Optimization of Monocrystalline $Mg_xCd_{1-x}Te/Mg_yCd_{1-y}Te$

Double-Heterostructure Solar Cells

by

Jacob J. Becker

A Dissertation Presented in Partial Fulfillment
of the Requirements for the Degree
Doctor of Philosophy

Approved April 2017 by the
Graduate Supervisory Committee:

Yong-Hang Zhang, Chair
Mariana Bertoni
Dragica Vasileska
Shane Johnson

ARIZONA STATE UNIVERSITY

May 2017

ABSTRACT

Polycrystalline CdS/CdTe solar cells continue to dominate the thin-film photovoltaics industry with an achieved record efficiency of over 22% demonstrated by First Solar, yet monocrystalline CdTe devices have received considerably less attention over the years. Monocrystalline CdTe double-heterostructure solar cells show great promise with respect to addressing the problem of low V_{oc} with the passing of the 1 V benchmark. Rapid progress has been made in driving the efficiency in these devices ever closer to the record presently held by polycrystalline thin-films. This achievement is primarily due to the utilization of a remote p-n heterojunction in which the heavily doped contact materials, which are so problematic in terms of increasing non-radiative recombination inside the absorber, are moved outside of the CdTe double heterostructure with two $Mg_yCd_{1-y}Te$ barrier layers to provide confinement and passivation at the CdTe surfaces. Using this design, the pursuit and demonstration of efficiencies beyond 20% in CdTe solar cells is reported through the study and optimization of the structure barriers, contacts layers, and optical design. Further development of a wider bandgap $Mg_xCd_{1-x}Te$ solar cell based on the same design is included with the intention of applying this knowledge to the development of a tandem solar cell constructed on a silicon subcell. The exploration of different hole-contact materials—ZnTe, CuZnS, and a-Si:H—and their optimization is presented throughout the work. Devices utilizing a-Si:H hole contacts exhibit open-circuit voltages of up to 1.11 V, a maximum total-area efficiency of 18.5% measured under AM1.5G, and an active-area efficiency of 20.3% for CdTe absorber based devices. The achievement of voltages beyond 1.1V while still maintaining relatively high fill factors with no rollover, either before or after open-circuit, is a promising indicator that this approach can result in devices

surpassing the 22% record set by polycrystalline designs. $Mg_xCd_{1-x}Te$ absorber based devices have been demonstrated with open-circuit voltages of up to 1.176 V and a maximum active-area efficiency of 11.2%. A discussion of the various loss mechanisms present within these devices, both optical and electrical, concludes with the presentation of a series of potential design changes meant to address these issues.

ACKNOWLEDGMENTS

TABLE OF CONTENTS

LIST OF TABLES

LIST OF FIGURES

x

CHAPTER 1

INTRODUCTION

The continued research and investment in solar technologies, most notably in photovoltaics, has resulted in remarkable improvements in their associated electricity costs—leading to an overall levelized cost of energy (LCOE) reduction of over 50% over the past 7 years [1]. As Silicon and GaAs solar cell efficiencies approach their respective detailed-balance limits [2], cadmium telluride (CdTe) based devices continue to languish well below the 32% limit [3], despite the fact that CdTe is an efficient photovoltaic material with a high absorption coefficient ($>15,000$ cm^{-1}) near the band-edge and a near-optimum bandgap with respect to the detailed balance efficiency for single-junction solar cells [4]. Indeed, the record Silicon and GaAs cells have monocrystalline absorbers while progress in the CdTe field continues to be driven by polycrystalline thin-films.

In fact, while polycrystalline CdS/CdTe solar cells have been utilized for photovoltaic applications with an achieved record efficiency of over 22%, as demonstrated by First Solar [3], monocrystalline CdTe devices have received considerably less attention. Prior to this thesis work, the record efficiency for a single-crystal CdTe absorber had stood for nearly 30 years at only 13.4% [5]. Our recent work together with others, have resulted in open-circuit voltages (V_{oc}) of over 1 V [6], [7]—a remarkable achievement considering the record thin-film V_{oc} is only 0.887 V [3], and the record efficiency single-crystal device demonstrated by Nakazama had a V_{oc} of only 0.892 V [5]. Yet in these designs, both poly- and monocrystalline, two issues play a major role in limiting the V_{oc}; i) low p-type doping concentration and ii) bulk non-radiative recombination at either the interfaces or in the bulk. With these two effects dominating, they limit the exploration of other factors and

their potential impact on V_{oc} (such as the contact layer). The record short-circuit current density (J_{sc}) and thus efficiency (η) of poly-crystalline CdTe devices have progressed considerably over the past several decades (a relative change of approximately 26% and 40%, respectively), while the V_{oc} has remained largely unimproved and has no contributed greatly to the dramatic progress in efficiency [3], [8]. The considerable bandgap-voltage offset ($W_{oc}=E_g/q-V_{oc}$) of approximately 0.52 V exhibited in the thin-film-market dominating CdTe devices is largely due to the three challenges that plague most CdTe thin-films: short bulk carrier lifetimes, high interface recombination velocities (IRV), and the inability to form a heavily doped p-type contact [6]. The high rates of non-radiative recombination found within the absorber layer that lead to the poor bulk carrier lifetime can largely be attributed to the recombination at the grain boundaries and absorber interfaces (CdS and ZnTe), as well as to the extremely low activation rate of the p-type dopant. Recent work with monocrystalline absorbers has attempted to explore these issues resulting in considerably higher activation rates for the p-type dopant and more abrupt interfaces [7]. It is for this very reason that the pursuit of double-heterostructure solar cell designs offers such a beneficial approach considering the deficiencies in II-VI based solar cells have historically been driven by this low V_{oc}.

Avoiding these limiting mechanisms is best achieved through the separation of the lightly doped absorber region from the highly-doped contact layer using a double heterostructure. Although several potential solutions exist, the CdTe/MgCdTe interface possesses extremely low interface recombination velocities due to the small lattice mismatch, making MgCdTe an ideal barrier material for minority carrier confinement and interface passivation, while also ensuring high-quality CdTe absorber growth above this

layer [9]. Effective minority carrier lifetimes of 3.6 μs are thus readily achieved in undoped CdTe double heterostructures while doped absorbers exhibit lifetimes on the order of hundreds of nanoseconds [6], [9], [10]. Absorber material quality and interface recombination are thus no longer the limiting factors in achieving high V_{oc}. The present challenge lies rather in providing adequate contacts to extract the large implied voltage at the maximum power point as an (equally) large external voltage. In particular, due to difficulties in doping p-type and high surface recombination in CdTe material, high-efficiency CdTe homojunctions are not currently a viable option and heterojunctions are employed in all of the record holding devices regardless of the layer structure; p-type absorber or n-type absorber.

This design technique is utilized in demonstrating a monocrystalline CdTe solar cell featuring a p-type a-Si:H hole contact layer with a record efficiency of 20.3% [11]. While allowing remarkable efficiency, the doped a-Si:H layer shows physical limitations, such as its moderate bandgap (~1.8 eV) which leads to considerable parasitic light absorption. A number of different material systems can be utilized in a similar manner, as is accomplished with p-type ZnTe:(As or Cu) [12]. The exploration of these different contact layer materials and their optimization as a hole contact in a double-heterostructure CdTe solar cell is presented throughout the following chapters. Materials include the aforementioned a-Si:H and p-ZnTe systems along with the previously unexplored option of CuZnS. The tradeoff that exists between providing an adequate built-in voltage (V_{bi}) and limiting parasitic absorption by maximizing transmission is a difficult optimization process that greatly differs amongst the contact materials studied here. A comparison on these grounds,

determining the most appropriate contact material for use with n-CdTe double-heterostructure solar cells is presented.

Despite these considerable improvements in the field of thin film solar cells, crystalline silicon cells continues to dominate the PV market with over 90% of the market share [13]. And yet, pushing the record efficiency of single-junction crystalline silicon cells (mono- or poly-) even further towards the practical limit is beginning to exhibit signs of diminishing returns, in terms of cost. In fact, to reach the aggressive LCOE goals set forth by the Department of Energy, it is alleged that improvements in current module efficiency alone will not be sufficient—reductions in BOS costs are believed to be even more important in achieving these goals [1]. Utilizing these well-established material systems as the foundation for the development of dual-junction devices though, may prove to be a lower-cost solution with the benefit of economy of scale. Assuming silicon, with a bandgap of 1.1 eV, is to be used as the lower bandgap subcell due to its well-established track-record in the PV market, the optimum bandgap for the upper cell is 1.7 eV with the potential to reach nearly 40% efficiency under one-sun [14]. As thin-film poly-CdTe is a proven low-cost and reliable PV technology with a bandgap closer to the ideal of 1.7 eV, this material system makes for an excellent choice as the starting point for the upper cell. Current state-of-the-art CdTe devices already incorporate additional elements, namely selenium, within the absorber to narrow the bandgap for the purposes of increasing current generation; because of the large bowing parameter for the ternary Cd(Se)Te, the bandgap drops down below 1.51 eV. The introduction of a number of other elements in place of selenium will have the opposite effect, making the achievement of a 1.7 eV absorber possible—these include but are not limited to: zinc, manganese, or magnesium.

Throughout this dissertation, both the 1.5 eV and 1.7 eV absorbers are explored simultaneously, discussing the path taken to achieve record efficiency values for their respective solar cell classes. The discussion begins with an overview of the double heterostructure design and its application to the II-VI material system. With the lattice constant of CdTe on the fringes of the commonly utilized grouping of semiconductors, finding both a suitable substrate and passivation material provides its own set of challenges. Next, this thesis aims to address the difficulties found in doping II-VI materials and develops an alternative solution in which an n-type absorber is used in conjunction with a remote p-n heterojunction. Device demonstration and optimization follow before ultimately concluding with an overview of potential design changes that could push this solar cell design beyond just record performance among its monocrystalline counterparts, but beyond the entire CdTe field as well.

CHAPTER 2

DESIGN OF $MG_XCD_{1-X}TE/MG_YCD_{1-Y}TE$ DOUBLE-HETEROSTRUCTURE ABSORBERS

This chapter will consider the methods in which high-quality CdTe epi-layer growth can be achieved, and the design of a double heterostructure built around this absorber. A discussion on the various material systems that can be used to passivate the interfaces and confine carriers within the absorber follows. The benefits and disadvantages of each system is compared with respect to their ability to confine carriers, resist atmospheric conditions, and passivate the absorber interface. The incorporation of magnesium within the absorber is explored in pursuit of a wide bandgap material to be used as the upper cell within a silicon-based tandem solar cell. The thickness of each respective absorber necessary to achieve near complete absorption of the solar spectrum is calculated using ellipsometry data for each material system.

2.1   Achieving high-quality epi-layer growth

The II-VI semiconductor lineup provides for a very wide range of available bandgap energies (particularly tellurium based compounds) and simultaneously provides material systems that range over a wide range of lattice constants. However, CdTe lies at the fringes of the more popular material systems with respect to the lattice constant, limiting the number of available substrates for high quality growth as shown in Fig. 1. Indeed, of the most commonly available substrates in Fig. 1, all are either group IV or III-V. And yet CdTe substrates themselves do exist and even though this would entail a homo-epitaxial growth, this is not actually the best option due to poor substrate quality and challenges associated with the removal of the surface oxide prior to MBE growth. II-VI material grown on InSb substrates has been demonstrated with a greatly reduced defect density—a

reduction of over two orders of magnitude under the right growth conditions—when compared with similar structures grown directly on CdTe substrates [15]. In addition, the combination of the small bandgap (0.17 eV) and high doping densities within the commercially available substrates leads to an extremely low resistivity which is beneficial for substrate based devices.
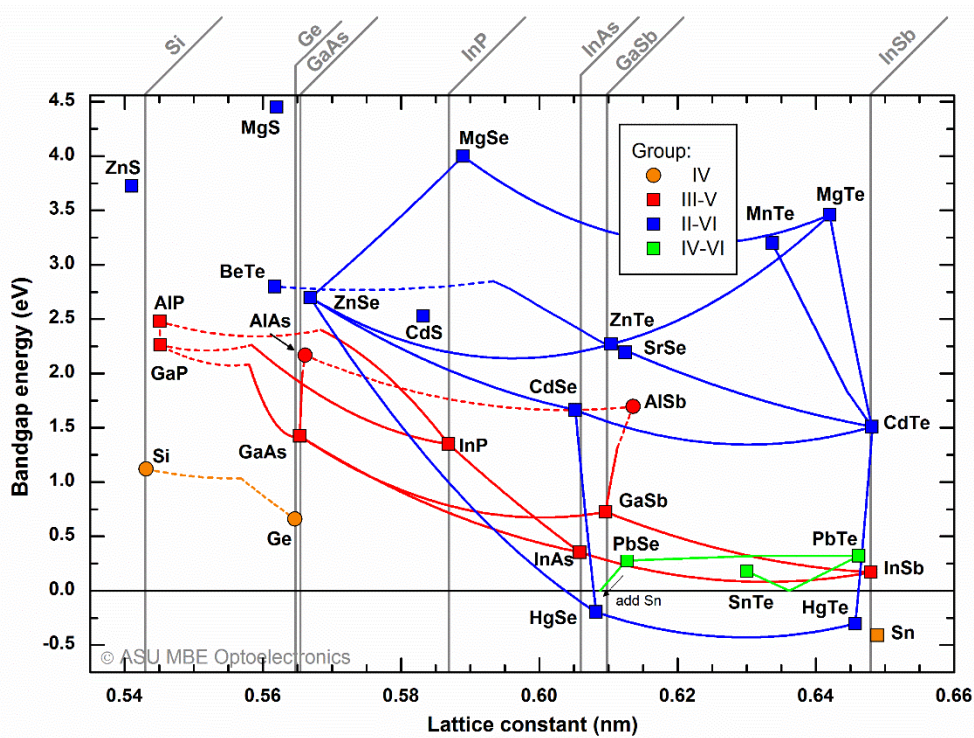
Fig. 1 Bandgap energy versus lattice constant for select Group IV, III-V, II-VI, and IV-VI compound semiconductors. Various popular substrates have been marked to indicate which other semiconductors materials are lattice matched.

The CdTe/InSb interface is one that has already seen considerable use in device applications ranging from wafer based solar cells to multi-color photodetectors [6], [16]. The small lattice mismatch between InSb and both CdTe (0.03%) and MgTe (0.9%) allows for extremely high quality double-heterostructure growths. The chemical and electronic structure of this interface has been broken down in the past with K. Mackey, et al. providing

7

an insight into the valence band offset of the system and the formation of intermediate InTe layers at the interface [17]. Further experimental probing into the quality of this interface is presented in Chapter 5.

2.2   Double-heterostructure design

Leveraging the high-quality CdTe epitaxially grown on InSb (100), a material of extremely high quality with a minimal dislocation density. However, this is only half the battle in achieving a reliable absorber with a high collection efficiency. Non-radiative recombination at the edges of the absorber are still a considerable concern and can drastically reduce the performance of a device as is the case with polycrystalline devices at the CdS and ZnTe heterointerfaces [7].

There are three well known II-VI binaries visible in Fig. 1 with bandgaps larger than that of CdTe that provide potential alloys for interface passivation and carrier confinement. MgCdTe, ZnCdTe and MnCdTe have all been well studied to varying extents and each provides different benefits as both barrier layers for a CdTe absorber or as a wide bandgap absorber itself. Because of the small lattice mismatch between MgTe and CdTe, relatively large amounts of magnesium can be added without dramatically effecting the quality of the interface of the CdTe/MgCdTe double heterostructure. However, the increasing bandgap leads to an increase in both the conduction band and valence band offsets; while beneficial for optical studies, which demonstrate the high lifetimes achieved using this material system, when utilized as a carrier selective contact, this becomes an issue. The conduction band offset (Q_C) and valance band offset (Q_V) ratio between CdTe and MgTe has been measured to be 70:30 and thus barriers exist for both electrons and holes [18]. Double heterostructures developed using III-V materials have been able to utilize materials with

similar offsets by controlling the barrier heights through proper doping control [19], [20]. For the CdTe system, this same methodology can be applied to the electron selective contact as the material system can be doped heavily n-type making it an acceptable back-side contact in an eventual double-heterostructure solar cell device. The high level of doping places the Fermi level very close to the conduction band which, at equilibrium, results in the formation of two narrow triangular barriers at the heterointerfaces through which electrons can tunnel (this can be visualized in Fig. 31 in later chapters discussing doped devices or in Appendix B). This same approach however is not feasible for use as a hole selective contact with this material system. CdTe and MgCdTe alike are difficult to dope p-type and achieving high carrier concentrations is nearly impossible without introducing a significant number of defects associated with the poor incorporation of p-type dopants; this topic will be addressed in more detail in later chapters. [21] Without the ability to reduce the barrier in the valence band, extraction of carriers at the hole contact can be difficult and the fill factor (FF) in a complete solar cell device is expected to suffer.

The ZnTe binary on the other hand is a wide bandgap material with the entirety of the band offset with CdTe contained within the conduction band [22], [23]. Thus, barriers can be constructed exclusively within the conduction band—a major benefit when developing a barrier layer for use between the absorber and hole contact. In this configuration, hole transport is not hindered at flat band regardless of the level of zinc incorporation. This material has been utilized quite successfully within current state-of-the-art polycrystalline devices where a copper-doped p-type ZnTe layer is used as the hole contact at the backside of the device. A combination of SIMS measurements and TEM images on such devices

show a considerable amount of zinc-cadmium interdiffusion creating a graded interface that may provide further passivation within these structures [23].

The wide bandgap MnTe binary is the next nearest neighbor to CdTe in terms of lattice constant outside of MgTe. In a similar manner to MgCdTe though, the MnCdTe valence and conduction band offsets is split with a ratio of 40:60 resulting in barriers for both electrons and holes as the manganese content increases [24]–[26]. MnCdTe however, may still prove beneficial as a replacement for MgCdTe as it is much more resilient to oxidation—providing for a much simpler process. Fig. 2 shows how the band edges of each respective ternary compares with that of CdTe as the incorporation of the additional element increases.
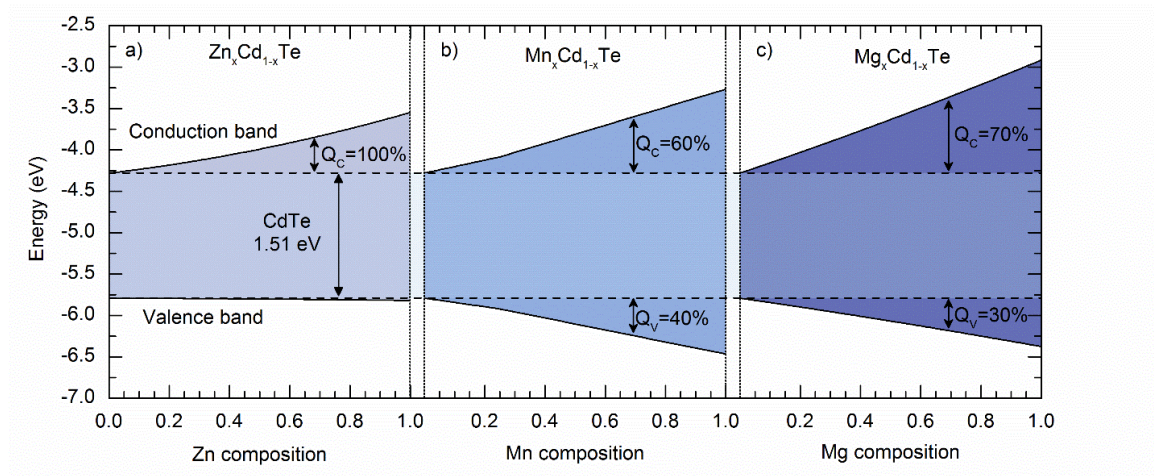
Fig. 2 Band edge minimum of each of the discussed ternary materials including a) ZnCdTe, b) MnCdTe, and c) MgCdTe. The CdTe energy levels are also included in dashed lines.

In the discussion of energy barriers to this point, the topic of lattice mismatch has been neglected. While ZnCdTe has been utilized successfully as a hole-contact material in polycrystalline devices and provides an ideal band alignment with CdTe for just that purpose, when utilized within a single-crystal environment, the large difference in lattice

constant results in relaxed layers that can no longer provide adequate passivation. The interface between CdTe and MnCdTe shares the same disadvantage to a lesser extent. To achieve the same conduction band offset with a $Zn_pCd_{1-p}Te$ barrier as is achieved with the optimum $Mg_{0.4}Cd_{0.6}Te$ layer (2.24 eV), a smaller bandgap of only 2.039 eV is required as there is no change in the valance band edge energy level. Yet, this change in bandgap necessitates approximately 77% zinc which shifts the relaxed lattice constant considerably, resulting in a mismatch of 4.46% with the underlying CdTe absorber. Conversely, because conduction band offset between CdTe and MnCdTe is *smaller* than that of MgCdTe and CdTe, it is necessary to utilize a barrier layer with an even larger bandgap to achieve the same barrier height for electrons. The bandgap versus lattice constant for each of these ternary systems is shown in Fig. 3 along with specific point at which each ternary achieves the same conduction band offset with CdTe—utilizing $Mg_yCd_{1-y}Te$ with $x=0.4$ as the standard. The specific material parameters associated with these points is included in TABLE 1 along with the lattice mismatch f_m.
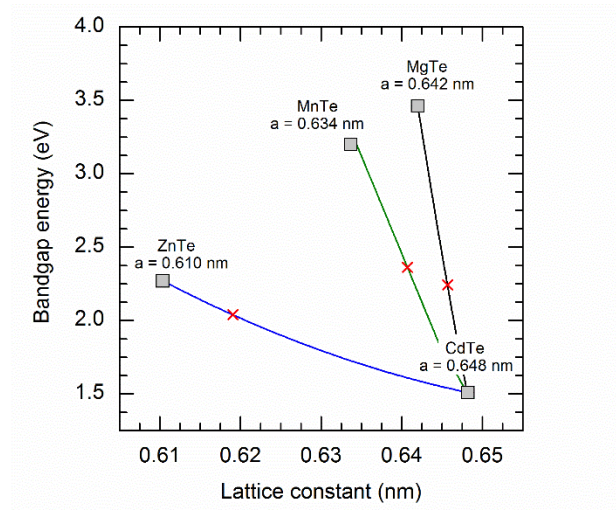
Fig. 3 $Zn_pCd_{1-p}Te$, $Mn_qCd_{1-q}Te$, and $Mg_yCd_{1-y}Te$ bandgap energy versus lattice constant along with the associated binaries: ZnTe, MgTe, and CdTe.

TABLE 1
TERNARY BARRIER PARAMETERS

	$Zn_pCd_{1-p}Te$	$Mn_qCd_{1-q}Te$	$My_yCd_{1-y}Te$
p,q,x	0.77	0.54	0.40
a (nm)	0.6191	0.6407	0.6457
E_g (eV)	2.039	2.36	2.242
ΔE_c (eV)	0.509	0.512	0.512
ΔE_v (eV)	0.020	0.338	0.220
f_m (%)	4.46	1.13	0.35

Maintaining coherently strained layers at these composition levels is very difficult to achieve without making the layers so thin that they can no longer provide adequate confinement; this is especially true for the hole-selective layer where it is likely to be capped with an amorphous contact. Fig. 4 shows the critical thickness of the three ternary materials discussed versus the anion composition. The MgCdTe material system is the only option that can seemingly achieve a high bandgap (magnesium composition) while simultaneously remaining coherently strained at thicknesses that provide clear confinement. The example composition levels discussed earlier have been marked on each curve in the figure while the inset table shows the critical thickness for that level. Equation (1) shows the Mathews and Blakeslee model that was used to calculate the curves in Fig. 4 with the material parameters needed for the calculations are given in TABLE 2 [27].
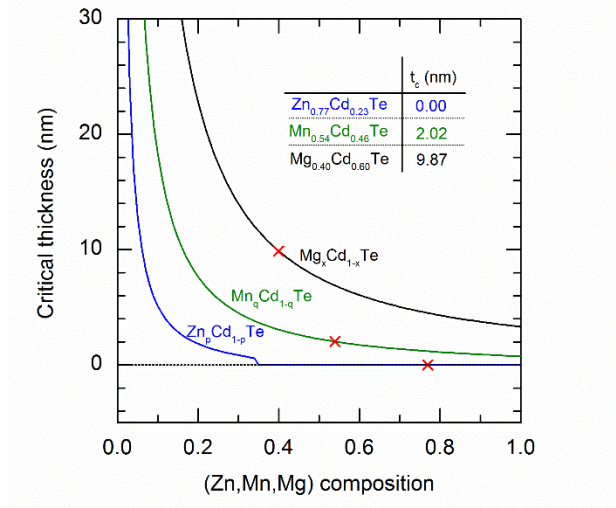
Fig. 4 Critical thickness versus group-II element composition for three potential ternary barrier layers: MgCdTe, MnCdTe, and ZnCdTe.

TABLE 2
MATERIAL ELASTIC PROPERTIES

	CdTe [28]	ZnTe [28]	MgTe [28]	MnTe
a (nm)	0.6481	0.6104	0.6420	0.6337 [29]
E_g (eV)	1.51	2.27	3.46	3.2 [30]
c_{11} (10^{11} dyn/cm^2)	5.35	7.15	5.28	5.86* [17,18]
c_{12} (10^{11} dyn/cm^2)	3.69	4.08	3.66	3.28 [31]
v	0.408	0.363	0.409	0.359 [17,18]

* The c_{11}/c_{12} ratio was measured in [30] while the value of c_{12} was extrapolated using data from [31]

$$h_c = \frac{a_{sub}}{K\sqrt{2}\pi f_m}\frac{\left(1 - {}^v/_{f_m}\right)}{(1+v)}\left(\ln\left({}^{\sqrt{2}h_c}/_{a_{sub}}\right) + 1\right) \qquad (1)$$

where a_{sub} is the lattice constant of the substrate or underlying material system (assumed to be CdTe for the purposes of this comparison), v is the Poisson's ratio as defined in TABLE 2, and f_m is the in-plane strain or lattice mismatch as defined in TABLE 1. The K parameter is a constant used to modify the solution depending on the structure, i.e. whether the layer has a cap. The critical thickness values reported here are not taken to be precise limits in real device applications but rather are utilized here to provide a helpful comparison between the material systems and highlight key disadvantages in choosing barriers.

13

With these limitations and the ideal band structure in mind, MgCdTe provides for the best immediate solution for passivation and confinement at both the electron- and hole-selective contacts. For the electron contact, both MgCdTe and MnCdTe provide comparative hole confinement when considering the valence band offset but MgCdTe will most likely provide for better passivation at the interface considering the better lattice match. In either case, there still exists a considerable barrier in the conduction band as well but as discussed earlier, n-type doping levels in these materials can be sufficient enough to pull down the bands in the center of the barrier. While ZnCdTe would be the perfect solution for the hole-contact material in terms of band offset, the strain is just too high to allow for proper interface passivation. Using MgCdTe in its place is thus necessary but not ideal, and results in a design that requires tradeoffs be made.

With MgCdTe the chosen material system for passivation and carrier confinement, the development of a 1.7 eV absorber is best accomplished using the same ternary system. The ideal tandem configuration may not utilize this particular bandgap for the upper cell when the bottom-cell bandgap is also a variable, yet with cost and stability major factors in deciding a suitable framework, choosing an existing technology to build off of is imperative. Using a 1.1 eV silicon cell as the foundation of a tandem design, provides a well-established technology on which an upper cell can be optically matched. Under these conditions, a bandgap of 1.7 eV provides for the best potential tandem efficiency under one-sun [14]. The 13% magnesium composition required to achieve this bandgap has been determined through a combination of PL and ellipsometry measurements to determine the bandgap, and XRD scans to verify the magnesium composition [32], [33].

From this data, the absorption coefficient can be used to determine the required absorber thickness to ensure near 100% absorptance of the solar spectrum above 1.7 eV. Absorptance is the ratio of the absorbed photon flux to the total incident solar photon flux at the surface of the absorbing material for energies above the bandgap. The following equation can be used to calculate the absorptance:

$$A_\alpha = \frac{\int_{E_g}^{\infty}\left[1 - e^{(-\alpha(E)\cdot t)}\right] \cdot \Phi(E)dE}{\int_{E_g}^{\infty} \Phi(E)dE} \tag{2}$$

where E is the photon energy, E_g is the bandgap of the absorber, t is the thickness of the layer, $\alpha(E)$ is the absorption coefficient as a function of photon energy, and $\Phi(E)$ is the solar photon flux (the AM1.5G spectrum is utilized here).

The absorptance in $Mg_{0.13}Cd_{0.87}Te$ versus thickness is shown in Fig. 5 compared with that of CdTe. For a CdTe absorber, 1000 nm can absorb 97.5% of all light above the CdTe bandgap. A similar thickness is required for a $Mg_{0.13}Cd_{0.87}Te$ absorber to absorb upwards of 95% of the spectrum above 1.7 eV. Unfortunately, because of the lattice mismatch between $Mg_{0.13}Cd_{0.87}Te$ and the underlying InSb, as the thickness of the absorber increases the layer will continue to relax. While this may not be detrimental in the long run, it was avoided for all devices discussed in this thesis. A thickness of 500 nm still allows for nearly 90% of the incoming light to be absorbed while maintaining a relatively high quality absorber; this 10% transmission loss will be visible in layer chapters as the quantum efficiency of the completed devices are explored.
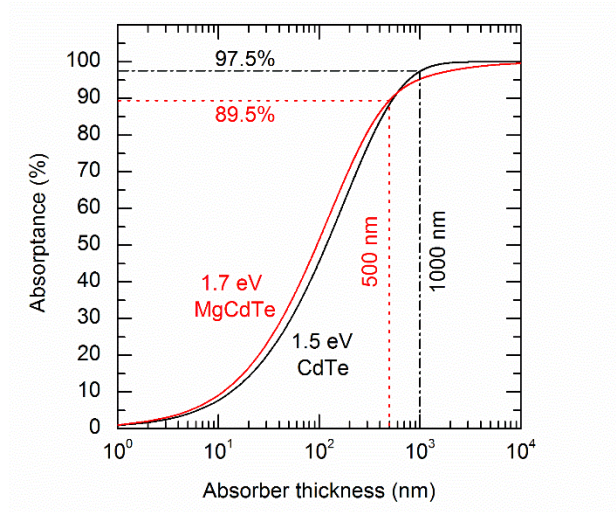
Fig. 5 Simulated absorptance as a function of CdTe (black) and MgCdTe (red) absorber thickness for the AM1.5G spectrum above each absorber's respective bandgap.

CHAPTER 3

DEMONSTRATION OF $Mg_xCd_{1-x}Te/Mg_yCd_{1-y}Te$ DOUBLE-HETEROSTRUCTURE SOLAR CELLS

There are a number of additional processes required in employing a double heterostructure within a completed solar cell device that will be discussed in the following chapter. Namely, charger separation and extraction are accomplished through the formation of a built-in electric field that is not accomplished within the confines of the discussed double heterostructures. The concept of a remote p-j junction is discussed prior to delving into the various material systems that can be used to generate a high V_{bi} within the double-heterostructure, while remaining outside of direct contact with the absorber. ZnTe, CuZnS, and a-Si:H are all considered as potential hole contact materials with wider bandgaps than the primary absorbing material but can still provide high hole concentrations.

3.1 Circumventing p-type doping in $Mg_xCd_{1-x}Te$ materials: the use of a remote junction

The issue of low V_{oc} in poly-CdTe devices can be attributed to a number of different mechanisms including recombination at the interfaces of the absorber, short carrier lifetimes within the absorber, and low p-type doping level. With n-CdS/p-CdTe processes dominating industrial output, most research work has followed suit and focused on understanding and improving the limitations associated with p-type CdTe and passivating the already established interfaces. Improving commercial technologies without dramatically affecting the process has been important in lowering cost. Simultaneously increasing the hole density within the absorber along with the material lifetime has been the goal of a number of studies that have resulted in the development of a few post-growth

processes to maximize these parameters. These include the development of $CdCl_2$ or $MgCl_2$ annealing processes to help interdiffuse the CdTe and CdS at the interface and passivate grain boundaries, and the addition of copper to the contact and absorber to improve both hole density and lifetime [34], [35]. Despite all of these post-growth optimization processes, the carrier lifetime in the absorber is still just several nanoseconds and carrier densities in the absorber rarely exceed 10^{15} cm^{-3} [7]. The interface between the absorber and the CdS electron contact and the ZnTe hole contact are both highly defective and exhibit very high recombination velocities [7].

Utilizing the double-heterostructure design but moving potentially defective contact layers outside of the absorber and the dedicated $Mg_yCd_{1-y}Te$ barrier/passivation layers—as is shown in Fig. 6—allows for the generation of a built-in voltage as is necessary for charge separation without sacrificing the quality of the absorber interfaces. This structure prevents the contact layers from compromising the quality of the absorber, whether it be through dopant induced recombination centers or broken bonds associated with non-crystalline materials, by confining minority carriers to the absorber. This is a widely used approach in compound semiconductor devices ranging all kinds of optoelectronic applications [19], [20], as well as used in silicon heterojunction with intrinsic thin layer (HIT) solar cells [36]. Where these designs differ though, is that while a HIT cell consists of a set of only two material systems where the passivation layer and heavily doped contact are both a-Si:H, the $Mg_xCd_{1-x}Te/Mg_yCd_{1-y}Te$ double heterostructure can accommodate any number of other material systems as a contact material. This is not merely a possibility, but a necessity because the p-type doping capabilities in CdTe are so limited. While many of the laser, LED, or solar cell devices constructed using other compound semiconductors can dope the

18

opposing barrier layers heavily p- and n-type, the solar cell devices discussed in this thesis work utilize an intrinsic $Mg_yCd_{1-y}Te$ barrier layer at the hole contact to maintain the passivated interface with the absorber.
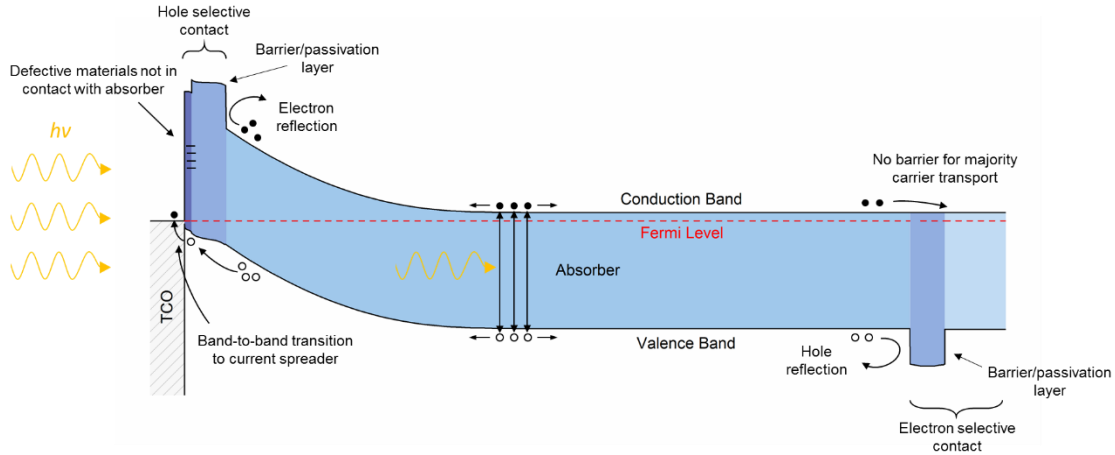
Fig. 6   Schematic band edge diagram for the ideal II-VI double-heterostructure design.

A great deal of the issues associated with p-type doping in the CdTe absorber—including compensation and the dramatic reduction in material quality at even low p-type doping levels—can be resolved by merely adopting a different architecture that relies on an n-type CdTe absorber. In this manner, the dilemma of achieving the doping levels in CdTe necessary for a high V_{bi} can be circumvented. Together, these two differences in design—utilizing n-type doping instead of p-type doping in the CdTe, and placing the heavily doped contact layers outside of the double heterostructure—result in a "remote junction" design that eliminates most of the non-radiative recombination concerns associated with the standard poly-CdTe thin-film process.

Utilizing a high-quality monocrystalline n-type absorber addresses two of the issues discussed above in that moving away from p-type doping enables longer minority carrier lifetimes and allows for higher carrier concentrations, and thus V_{oc}, to be reached in solar cell devices. As demonstrated in previous work with this material system, both undoped

19

and n-CdTe double heterostructures demonstrate exceptional material quality, not just because the material system is monocrystalline but because the indium dopant used has a close to 100% activation rate up to the low 10^{17} range but begins to reduce beyond that point [10]. In these double-heterostructures, bulk minority carrier lifetimes in undoped absorbers are as long as several microseconds while n-type doping with indium will reduce the lifetime to hundreds of nanoseconds at doping levels of 10^{16} to 10^{17} cm^{-3} [10] due to an enhanced radiative recombination rate. Lifetimes at these levels are more than sufficient to give diffusion lengths longer than the micron thick absorbers needed for full absorption of the solar spectrum.

But effective minority carrier lifetime in an undoped absorber is not necessarily the only figure of merit when attempting to maximize the V_{oc} of the device. The total minority carrier lifetime reported is determined by contributions from multiple recombination mechanisms—non-radiative recombination including SRH, Auger, or interface recombination, as well as radiative recombination. While both non-radiative and radiative carrier lifetimes can decrease with doping, it is important to understand the ratio of these two mechanisms and the importance of a system dominated by radiative recombination over non-radiative recombination.

Under constant excitation, the PL intensity of a material is proportional to the internal luminescent quantum efficiency (η_{int}) which is defined as the ratio of the radiative recombination rate to the total recombination rate including both radiative and non-radiative recombination shown in equation (3). The external luminescence quantum efficiency (η_{ext}), which quantifies the fraction of internally emitted photons that are *able to*

escape the front surface of the structure and can therefore be directly measured, is related to η_{int} as shown in equation (4).

$$\eta_{int} = \frac{R_{rad}}{R_{rad} + R_{nr}} \tag{3}$$

$$\eta_{ext} = \frac{\gamma_e \eta_{int}}{1 - \gamma_r \eta_{int}} \tag{4}$$

where γ_e is the photon extraction factor from the surface describing the probability that a radiatively emitted photon will escape the front surface, and γ_r is the photon recycling factor describing the probability that a photon will be reabsorbed within the material. With this relationship, it can be seen that even if the total recombination rate increases, if the radiative recombination rate increases at a greater pace than the non-radiative recombination rate, η_{int} (and thus η_{ext}) will still increase. Maximizing this ratio and the η_{ext} is thus a better metric when attempting to maximize the potential quasi-Fermi level separation in a device. Understanding why this is beneficial for a solar cell device may seem counterintuitive but can be explained qualitatively. Under ideal open-circuit conditions, in which there is no non-radiative recombination and none of the photo-generated carriers will be collected as current, the same number of photons that are absorbed must therefore be emitted radiatively near the band edge with the energy difference accounted for through heat. This principle is paramount in determining the limiting efficiency of a solar cell in the detailed balance model for p-n junction solar cells [2]. This phenomenon has led to the coining of the phrase, a good solar cell makes a good LED [37]. Therefore, any reduction in the measured emission implies photons were lost to non-radiative recombination or parasitic absorption. With this reasoning, η_{ext} can be used

to estimate how far the device's V_{oc} will depart from the ideal V_{oc} of a solar cell (known as implied-V_{oc}), as shown in equation (5) [37]–[39]:

$$iV_{oc} = V_{db} - \frac{kT}{q}|\ln(\eta_{ext})| \tag{5}$$

where V_{db} is the ideal V_{oc} as determined by the detailed balance limit. Fig. 7 shows that even as the total measured effective lifetime within the CdTe/Mg$_{0.46}$Cd$_{0.54}$Te double heterostructure drops with an increase in doping, the PL intensity, and thus, the η_{ext} continues to rise [10]. However, as the indium activation rate within the absorber begins to reduce beyond indium concentrations of 1×10^{17} cm^{-3}, these indium atoms act as recombination centers and the non-radiative recombination begins to dominate.

Another way to view this is because the V_{oc} is proportional to the log of the np product as shown in equation (6), an increase in the doping N_D can lead to an improvement in V_{oc} so long as the accompanying reduction in the excess carrier concentration Δp is smaller.

$$V_{oc} = \frac{kT}{q}\ln\left[\frac{(N_D + \Delta p)\Delta p}{n_i^2}\right] \tag{6}$$

A doping of over 1×10^{16} cm^{-3} was chosen for the devices to ensure consistent proximity to the peak seen in Fig. 7 without the possibility of inadvertently doping the structure to high.
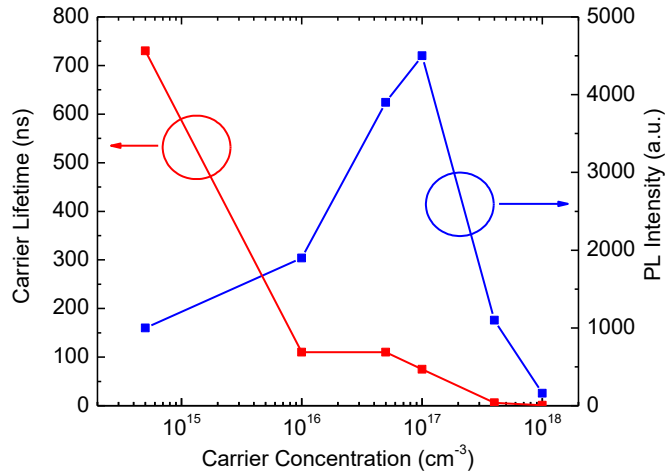
Fig. 7 Carrier lifetime and photoluminescence peak intensity of CdTe/Mg$_{0.46}$Cd$_{0.54}$Te double heterostructures with different carrier concentrations [10].

Compared with CdTe however, the PL intensity for Mg$_x$Cd$_{1-x}$Te alloys decreases with the addition of any indium as shown in Fig. 8. In part because incorporation and activation of indium in MgCdTe is so low, large quantities of indium are necessary to achieve even relatively small electron concentrations. Correlating dopant densities determined from SIMS results with carrier concentrations as determined by CV measurements, indium has an activation rate of only 10% in the Mg$_{0.13}$Cd$_{0.87}$Te layers studied with a maximum achieved carrier concentration of only 3×10^{15} cm^{-3}. It is reasonable to expect that a large number of dopants create deep levels and become recombination centers, thereby dramatically increasing the non-radiative recombination rate.
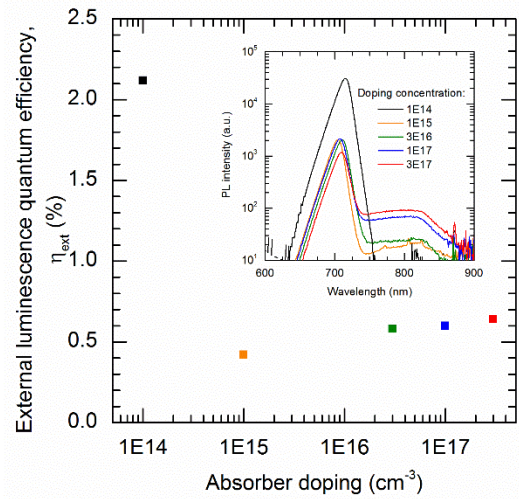
Fig. 8 External luminescence quantum efficiency (η_{ext}) as a function of $Mg_xCd_{1-x}Te$ absorber doping. The inset in the left figure shows the spectral PL intensity for the same samples. The absorber doping levels listed (1×10^{15}, 3×10^{16}, 1×10^{17}, and 3×10^{17}) are designed levels and do not necessarily reflect activated donor sites, while the nominally intrinsic sample is listed under the measured carrier concentration of 1×10^{14} cm^{-3}. Unpublished measurements taken by Dr. Xin-hao Zhao and Dr. Yuan Zhao.

Indium can be fairly mobile, and large quantities of indium will often out-diffuse from the InSb substrate and buffer layer into subsequent epi-layers; later chapters show this phenomenon through SIMS profiles of the CdTe/InSb interface as well as in completed solar cell devices (Fig. 14 and Fig. 43). For these reasons, it is believed that the presence of doping N_D will have an outsized detriment on the non-radiative minority carrier lifetime and the excess carrier concentration. Fortunately, the lifetime of 560 ns measured for undoped absorbers is still sufficiently long for the relatively thin MgCdTe absorbers and the iV$_{oc}$ is still relatively high at 1.29 V for a 1.2% η_{ext} under one-sun conditions; this is assuming a calculated V$_{db}$ of 1.4 V. However, this still leads to issues when attempting to provide electron selective contacts which require high levels of doping in the barrier layer. Furthermore, indium has been found to move quite readily from even doped barrier layers

24

into undoped absorbers, thereby reducing the PL of the entire structure. For this reason, both barrier layers cladding the wider bandgap MgCdTe absorber must be left undoped to maintain the high level of quasi-Fermi level separation within the structure. Yet this may not be the case for all potential MgCdTe dopants. Indium seems to be the n-type dopant with the lowest activation rate once magnesium is added with halogens such as bromine, chlorine, or iodine providing potential alternatives [40].

3.2   Choice of hole contact and device demonstration

Fig. 9 shows the general structure of solar cells fabricated using this architecture for both 1.5 eV and 1.7 eV absorbers. Interface passivation and carrier confinement is provided using $Mg_yCd_{1-y}Te$ barrier layers on either end of the n-CdTe or i-$Mg_xCd_{1-x}Te$ absorber. All double heterostructures discussed were grown at Arizona State University on a 2" n-type InSb substrate in a VG V80H dual chamber MBE system. The InSb buffer layer was grown in a dedicated III-V chamber after thermal desorption of the substrate's oxide at a substrate temperature of 390 °C and a Sb/In flux ratio of 1.5. After transferring the wafer while under ultra-high vacuum to a dedicated II-VI growth chamber, all subsequent CdTe material growth is carried out at a substrate temperature of 265 °C and a Cd/Te flux ratio of 1.5. Unfortunately, the inability to effectively dope CdTe p-type prevents this same material from being employed as the hole contact or an emitter layer in a standard homojunction. Each material employed in its place is explored in detail in the following sections. Upon deposition of the hole-contact layer, the final devices can be processed. Indium tin oxide (ITO) patches were deposited via sputtering on the surface of the hole contact to act as the electrode responsible for lateral current flow. While ITO is used for all devices discussed, it's entirely possible to use any number of transparent conducting oxides (TCO) depending

25

on the underlying contact decided upon. Silver contact pads are then deposited on the edges of the ITO mesas to provide stable, long term contact for electrical probing. This entire substrate based device is mounted onto a gold-coated silicon wafer using silver conducting paste to provide both stability and allow for probing of the back contact.
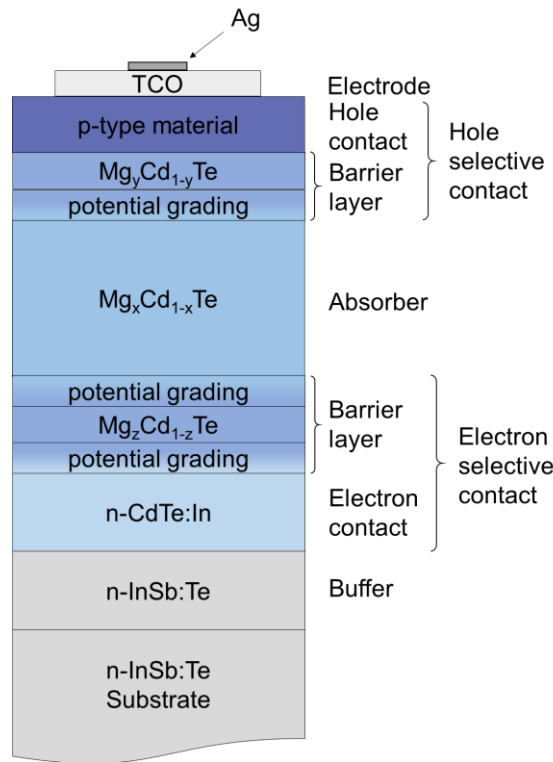
Fig. 9 General layer structure of the $Mg_xCd_{1-x}Te/Mg_yCd_{1-y}Te$ double-heterostructure solar cell utilizing an isolated hole contact.

Device mesa design has gone through several iterations from the outset of the project. ITO patches define the approximate mesa area in all situations as the top electrode. Fig. 10 shows the evolution of the mesa design along with the size and shape of the aperture used for Light IV measurements. Probing the patch directly is possible and was the method originally used, however, silver makes a great contact to ITO and prevents probe damage. In order to prevent shading during the measurement, the silver contact pad must be placed

at the edge of the mesa as seen in Fig. 10 b), yet as the device area increases, resistive losses due to lateral current transport increase. While the ITO is farily conductive with a sheet resitance of less than 100 Ω sq^{-1}, at a thickness of only 50 nm, silver fingers are necessary to minimize loss due to latteral current flow.
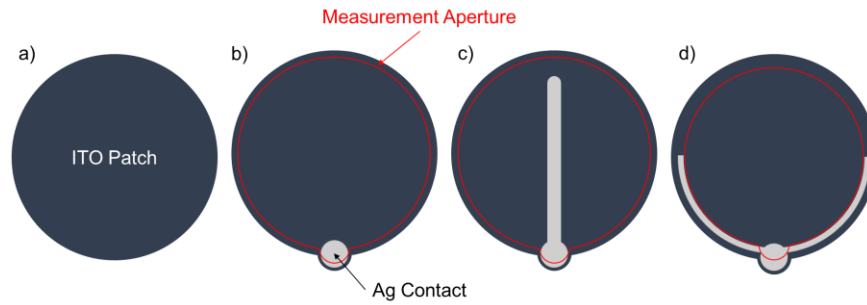
Fig. 10 Solar cell device mesa design history detailing silver contact design and coverage of the measurement aperture.

Indeed, devices of different mesa areas are processed on each sample and Fig. 11 compares the average IV characteristics for different mesa areas on one such wafer utilizing mesas of design b. For devices of this design, as the area increases, current must flow laterally for longer disstances through the ITO. This change is typified in the FF loss seen in Fig. 11 c) between devices of 2 mm versus devices of 3 mm diameters. In addition, a difference in J_{sc} is also seen with a change in mesa diameter. This difference is largely explained by the increase in relative contact shading as the metal coverage moves from only 1% to 2.6% for 3 mm diameter devices and 2 mm diameter devices, respectively. To counter this reduction in FF, metal fingers are necessary to carry current to the probe pad.
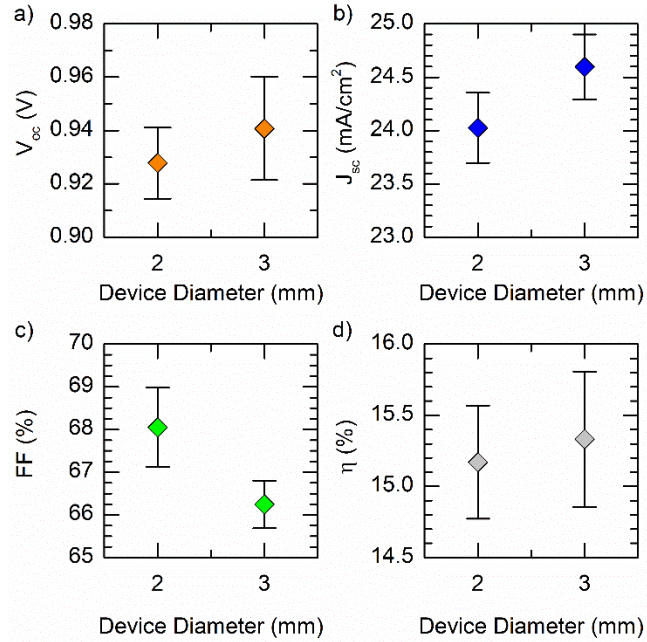
Fig. 11 Average V_{oc}, J_{sc}, FF, and η for samples with device diameters of 2- and 3-mm of design b shown in Fig. 10; error bars indicate the standard error of the mean for devices on the same wafer.

The addition of the silver finger in Fig. 10 c) eliminates this concern but of course results in considerable metal coverage. A potential solution is presented in Fig. 10 d) where the silver fingers are wrapped around the edges of ITO mesa. The measurement aperture can then be made slightly smaller than the inner diameter of the contact while still maintaining low metal coverage under aperture at 1.1% and 1.6% for 3 mm diameter devices and 2 mm diameter devices, respectively. Photos of the most recent iterations of finger deisng are shown in Fig. 12. This design only limits resistance losses so long as the total device area remains relatively small—lateral current flow limited to < 1.25 mm. The bottom contact is much simpler in design and fabrication. Because of the low bandgap and high conductivity of the InSb substrates, little effort is required in producing an ohmic contact on the backside of the device. Conducting silver paste is used to mount each device

28

onto a silicon carrier wafer coated with gold which provides for low resistance lateral current flow to the eventual probe tips. The silicon carrier wafers are coated with a thin 50 nm layer of titanium followed by a 250 nm layer of gold; the titanium layer is primarily used for adhesion purposes.
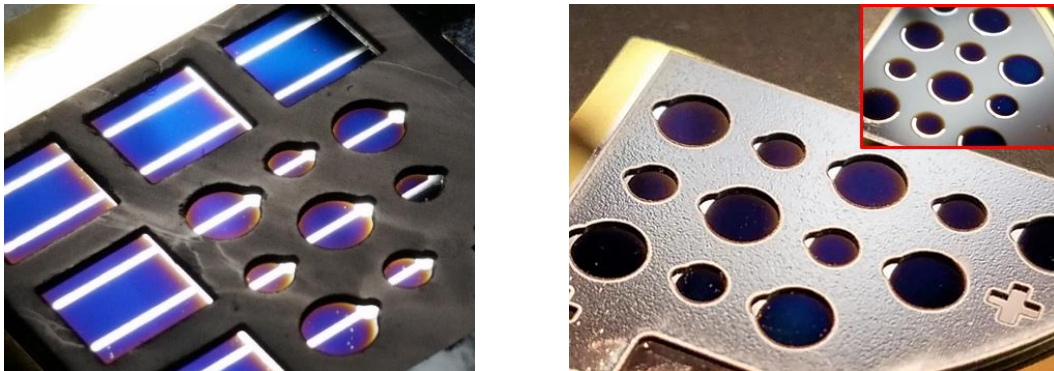
Fig. 12 Photos of completed solar cell devices under aperture. Photo a) depicts a single finger design with considerable metal coverage while photo b) depicts the crescent finger design with the inset showing the metal finger layout under the aperture.

3.2.1 Devices using zinc telluride

ZnTe is a wide bandgap material of 2.25 eV [28] that can be heavily doped p-type. ZnTe has been used as a hole contact in polycrystalline devices to great benefit, although in those circumstances it is used in conjunction with a p-type CdTe absorber as is standard with polycrystalline designs [23]. The material has even been integrated into commercial modules [41]. What remains to be seen is whether this material can be utilized as the primary hole contact for the monocrystalline devices discussed here in which an n-type absorber is used. With polycrystalline devices, CdS is the primary generator of the built-in potential that is eventually extracted as voltage, and not the ZnTe hole contact.

Two different approaches were taken to produce a highly conductive ZnTe hole contact on a CdTe absorber based device to test the viability of the contact material. While the

overall design of the underlying absorber will remain the same in both cases, the deposition method and doping species for the contact layer differs. The ZnTe hole contact was doped with arsenic in one case and coper in another. In the case of arsenic doping, the p-ZnTe layer was grown in a custom MOCVD system at Rensselaer Polytechnic Institute (RPI) at 300 °C after the completion of the MBE grown absorber and cladding barrier layers. Further processing and characterization though were carried out entirely at ASU. The growth conditions have been shown, through Hall measurements carried out at RPI, to produce p-type ZnTe films with concentrations of 2×10^{18} cm^{-3} [42].

In the case of copper doping, the cell can be fully grown by MBE at Arizona State University. This copper doping process differs from the arsenic doped case in that the latter utilizes an in-situ doping process, while the former is accomplished via post growth diffusion. A thin layer of copper is sputtered on the surface of the now-intrinsic ZnTe contact where it can then be driven in through diffusion. The amount of copper necessary to achieve high carrier concentrations within a 10 nm contact layer is very small and only very short copper depositions are required. Hall measurements on ZnTe films doped with only 1 nm of copper on the surface indicate an average concentration of 4×10^{18} cm^{-3}, while CV measurements on the same samples indicated an average concentration of 6×10^{18} cm^{-3}. In both of these cases, no additional drive-in anneal process was used outside of the elevated temperatures achieved during processing. Bcause these copper layers are so thin, removal of the seed layer is not entirely necessary as they are still highly transparet. Small levels of absorption occur within the metal layer though and can contribute to a reduction in potential device current as is seen in Fig. 13. The reflectance of these ZnTe surfaces will also change slightly with the addition of copper but this change is less relevant once we

transition to completed devices in which the surfaces will be coated with additional anti-reflection coating layers.
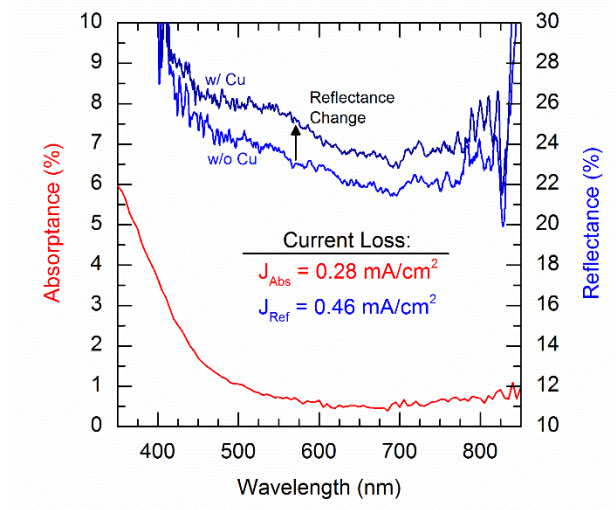
Fig. 13 Spectral absorptance and reflectance of 1 nm thin copper film. The absorptance was measured for a thin film of copper deposited on a glass slide while the reflectance comparison was made between the surface of ZnTe with and without the copper seed layer. The inset table shows the potential current loss for a CdTe device due to these two changes.

In addition, the copper can migrate into the CdTe absorber, and while it is employed as a p-type dopant in typical polycrystalline processes, it is a deep-level acceptor with extremely poor incorporation [34], [35]. With an n-type absorber, incorporated or not, the presence of copper will lead to a reduction in performance either through dopant compensation or an addition of recombination centers. Lifetime and overall PL intensity has been shown to be dramatically reduced with an excess of copper [35]. Preventing this migration is essential to maintain the high quality and long carrier lifetime in the absorber. And yet, the SIMS profile shown in Fig. 14 shows just such an undesirable occurance. Copper has migrated, from the surface, several hundred nanometers into the CdTe absorber. It is worth noting that significant indium diffusion from the substrate and

subsequent buffer layer is present at the back side of the device and can be seen to increase

the doping in the bottom 250 nm of the absorber.
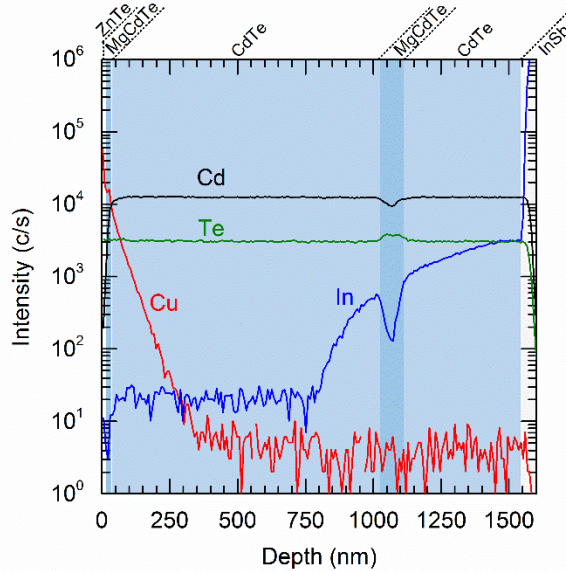
Fig. 14 SIMS profile of a solar cell with a copper-doped ZnTe hole contact. The profile was measured with a primary current of 100 nA with a raster of 250 µm and a field aperture in place, thereby limiting the sampling area to a 60 µm square in the center. SIMS measurements were carried out at the NanoSIMS facility at ASU.

While annealing after copper deposition is not necessary to achieve copper activation in the ZnTe, additional processing steps as well as operating conditions can expose the cell to temperatures that may effect the migration of the copper. The SIMS profile was taken on a solar cell without any annealing and already shows copper within the absorber; as the copper seed layer isnt removed during processing, annealing can only increase the density and depth of the copper in the absorber. Using the PL quantum efficiency as an indicator of the iV_{oc} [43], significant degradation is seen as annealing moves additional copper into the absorber. Annealing was carried out in atmosphere for a period of 30 seconds at each temperature. As can be seen in Fig. 15, even before annealing, 1 nm of copper leads to a

reduction in PL. As the annealing temperature nears 150 °C, the PL begins to crater with a complete loss of performance and zero PL intensity at only 200 °C, while the control sample takes longer to decay. Reducing the thickness of the copper material at the surface protects, to some extent, the integrity of the absorber with little to no annealing, but is still detrimental when exposed to temperatures beyond 100 °C.
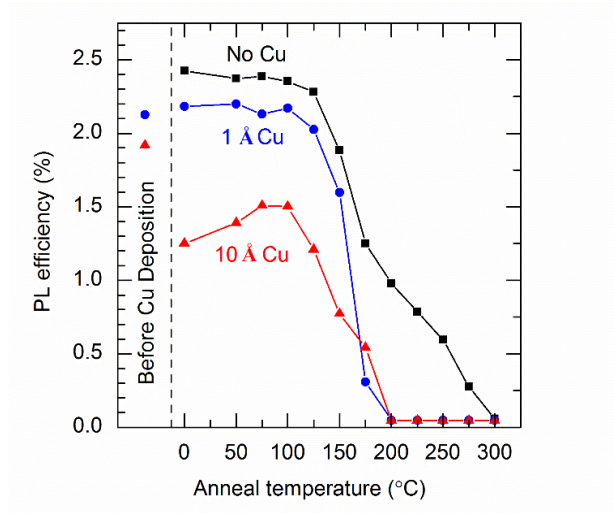
Fig. 15 PL quantum efficiency vs. anneal temperature for samples with 0.1 nm of copper and 1 nm of copper on the surface of the ZnTe contact layer compared with a control sample with no copper deposition.

Fig. 16 shows the structure of the fabricated solar cells using this architecture with p-ZnTe as the hole contact layer. This design change enhances previous work in which a p-ZnTe/CdTe heterointerface was present, devoid of a MgCdTe passivation layer [42].

75 nm	ITO	Electrode
15-20 nm	p-ZnTe: As or Cu	Hole contact
10 nm	i-Mg$_{0.4}$Cd$_{0.6}$Te	Barrier layer
1000 nm	n-CdTe:In (N$_D$=1 x 10^{16} cm^{-3})	Absorber
50 nm	n-Mg$_{0.24}$Cd$_{0.76}$Te:In (N$_D$=5 x 10^{17} cm^{-3})	Barrier layer
500 nm	n-CdTe:In (N$_D$=5 x 10^{17} cm^{-3})	Electron contact
500 nm	n-InSb:Te (N$_D$=5 x 10^{17} cm^{-3})	Buffer
500 μm	n-InSb Substrate	
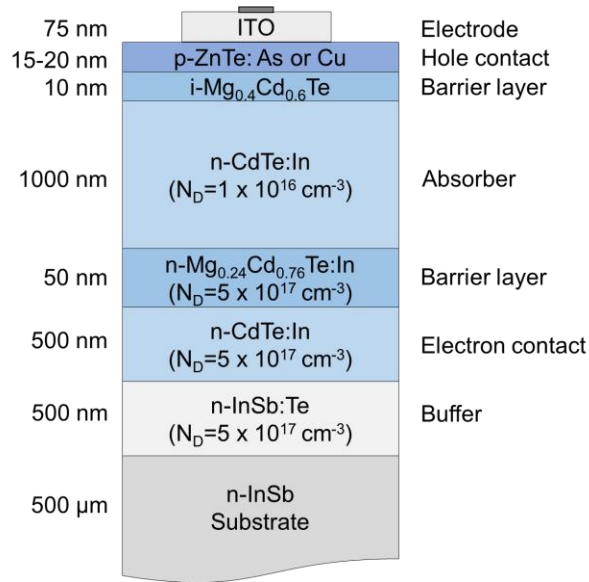
Fig. 16 Layer structure of the CdTe/Mg$_x$Cd$_{1-x}$Te double-heterostructure solar cell with a p-type ZnTe contact layer.

CV measurements on these structures—both copper-doped and arsenic-doped—confirm the formation of a built-in voltage of over 1.1 V as shown in Fig. 17. These measurements are carried out using a mercury probe prior to the deposition of the ITO and silver contacts.
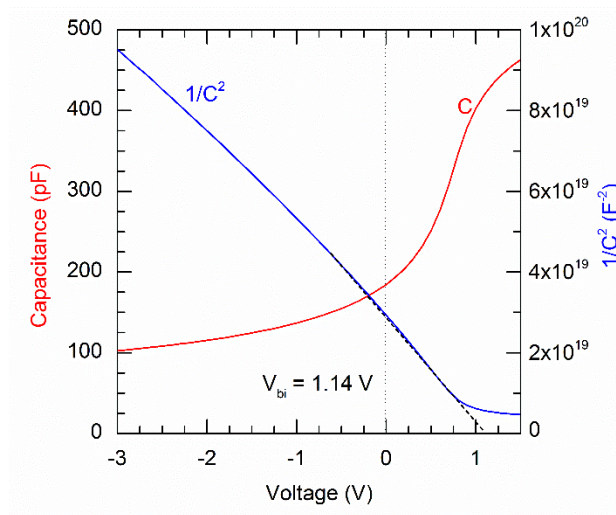
Fig. 17 C-V and 1/C^2 profile for a solar cell with a copper-doped ZnTe hole contact. This measurement was taken using a Hg probe prior to ITO deposition and without any high temperature annealing process.

34

The current density-voltage (J-V) curve for the highest efficiency ZnTe:As based device is shown in Fig. 18 a) with the external quantum efficiency (EQE) and reflectance shown in Fig. 18 b). TABLE 3 compares the V_{oc} and power conversion efficiency (η) for several device structures, each with a different type of ZnTe hole contact. The introduction of the MgCdTe barrier clearly results in an improvement in V_{oc}, no matter the hole contact used. The arsenic-doped ZnTe hole contact provides a higher V_{oc} and efficiency than that of the copper-doped contact (ZnTe:Cu), with copper diffusion being a potential cause.
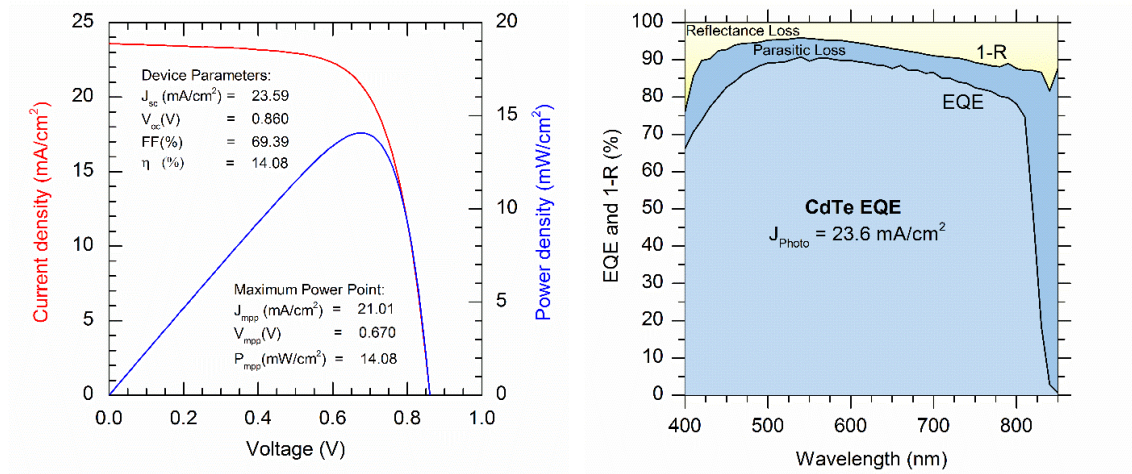
Fig. 18 a) Light J-V curve and power density, and b) EQE and 1-reflectance for the highest performing CdTe double-heterostructure solar cell with a ZnTe:As hole contact. The J-V curve represents an active-area efficiency corrected using the integrated EQE. This device was processed and characterized without the use of an additional anti-reflection coating.

TABLE 3
MAXIMUM DEVICE PARAMETERS
FOR VARIOUS ZNTE CONTACT DESIGNS

	ZnTe:As/ CdTe	ZnTe:Cu/ MgCdTe/CdTe	ZnTe:As/ MgCdTe/CdTe
J_{sc} (mA/cm^2)	21.2	22.2	23.6
V_{oc} (V)	0.759	0.819	0.860
FF (%)	67.4	51.7	69.4
η (%)	10.9	9.4	14.1

3.2.2 Devices using copper zinc sulfide

The isolation of the absorber from the hole contact layer means that the quality of the contact layer is largely irrelevant with respect to maintaining a high quasi-Fermi level separation. Thus, the design does not necessitate crystalline materials like ZnTe, but indeed, can accommodate defective layers in the form of multi-crystalline or amorphous material systems. Copper zinc sulfide ($Cu_xZn_{1-x}S$) is a semi-transparent conducting material. CuZnS films synthesized via chemical bath deposition (CBD) are comprised of a nanocomposite mix of independent sphalerite ZnS and covellite CuS crystals. In general, higher concentrations of the CuS phase lead to a higher hole conductivity and carrier concentration. The bandgap of the films can be varied from 2.1 eV to 3.45 eV by adjusting the films composition from pure CuS to ZnS. The wide bandgap, high hole concentration, and high conductivity all lend themselves to making a great hole-contact material. With the hole contact lying on the light incident side of the device, outside of the CdTe double heterostructure, absorption within this layer is generally lost to non-radiative recombination. The transparency of the material used is therefore very important. Fig. 19 shows a structure diagram of the studied devices. Because of the changing carrier concentrations and conductivity within the CuZnS layers, an additional ITO is required for low copper compositions but is used in all cases to maintain symetry among samples. The nature of the deposition technique leads to difficulties in precisely controlling the thickness of CuZnS films. As the growth speeds of the CuS and ZnS crystals differ, the thickness of the films can vary; the films estimated thickness is between 10- and 20-nm.
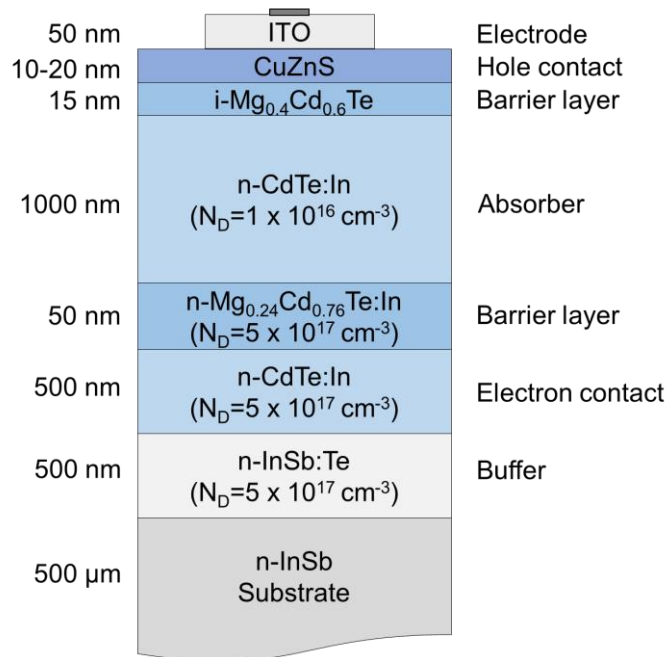
Fig. 19 Layer structure of the CdTe/$Mg_xCd_{1-x}Te$ double-heterostructure solar cell with a CuZnS hole-contact layer.

Measured current-voltage curves for solar cell devices of different copper compositions are shown in Fig. 20.
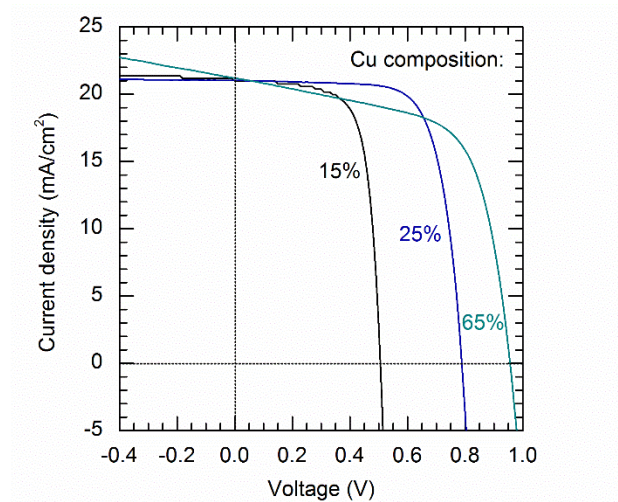
Fig. 20 EQE corrected J-V curves for solar cells with CuZnS hole contacts of 15%, 25% and 65% copper compositions. The devices under test have a total area of 0.033 cm^2 with approximately 1.5% metal coverage.

TABLE 4
ACTIVE-AREA DEVICE PARAMETERS

Cu	V_{oc} (V)	J_{sc} (mA/cm^2)	FF (%)	η (%)
15%	0.506	21.0	71.8	7.6
25%	0.788	21.0	73.0	12.1
65%	0.956	21.2	63.5	12.9

With increasing copper content, the carrier concentration within the contact layer will increase, thereby improving the built-in potential. A corresponding increase in the V_{oc} with copper composition is apparent in the light J-V curves shown in Fig. 20 as well as indicated in TABLE 4. With a copper composition of 65%, a V_{oc} of 0.956 V is achieved. While the V_{oc} is still higher than those measured with polycrystalline devices [3], the W_{oc} of 0.544 V for this particular device is still similar given the smaller bandgap of polycrystalline devices.

Along with the increase in carrier concentration comes a dramatic improvement in layer conductivity. With a CBD process, this can be extremely problematic if the back contact or sidewalls are not adequately covered during the deposition. A short between the CuZnS hole contact and the electron contact would manifest itself as a shunt conductance in the J-V curve as we can see in the case of the device with a 65% copper composition in Fig. 20. Sidewall deposition may still be an issue in the case of all devices but for a layer with only 15% or 25% copper incorporation, the conductivity may not be high enough to dramatically reduce the FF of the J-V curve. The shunt conductance observed in the J-V curve does not necessarily have to plague future devices. Better isolation through a more controlled process such as sputtering or simply dicing all wafers post CBD growth can most likely result in the same voltages and current generation while simultaneously ensuring an improvement in the FF. Assuming these values are not affected, equation (7) can be used

to approximate the maximum power (P^*_{MP}) without the power lost in a shunt resistance. Improving the 290 $\Omega \cdot cm^2$ shunt resistance measured in the light J-V curve could lead to an improvement in efficiency up to 15.3%.

$$P^*_{MP} = P_{MP} \left(1 - \frac{1}{r_{SH}}\right)^{-1} \tag{7}$$

Unexpectedly, the J_{sc} has not changed considerably with an increasing density of CuS crystals within the nanocomposite. The external quantum efficiency (EQE) curves shown in Fig. 21 indicate that the overall quantum efficiency within the device is not significantly changed with a change in copper composition. The small change in refractive index does however result in a shift of the reflectance minimum. However, the absorption within the CuZnS layer does indeed change with copper composition as seen in Fig. 22. As the copper content increases, so too does the absorption within the layer. The reason the large reduction in parasitic absorbance loss seen when moving from CuZnS layers of 25% to 15% copper is not translated into an improvement in the EQE as well can be explained through a compensating reduction in collection efficiency across the spectrum due to the depletion of the hole contact layer due to the low carrier concentration in this layer.

Of course, the differences in reflection will not necessarily be evident in a fully optimized device as the differences in refractive index will be accounted for during the optimization of any additional anti-reflection layers added to the design. In addition, as contacts move to higher copper compositions, it may no longer be necessary to utilize a highly conductive ITO layer for lateral current flow. However, this design may still be desirable to allow for the hole contact to be as thin as possible to minimize parasitic absorption loss within this layer; absorbance within the ITO is considerably lower than in CuZnS films.
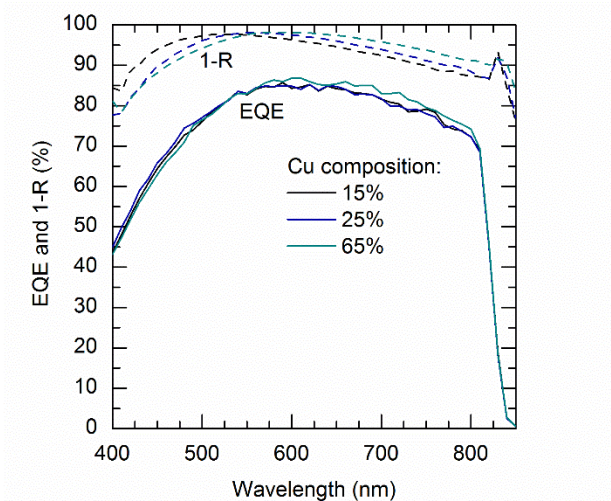
Fig. 21 EQE and 1-R curves for solar cells with CuZnS hole contacts of 15%, 25%, and 65% copper compositions. Both EQE and R were measured at the center of the devices with a beam spot size smaller than the aperture.
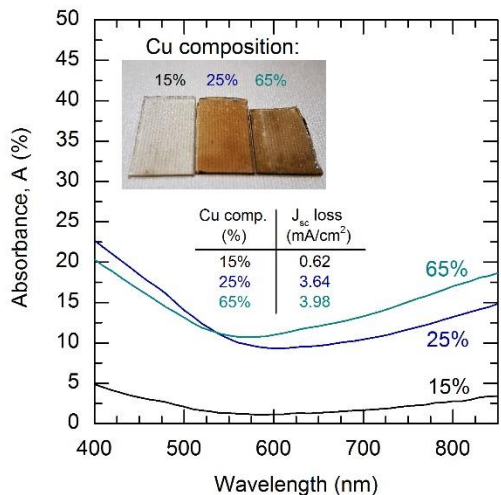
Fig. 22 Absorbance within CuZnS contacts of 15%, 25%, and 65% copper compositions. The parasitic current loss within the hole contact layer for each copper composition is also shown; the curves are weighted against the solar spectrum and integrated below 825 nm. The inset image shows the CBD deposited films on glass. Absorbance measurements were carried out using a spectrophotometer equipped with an integrating sphere.

3.2.3 Devices using amorphous silicon

Amorphous silicon offers a similar contact solution with a well-established, lower-cost deposition process and the capability to achieve very high hole densities. This same material system is utilized in double-heterostructure designs within the record holding HIT solar cells in which a-Si:H is utilized to passivate the surfaces of a multi-crystalline silicon absorber [36]. At this point, the heavily doped p-type a-Si:H contact has little to no effect on the crystalline absorber quality as is the case with the CdTe devices discussed here. The p-doped amorphous silicon layer was deposited after air exposure, without prior surface treatment, by plasma-enhanced chemical vapor deposition (PECVD) in a P-5000 tool using Silane, hydrogen and tri-methyl boron, at a pressure of 2.5 torr, a nominal susceptor temperature of 250 °C and a radiofrequency (RF) power of 36 W. Unfortunately, of the three options discussed thus far, a-Si:H has the lowest bandgap (1.8 eV) and thus parasitic absorption will play the biggest role in these devices.

One option to reduce the parasitic absorption observed in both simulations and measurements is to thin the a-Si:H hole contact. The EQE curves shown in Fig. 23 show just such an improvement in the blue wavelengths. However, thinning much below 8 nm results in a reduction in V_{oc} and FF that we attribute to depletion of the hole contact by the adjacent n-type ITO layer [44]. As can be seen from the inset table, at 6 nm the contact layer is depleted to the point that the V_{oc} and FF reduction dramatically outweighs the J_{sc} benefit. For this reason, the EQE curves shown were measured under reverse bias to ensure complete carrier collection. The dramatic changes in the Light J-V curves can be seen in Fig. 24.
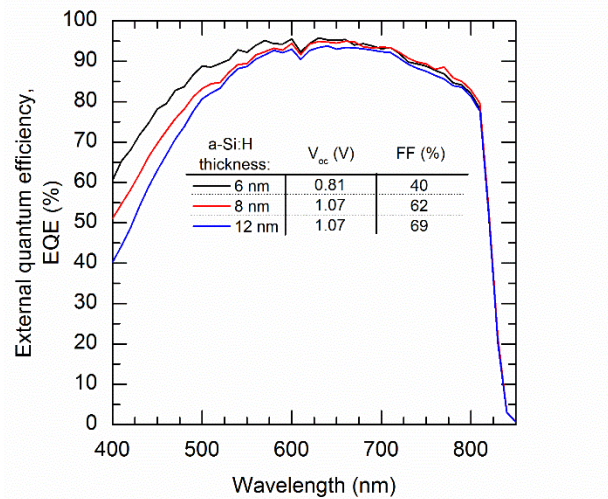
Fig. 23 EQE comparison for devices with different a-Si:H layer thicknesses. The inset table shows the devices' corresponding V_{oc} and FF under AM1.5G illumination. The dip at 610 nm is an artifact of the measurement tool. All EQEs were measured under reverse bias to ensure complete carrier collection.
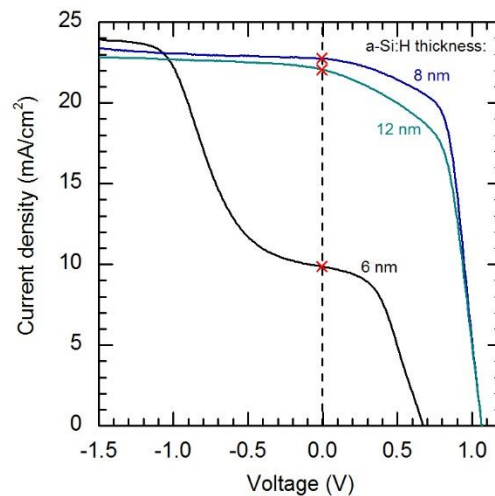
Fig. 24 IV comparison of CdTe solar cells with hole-contact layer thicknesses of 6-, 8-, and 12-nm.

On the front of the device, a silicon oxide (SiO_x) layer was added on top of the ITO electrode, following the design suggested by Herasimenka et al. [45]. It serves as the upper layer of a double-layer anti-reflection coating and increases the conductivity of the ITO due to the hydrogen treatment experienced during the higher-temperature hydrogen-

containing SiO_x growth [45]. With this design, the ITO can be thinned, thereby reducing the level of parasitic absorption in this layer. The thickness of the SiO_x layer was optimized through OPAL simulations to minimize the AM1.5G-weighted front-surface reflectance [46].

Fig. 25 shows the simulated front-surface reflectance and front-stack (a-Si:H, ITO, and optional SiO_x layers) absorbance for a device with and without SiO_x included within the contact stack. The corresponding J_{sc} losses, calculated by integrating over the solar spectrum between 300 nm and 830 nm, are reduced from 3.3 mA/cm^2 to 0.6 mA/cm^2 for the reflection loss and from 2.6 mA/cm^2 to 2.2 mA/cm^2 for the parasitic absorption loss. An increase in photogenerated current density of 3.1 mA/cm^2 is thus expected over earlier designs. Top surface reflection therefore no longer makes up the majority of the optical loss while parasitic absorption within the contact stack now becomes the primary concern when addressing the J_{sc} of these devices.

To validate the modeled absorptance of the stack, all three layers—SiO_x, ITO, and a-Si:H—were deposited on glass and measured using a UV-Vis spectrophotometer. Absorption within the individual SiO_x, ITO, and a-Si:H layers is difficult to experimentally parse as the inter-diffusion between these three layers within the completed device unavoidably changes the absorbance contribution from each layer (hydrogen doping of the ITO from both adjacent layers is one of these changes [46]–[48]). A qualitative distinction between contributions from each layer can be made, however. The SiO_x layer used here is nearly 100% transparent over all the investigated range. The ITO is responsible for all absorption at wavelengths above 600 nm, for which the very thin a-Si:H layer absorbs negligibly. Below 400 nm, both the ITO and a-Si:H contribute to parasitic absorption, but

the clear majority of the absorption, originating from the 400 nm to 600 nm range and adding up to 1.6 mA/cm^2, can be attributed to the a-Si:H contact layer. A full exploration of the hero device will be presented in the following chapters.
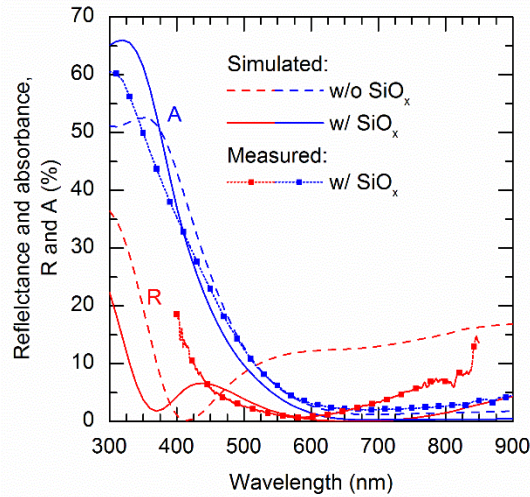
Fig. 25 Simulated and measured front-stack absorbance and reflectance for a CdTe device with either an ITO/a-Si:H layer stack or a SiO$_x$/ITO/a-Si:H layer stack. Simulations were carried out using OPAL.

3.2.4   Contact summary and comparison

ZnTe was chosen because of its ability to achieve high hole concentrations inducing high built-in voltages, but of similar importance is the wide bandgap of ZnTe which allows for less parasitic absorption when compared with other amorphous or poly-crystalline hole contacts such as a-Si:H and CuZnS contacts tested. The internal quantum efficienies (IQE) of three hero device designs are shown in Fig. 26. With the use of ZnTe:As as the hole contact, parasitic absorption at shorter wavelengths (< 600 nm) is minimized when compared to both other contacts. The difference in IQE corresponds to a 1.25 mA/cm^2 gain of potential photogenerated current when using ZnTe instead of a-Si:H. This represents nearly 7% of the maximum J$_{sc}$ attainable for a bandgap of 1.5 eV. The copper-doped ZnTe hole contact shows the same improvements in quantum efficiency at shorter wavelengths

44

and consequently demonstrates similar improvements in current. This large current differential taken from the IQE is not necessarily born out in the current comparison between the highest performance devices shown in TABLE 3 as the ZnTe based devices will have a significantly different reflectance than that of the the a-Si:H based devices; a proper comparison of the final currents would need to be made after each device has an optimized anti-reflection coating; this same reasoning applies to the devices developed using CuZnS.
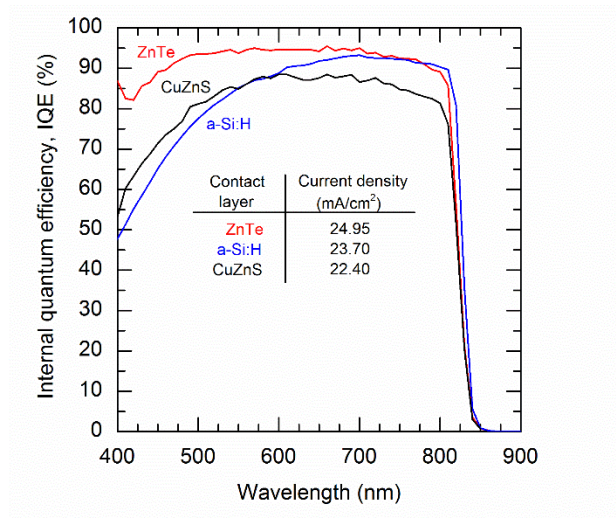
Fig. 26 IQE of CdTe solar cells with three different hole contacts: ZnTe:As, a-Si:H, and CuZnS. The listed current density is found by integrating the IQE weighted against the AM1.5G spectrum. These values are not the J_{sc} of each device but merely provide a weighted comparison between the internal quantum efficiencies of the devices.

TABLE 5
MAXIMUM DEVICE PARAMETERS
FOR VARIOUS CONTACT MATERIALS

	ZnTe:As no barrier	ZnTe:Cu	ZnTe:As	CuZnS	a-Si:H
J_{sc} (mA/cm^2)	21.2	22.2	23.6	21.2	24.5
V_{oc} (V)	0.759	0.819	0.860	0.956	1.10
FF (%)	67.4	51.7	69.4	63.5	75.6
η (%)	10.9	9.4	14.1	12.9	20.3

Unfortunately, while the reduction in parasitic absorption goes a long way in moving the ZnTe based solar cells closer towards the efficiency records set by the a-Si:H based cells, the V_{oc} is not simulatneously maintained at this point. Knowing this limitation with current ZnTe deposition methods and dopants, a-Si:H contacts are utilized within the highest efficiency devices for both 1.5 eV and 1.7 eV absorbers. The following chapter discusses the record holding devices.

CHAPTER 4

DEVICE OPTIMIZATION AND IMPROVED PERFORMANCE

In this chapter, optimization of the $Mg_yCd_{1-y}Te$ barrier layers for both the CdTe 1.5 eV and $Mg_{0.13}Cd_{0.87}Te$ 1.7 eV absorbers is carried out to maximize V_{oc}. Completed devices are discussed and characterized, presenting light J-V and EQE curves for the devices with the highest achieved efficiency. CdTe solar cells are demonstrated with a J_{sc} of 24.5 mA/cm^2, a FF of 75.6%, a V_{oc} of 1.1 V, and an active-area efficiency of 20.3%. In addition, $Mg_{0.13}Cd_{0.87}Te$ solar cells are demonstrated with a J_{sc} of 15.0 mA/cm^2, a FF of 63.5%, a V_{oc} of 1.176 V, and an active-area efficiency of 11.2%. The highest measured V_{oc} of 1.11 V, achieved with a lifetime of approximately 100 ns, shows considerable progress when compared to published CdTe results from the past two decades.

4.1 Devices with a 1.5 eV CdTe absorber

4.1.1 Barrier layer optimization

With the upper barrier layer left intrinsic, energy barriers exist for electrons and holes and thus optimization of this layer requires more attention than that of the layer adjacent to the electron contact. Fig. 27 shows the average and maximum V_{oc} of a series of solar cells of similar design but of varying barrier width and height (magnesium composition, x) for the front $Mg_yCd_{1-y}Te$ layer. As anticipated from PL and TRPL studies of CdTe double heterostructures [49], the V_{oc} rises as the front barrier height or width increases, further confining electrons to the CdTe absorber layer with thermionic emission and tunneling suppressed. While the $Mg_yCd_{1-y}Te$ layer does in fact still provide adequate passivation of the interfaces themselves at the edge of the CdTe absorber, no matter the thickness, the *effective* interface recombination velocity includes the loss of carriers to non-radiative

recombination at the surface or more defective contact layer due to tunneling *through* or thermionic emission *over* the barriers. Tunneling is therefore an issue for barriers of only 5- to 10-nm while thermionic emission becomes a problem for barriers of lower magnesium compositions. Both of these upwards trends are exhibited quite clearly for a CdTe absorber in Fig. 27. Although this same level of barrier optimization within the final device has not yet been carried out for the wider bandgap MgCdTe absorber, similar behavior can be seen in the PL comparison discussed in the next section. Maximizing this effect though, by increasing either the barrier thickness or height will not necessarily result in an increase in efficiency within an actual device. Providing confinement for electron majority carriers must be pursued while simultaneously ensuring that the accompanying barrier in the valence band does not become so large as to dramatically reduce the FF by limiting hole transport into the a-Si:H contact. In addition to the potential drop in FF, increasing the magnesium content further is expected to result in a lower quality interface as the strain increases. Whereas prior studies with similar double-heterostructure samples have shown that barriers with magnesium compositions as high as 46% can be made with high-quality interfaces [50], the PL intensity and implied-V_{oc} degrades as the magnesium composition in the barriers approaches 60%. Also, even though the trend shown in Fig. 27 might encourage the pursuit of even thicker barriers layers, this is believed to be counter productive at this point as the maximum V_{oc} with a 15-nm-thick barrier (1.11 V) already reaches the maximal iV_{oc} (1.13 V) for such an absorber, calculated from η_{ext} measurements [43]. Moreover, with this barrier layer being intrinsic, the conductivity is very low and the FF would suffer considerably as this layer thickness increases. This is, once again, not

believed to be as big of an issue at the backside of the device as the barrier layer on the opposite side of the absorber is heavily doped.
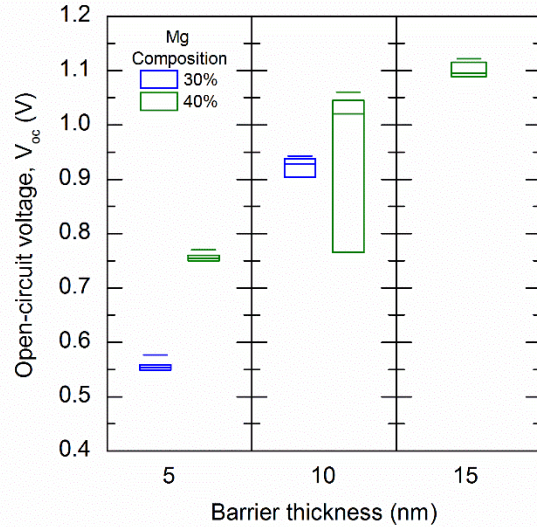
Fig. 27 Box plot indicating the V_{oc} for solar cells with different front MgCdTe layer barrier thicknesses and heights (magnesium composition). The boxes indicate the average values and upper and lower quartiles of all cells on the same wafer; the uppermost lines indicate the maximum values measured.

While the poor performance of the devices utilizing a thin MgCdTe barrier can be partially explained by the increased ability for electrons to tunnel through the barrier and recombine non-radiatively, either in the contact layer or at the surface, there are other potential concerns when using thin barriers in a solar cell structure. During device fabrication, it is highly likely that the upper MgCdTe barrier layer will be exposed to atmosphere prior to the deposition of the contact layer. With MgTe being an extremely hygroscopic material, high magnesium compositions even in the MgCdTe ternary can lead to considerable oxidation of this layer. For thin layers, it is possible for the barrier to oxidize completely resulting in the destruction of the high quality CdTe/MgCdTe interface and thus a dramatic increase in the interface recombination velocity. The transmission electron

microscopy micrograph shown in Fig. 28 shows the oxidation of the interface between the MgCdTe barrier layer and the upper contact layer.
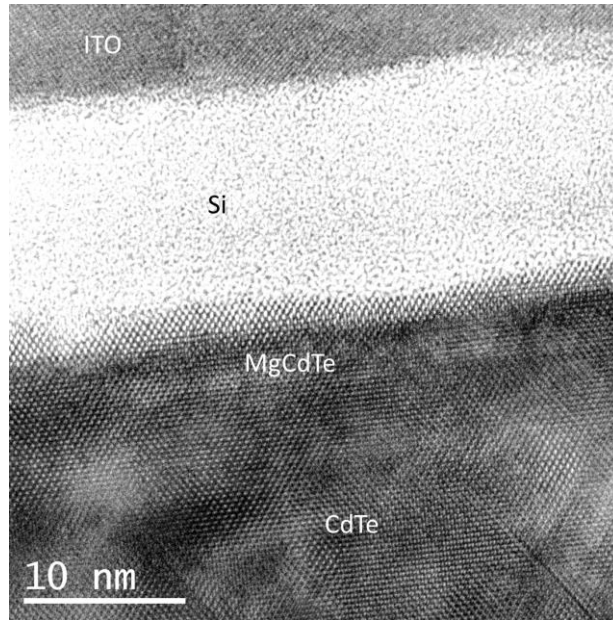
Fig. 28 TEM image of the upper layers of a CdTe/MgCdTe double-heterostructure solar cell with an a-Si:H contact. TEM images provided by Brian Tracy and Dr. David Smith at the LeRoy Eyring Center for Solid State Science.

And yet the presence of a thin oxide layer within the contact stack is not necessarily detrimental to the performance of the solar cell. Fig. 29 depicts the average parameters for solar cell samples with varying degrees of MgCdTe oxidation. Perhaps the most intriguing change with a thicker oxide layer is the increase in V_{oc}. What was originally believed to be a significant downside to using MgCdTe as a barrier layer has proven to be a relatively benign occurrence when barriers are of sufficient thickness so as not to completely oxidize. In fact, the record performing devices discussed in this chapter were intentionally exposed to air for one week prior to contact layer deposition.
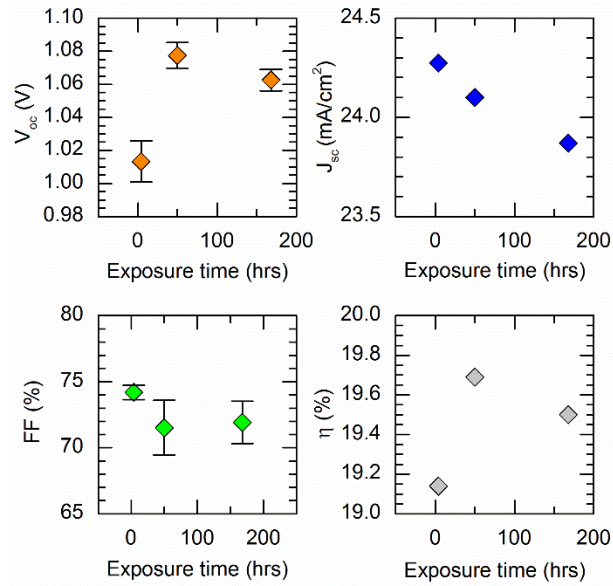
Fig. 29 Average V_{oc}, J_{sc}, FF, and η for three samples in which the intrinsic MgCdTe passivation layers were exposed to atmosphere for varying lengths of time. Error bars in V_{oc} and FF indicate the standard error of the mean for devices on the same wafer. The J_{sc} data points were calculated by integrating the EQE so an approximate error is not presented.

4.1.2 Demonstration of devices with record performance

Fig. 30 shows a structure diagram for a double-heterostructure solar cell which utilizes an amorphous silicon contact layer along with the optimized barrier designs discussed here and in earlier chapters. Deposition time was adjusted to obtain an 8-nm-thick layer based on the thickness optimization discussed in the previous chapter. A 50-nm-thick layer of tin-doped indium oxide (ITO, 95%/5%) was then sputtered on the surface in addition to utilizing the same top and bottom contact processes discussed in Chapter 2. Optical loss is a major component contributing to the reasons why monocrystalline cells constructed in this manner still demonstrate record efficiencies below those of polycrystalline designs—

the best J_{sc} values still fall below 25 mA/cm^2 while the record polycrystalline devices exhibit currents of 30 mA/cm^2.
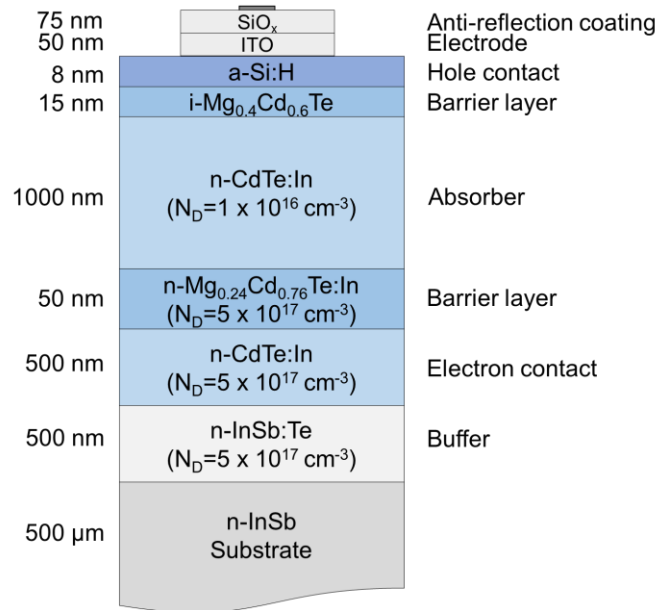
Fig. 30 Layer structure of the CdTe/MgCdTe double-heterostructure solar cell with a p-type a-Si:H contact layer.
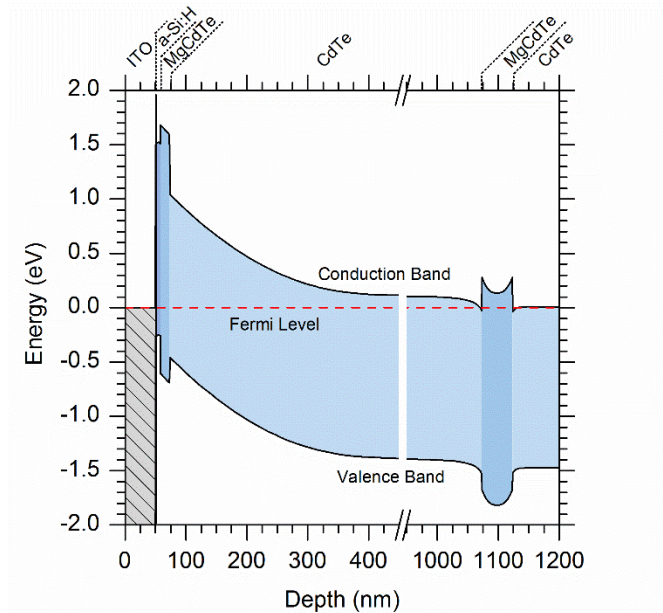
Fig. 31 Simulated band-edge diagram at equilibrium for a CdTe double-heterostructure solar cell with a p-type a-Si:H contact layer. A complete list of the parameters used in the band-edge diagram simulations is shown in TABLE 6.

The simulated band edge diagram shown in Fig. 31 shows that the a-Si:H contact layer, results in a V_{bi} of over 1 V and the CV measurements for these device structures verify this fact with measured V_{bi} values of 1.1 V [51]. The simulated device parameters of the absorber are shown in TABLE 6 with a full breakdown of all material and simulation parameters found in Appendix A.

TABLE 6
PARAMETERS USED FOR BAND-EDGE DIAGRAM SIMULATIONS

	ITO	p- a-Si:H	i-MgCdTe	n-CdTe	n-MgCdTe	n-CdTe
Bandgap	4 eV	1.8	2.284 eV	1.51 eV	1.98 eV	1.51 eV
Magnesium Composition	-	-	0.40	-	0.26	-
Electron Affinity	4.9 eV	3.9 eV	3.738 eV	4.28 eV	3.951 eV	4.28 eV
Doping Density	Degenerate	1×10^{18} cm^{-3}	NA	1×10^{16} cm^{-3}	5×10^{17} cm^{-3}	5×10^{17} cm^{-3}
Intrinsic Carrier Conc.	Metal-like	8×10^{4} cm^{-3}	6×10^{3} cm^{-3}	5×10^{5} cm^{-3}	6×10^{3} cm^{-3}	5×10^{5} cm^{-3}
N_C/N_V	Metal-like	1	0.144	0.144	0.144	0.144
Thickness	50 nm	8 nm	15 nm	1000 nm	50 nm	500 nm

Fully processed devices were tested by the National Renewable Energy Laboratory (NREL). The certified current-voltage curve (J–V curve) and EQE characteristics shown in Fig. 32 indicate a record total-area efficiency of 17.12% and an active-area efficiency of 19.7%—where the active-area is defined as the area within the aperture that is not shaded by metal. The V_{oc} is 1.0919 V—the highest certified value for a CdTe solar cell—and, though the device has appreciable series resistance (discussed in later sections)—there is no rollover in the J–V characteristics. The FF exceeds 70%, which is higher than typical record-V_{oc} devices, for which FF is often sacrificed in order to artificially push V_{oc} higher.
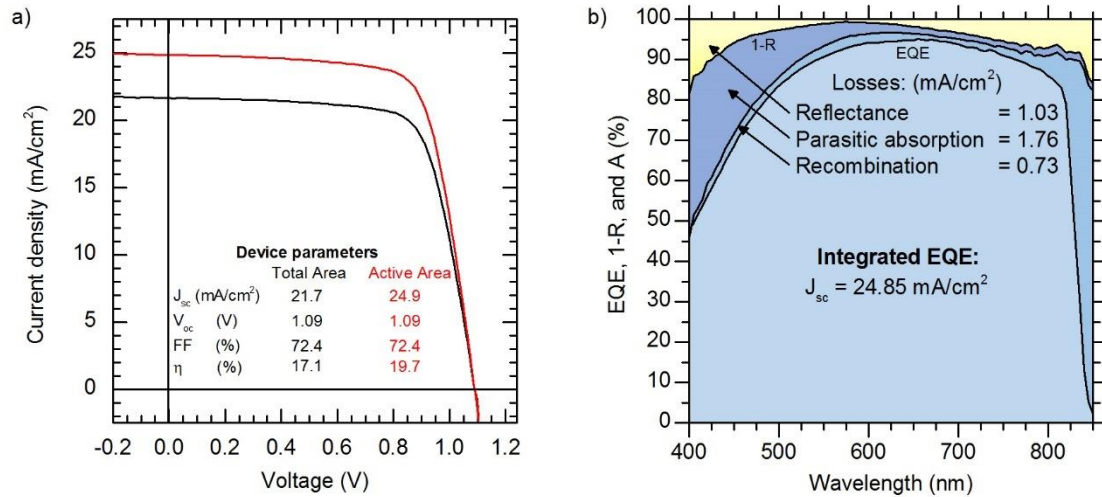
Fig. 32 a) NREL-certified total-area J–V curve (black) and ASU-calculated active-area J–V curve (red) derived from the b) NREL-certified EQE. In addition to the EQE, the device reflectance and contact layer absorption are included with calculated current losses. The device had a total area of 0.06335 cm^2 as defined by a laser-etched silicon mask (measured by NREL) with approximately 13% metal coverage visible within the aperture area.

TABLE 7 lists the in-house measured device parameters from the best cells across the same wafer in which all of the discussed optimizations have been utilized. In all cases, the V_{oc} is above 1 V while the FF is over 70%. The maximum active-area efficiency of 20.3% was measured on a cell with considerable metal coverage explaining the large difference between the total-area and active-area J_{sc}. In the case of the best measured voltage of 1.11 V, the W_{oc} of 0.39 V is considerably lower than the polycrystalline record device. A comparison of published V_{oc} data spanning the past two decades, as gathered by Repins et al., is plotted versus the coresponding minority carrier lifetime in Fig. 33 [52]. A considerable gap in both V_{oc} and carrier lifetime within the device is present in comparison to both the larger grouping of polycrystalline cells as well as to the more recent monocrystalline devices [7]. The double heterostructure design utilized in conjunction with

54

a thinner monocrystalline absorber leads to bulk minority carrier lifetimes sufficient to provide diffusion lengths longer than the absorber thickness.

TABLE 7
MAXIMUM MEASURED DEVICE PARAMETERS

| Device | V_{oc} (V) | J_{sc} (mA/cm^2) | | FF (%) | η (%) | |
		Total-area	Active-area		Total-area	Active-area
1	**1.11**	21.1		72.2	16.9	
2	1.09	**22.6**		74.0	18.2	
3	1.10	21.6		**75.9**	18.0	
4	1.09	22.4		75.7	**18.5**	
5	1.10	18.7	24.5	75.6	15.5	**20.3**
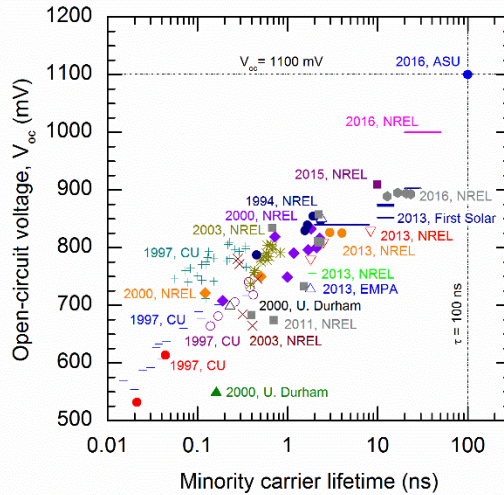
Fig. 33 Published carrier lifetime and V_{oc} data for CdTe devices over the past two decades including the maximum measured V_{oc} presented here [52]. The lifetime was measured in a CdTe double heterostructure with a doping level of 1×10^{16} cm^{-3}.

While this figure indicates that there is little room for improvement in the V_{oc}, there still exists considerable room for improvement in the FFs of these devices. However, pursuit of a higher J_{sc} seems to provide the path of least resistance. The transition to a less absorptive hole contact would allow for a huge reduction in parasitic absorption that has been the primary cause for the difference between the measured J_{sc} and the maximum attainable for a 1.51 eV absorber. Potential candidate materials include high-work-function

metal oxides, p-type dopable chalcogenides, and other II-VI materials. MoO_x—an example of the first—has been used successfully in organic and silcion solar cells [53]; CuZnS—an example of the second—has already been explored but due to difficulties in processing, high efficiencies have not yet been realized; and ZnTe—an example of the third—showed early signs of success in increasing J_{sc} as seen in Chapter 3 but has yet to see voltages beyond 1 V [12].

4.2 Devices with a 1.7 eV MgCdTe absorber

4.2.1 Usage of graded barrier layers

Although very similar to the structure described in the previous section, several design changes are necessary when transitioning to a wider bandgap absorber device. For starters, the absorber thickness is reduced to 500 nm in the hopes of maintaining a higher quality absorber. Secondly, to provide adequate carrier confinement and surface passivation for a wider bandgap absorber as is the case with a magnesium incorporation of 13%, even greater magnesium levels in the barriers than has been previously employed with CdTe based devices is necessary. While CdTe DH designs can utilize abrupt heterointerfaces, this same abrupt change is difficult to achieve for a 1.7 eV absorber as magnesium is present throughout the entire DH and thus the magnesium shutter cannot merely be open and shut to generate the barrier layers as is typically done for the CdTe devices. Using a growth interruption to allow for the magnesium cell temperature to adjust to the required level for the different layers may result in an abrupt heterointerface, but this could result in a lower quality interface. Even under ultra-high vacuum, foreign elements in the chamber can build up at the interface resulting in an increase in the IRV. To generate an abrupt interface, at the completion of the barrier and absorber layer growths, both the magnesium cell and

tellurium cell shutters are closed leaving the surface of the sample under cadmium overpressure. At this point, the magnesium cell temperature is either ramped up or down at a rate of approximately 15 °C/min. Once the desired cell temperature for the subsequent layer is achieved, all shutters can once again be opened and growth can continue. To attain a grading of the composition between the absorber and barrier layers, the magnesium cell temperature is raised or reduced while all cell shutters remain open. The relationship between the cell temperature and the elemental flux is exponential so as the cell temperature changes linearly, the magnesium composition within the graded layer will change exponentially. The equilibrium state band edge diagram shown in Fig. 34 portrays how this grading affects the barrier band edges. In principal, this method of grading— assuming the portion of the barrier containing the maximum magnesium composition remains unchanged, which is the case for the devices discussed below—will result in a thicker overall barrier layer. While this leads to a situation in which there are no discontinuities in the band edges for the absorber, the transition from the pure CdTe in the buffer layer does include a band offset formed by the opening of the magnesium shutter; this is not an issue for electron transport from the absorber into the CdTe contact.
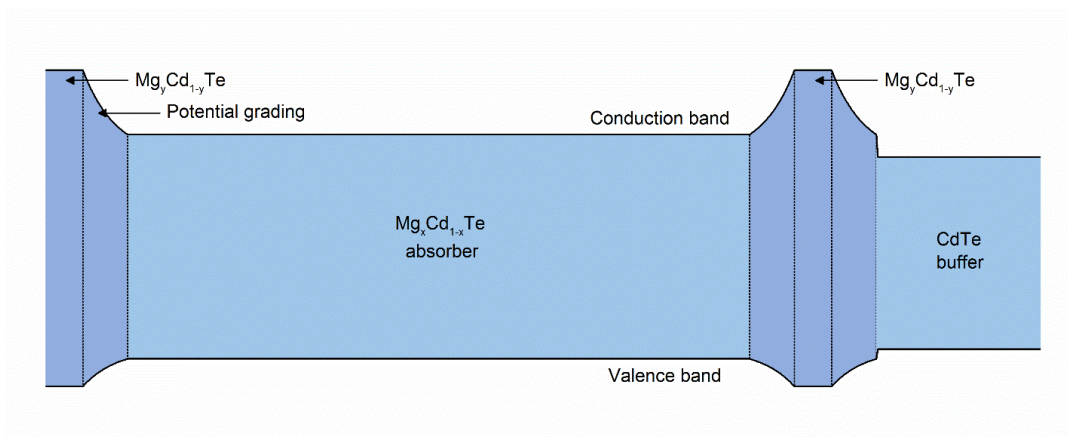
Fig. 34 Schematic band-edge diagram at equilibrium for the MgCdTe DH with graded barrier layers.

Two sets of sample structures were developed to compare the quality of the absorber material when the barriers are either graded or abrupt. The PL intensity for each of these samples is shown in Fig. 35 a) and b). The samples shown in a) have a maximum magnesium composition of 24% within the barrier layers, with one sample containing an abrupt interface between the barrier and the absorber, while the other sample has 10 nm of grading between the barrier and absorber. For a 1.7 eV absorber, a 24% magnesium composition within the barriers does not generate a sufficient enough energy barrier to confine carriers at room temperature. This indicates that higher levels of magnesium are indeed necessary for final device development, yet comparisons can still be made between the samples at low temperature. At 130 K and below, the PL intensity for both samples is nearly equivalent, indicating that grading does not necessarily present any benefit when attempting to maximize the iV_{oc} of the structure.

In light of the fact that barriers with only 24% magnesium cannot be used within a completed device structure, an increased magnesium composition of 50% was also compared as is shown in Fig. 35 b). In this case, the PL is quite high even at room temperature and the η_{ext} of 1.2% gives an iV_{oc} of 1.29 V. This holds true for the sample with and without grading in the barriers with very little difference in intensity between the two. The slight difference in peak position can be explained by a shift in the magnesium flux rate which occurs naturally over time as the cell continues to deplete (cell temperatures are re-calibrated over time as these shifts become apparent). In addition to the PL intensity, the bulk minority carrier lifetimes extracted from the time-resolved photoluminescence decay shown in Fig. 36 are nearly equivalent as well—being measured at approximately 50 ns for both. The 50% magnesium barriers, whether used in conjunction with graded

layers or with an abrupt interface, provide excellent confinement and interface passivation with measured bulk minority carrier lifetimes of up to 560 ns measured in a graded structure [32]. Although oxidation is expected to become more prevalent as compositions move to these higher values, the absorber interface remains untouched by atmospheric degradation even a year after exposure to oxygen began. The 30 nm $Mg_{0.5}Cd_{0.5}Te$ barrier layer, even without a CdTe capping layer, was resilient enough to atmospheric exposure to result in no significant change in PL intensity. This also holds true for both abrupt and graded samples.
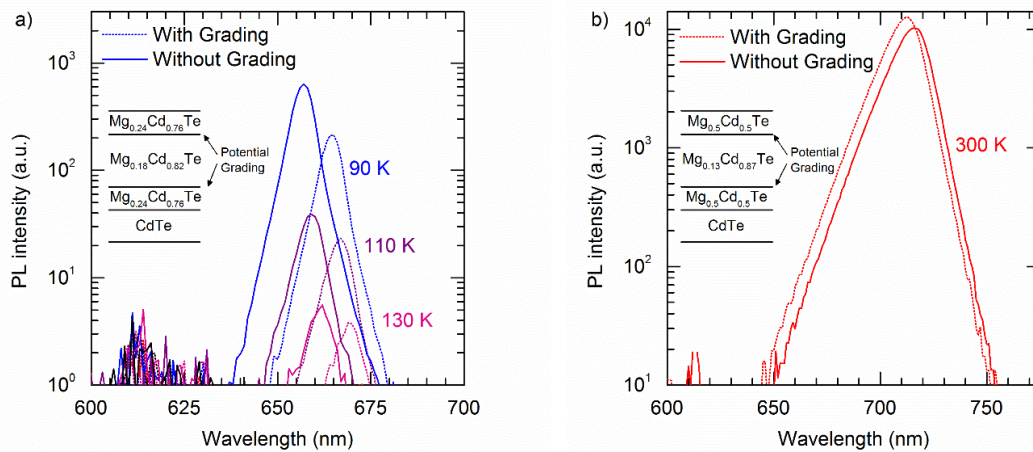
Fig. 35 PL intensity comparing samples with and without grading layers between the barrier and absorber layers. a) compares samples with barrier layers with a maximum magnesium composition of 24%, while b) compares samples with barrier layers with a maximum magnesium composition of 50%.
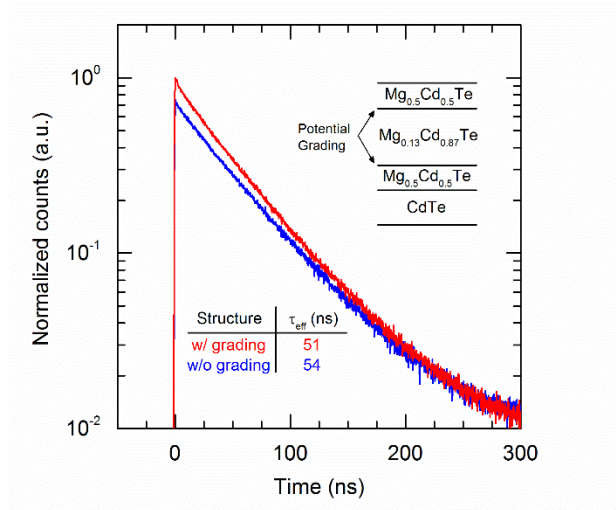
Fig. 36 Normalized room-temperature time-resolved photoluminescence decay for a set of two DH samples, each consisting of two 30nm $Mg_{0.5}Cd_{0.5}Te$ barriers and a $Mg_{0.13}Cd_{0.87}Te$ absorber layer with or without grading. The curves have been shifted along the y-axis for clarity. The fitted lifetimes are shown in the inset table.

4.2.2 Demonstration of devices with record performance

The layer structure in Fig. 37 shows the design changes used when transitioning to a wider bandgap 1.7 eV absorber which include the addition of the graded barrier layers and the thinning of the absorber. The simulated equilibrium state band edge diagram shown in Fig. 38 portrays how this grading affects the barrier band edges. The p-type a-Si:H layer in contact with the top of the DH induces the band-bending in the $Mg_{0.13}Cd_{0.87}Te$ absorber. Because the absorber region is left nominally intrinsic, the bands show a consistent electric field present throughout the entire absorber. With the addition of the grading layers used in conjunction with each barrier layer, a considerable impediment to carrier transport exists, especially considering doping cannot be used to in the electron selective barrier layer.
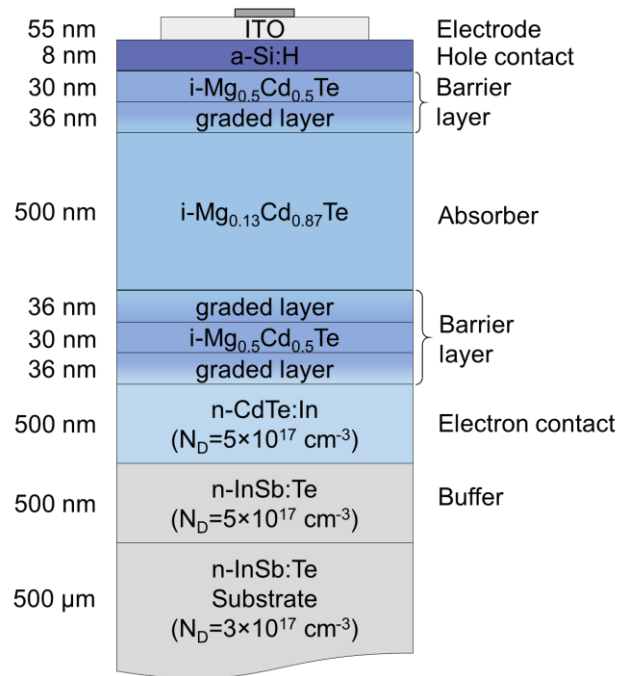
Fig. 37 Layer structure of the $Mg_{0.13}Cd_{0.87}Te/Mg_{0.5}Cd_{0.5}Te$ double-heterostructure solar cell with a p-type a-Si:H hole contact.
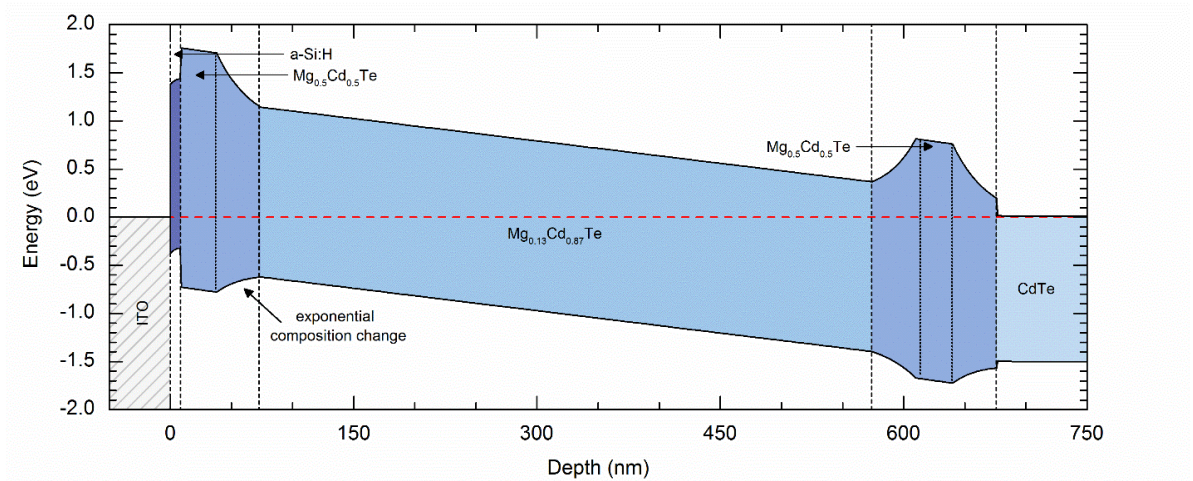
Fig. 38 Simulated band-edge diagram at equilibrium for the MgCdTe solar cell shown in Fig. 37.

Fig. 39 shows the J-V characteristic under illumination and the EQE for the device that has demonstrated the maximum efficiency. The J_{sc} is difficult to accurately determine directly from the J-V measurement even with a mask, due to extreme sensitivity in the determining the area. Thus, the J_{sc} is calculated by integrating the EQE curve with the AM1.5G spectrum and is determined to be 15.0 mA/cm^2 for the highest efficiency solar cell. The measured J-V curve is scaled to match the 15.0 mA/cm^2 J_{sc}. The active-area efficiency (defined to be the efficiency of the unshaded area) is measured to be 11.2%, and accounting for the ~10% metal coverage, the total area efficiency is closer to 10.1%.
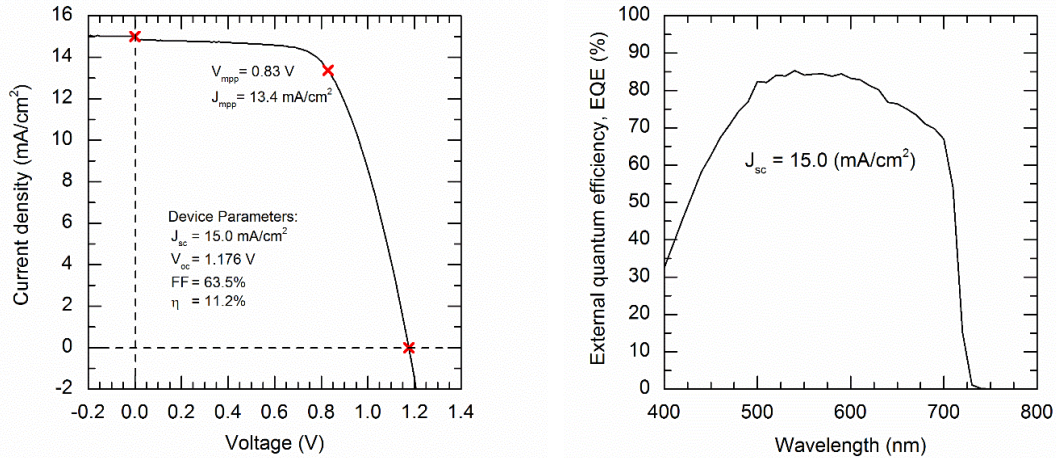
Fig. 39 Device performance of the most efficient cell with area of 5 mm by 5 mm including the light J-V curve under the AM1.5G solar spectrum (left) and the external quantum efficiency (right).

The V_{oc} of 1.176 V is lower than the implied-V_{oc} calculated from luminescence efficiency measurement, and this same discrepancy exists when examining the built-in voltage (V_{bi}) of the device. The C-V and $1/C^2$ plots shown in Fig. 40 indicate that the completed DH device has a maximum potential V_{bi} of approximately 1.42 eV. However, there is a distinct change in the slope of the curve that can be attributed to the band offset at the heterojunction and this can introduce some variance in the V_{bi} depending on where

the curve is fit. Yet, it still stands that the a-Si:H hole contact generates a larger built-in potential across the $Mg_{0.13}Cd_{0.87}Te$ absorber but extracting this potential as a voltage at the contacts is still problematic. The low fill factor (FF) of 63.5%, also implies that the charge transport in this solar cell structure still has ample room for further improvement with the most likely causes being the energy barriers discussed earlier in the paper. Further analysis of the reasons for this FF reduction help to bolster this claim and are discussed in the next chapter.
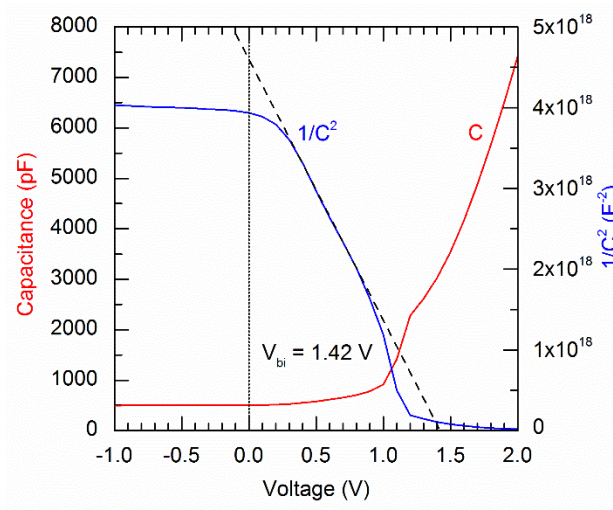
Fig. 40 C-V and $1/C^2$ profile for the MgCdTe solar cell. Five devices across the sample were measured and the data presented represents the device demonstrating the median V_{bi} of 1.42 V calculated as the intersection of the fitted $1/C^2$ profile with x-axis

CHAPTER 5

LOSS MECHANISMS AND ENVISIONED FUTURE DESIGNS

Understanding the underlying reasons for the difference in performance between the devices discussed in the prior chapter and that of the current state-of-the-art poly-CdTe solar cell, exposes a number of pathways for improvement. Chapter 5 discusses several of the different loss mechanisms found within the two different solar cell technologies discussed within this thesis. Beginning with electrical loss mechanisms that effect the FF of the devices, exploration of the impact of the lumped series resistance in the device is modeled and measured to determine a pseudo-FF and efficiency for the devices. The photocurrent loss mechanisms are then discussed through the comparison of the simulated device absorbance within the individual layers and the measured EQE. A series of design changes to address these loss mechanisms and improve the performance of the double-heterostructure design are then considered; this includes absorber bandgap tuning and substrate removal.

5.1   Loss mechanism analysis

5.1.1   Loss mechanisms contributing to lower FF

The J–V curve of the device with the best total-area efficiency was fitted with a one-diode model based on the model developed by Merten et al. [54], as shown in Fig. 41. The parameters used in the model are listed in TABLE 8. The slight slope around short circuit can be fit well with a parallel resistance of only 5 kΩ·cm^2, indicative of slight shunting responsible for a 0.6% FF loss. However, to properly reproduce the shape of the J–V curve between -1 V and the maximum power point (MPP), an additional imperfect collection term has to be used, which we model with a mobility-lifetime product of 3.3×10^{-6} cm^2/V,

responsible for another 1.3% FF loss. Though such a mobility-lifetime product may be unphysical given the microsecond-range lifetime observed in undoped samples, bulk lifetimes within the actual solar cell devices are shorter due to the increased doping concentration (see Fig. 7).
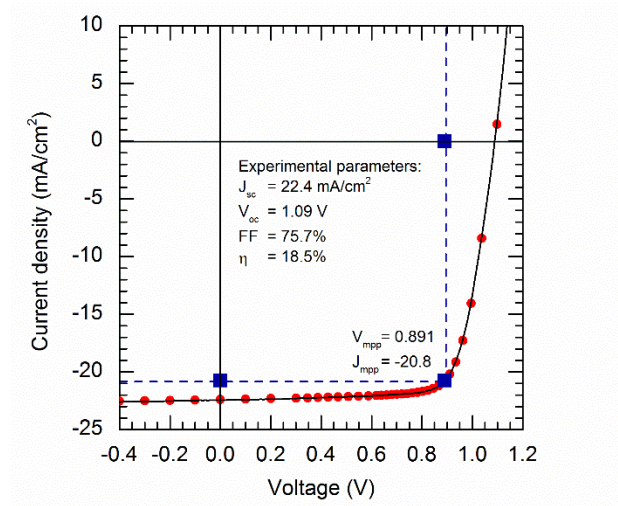
Fig. 41 Experimental and simulated J–V curves of an 18.5%-efficient monocrystalline CdTe solar cell. The curve was fitted with a one-diode model with series resistance, parallel resistance, and recombination terms.

TABLE 8
MODELED DEVICE PARAMETERS

	Value	Unit	Absolute FF loss
Diode saturation current (J_0)	7.7×10^{-13}	mA/cm^2	-
Diode ideality factor (n)	1.4	-	-
Photogenerated current (J_{ph})	22.6	mA/cm^2	-
Effective mobility·lifetime product ($\mu\cdot\tau)_{eff}$	3.3×10^{-6}	cm^2/V	1.3%
Built-in voltage (V_{bi})	1.2	V	
Parallel resistance (R_p)	5000	Ω·cm^2	0.6%
Series resistance (R_s)	4	Ω·cm^2	7.1%

Series resistance is the largest of the loss mechanisms, and an over 7% (absolute) improvement in FF is expected if the resistance can be reduced. About 1% can be attributed to the front electrode (120 Ω/□ sheet resistance of the front ITO, resistive losses in the

finger and contact resistance). The origin of the remaining 6% loss is under investigation, and likely originates in the numerous barriers to charge extraction between the CdTe absorber and the electrodes. The extraction of holes from the p-type a-Si:H to the ITO is expected to yield less than 0.5% loss based on the high FF values attained in silicon heterojunction cells using the same structure [45], leaving more than 5.5% FF loss in the II-VI stack and MgCdTe/a-Si:H interface. The two MgCdTe barriers probably contribute most to the loss, though the share between the front and rear layers is uncertain. In addition to the difference in magnesium composition, different doping densities and thicknesses are used in the front and rear. Varying the thickness and composition of these two barriers would help to elucidate the transport losses and to find an optimum barrier for each side that would minimize the resistance to the extraction of majority carriers while maintaining a low IRV [55].

Electron transport from the CdTe buffer to the InSb wafer and rear metal is expected to be negligible due to the high doping in all layers and the low bandgap of InSb. Indeed, two structures were grown in order to measure the transport across the interface of an n-CdTe on n-InSb structure as well as a n-CdTe on p-InSb structure. The final device structure and associated simulated band diagrams are show in Fig. 42. The structures consist of a 500-nm n-type CdTe layer grown on either an n- or p-type InSb layer. The top indium contact is made to the n-CdTe layer while the bottom contact is made using a Ti/Pt/Au stack on the InSb layer; this is done as opposed to the bottom of the substrate so as to avoid any wafer resistance effecting the vertical transport measurements. Lateral current flow is not believed to dramatically affect the measurements. Reciprocal space mapping on similar structures indicate that, as CdTe is so closely lattice matched to InSb,

66

these layers are coherently strained and the interfaces are relatively defect free [56]. X-ray diffraction peaks for the n-CdTe/n-InSb and n-CdTe/p-InSb devices in question show similarly high quality with full-width half maximums of 22- and 21-arc seconds, respectively.

While the CdTe (1.51 eV) and InSb (0.17 eV) bandgaps were found from literature averages [28] (with the CdTe bandgap verified using photoluminescence measurements), the valence band offset and doping levels were found experimentally for these growths. X-ray and ultraviolet photoelectron spectroscopy measurements performed by Robert Nemanich, et al. found that the valence band offset is approximately 0.90 eV [57]; this value compares really well with both the calculated offset of 0.86 eV and previous experimental results of 0.87 ± 0.10 eV [17], [58]. For the n- on n- case shown in Fig. 42 b), the barrier is approximately 8 nm wide with a height of roughly 240 meV. For the tunnel junction shown in Fig. 42 c), the degenerate doping levels on both sides of the interface results in only a 15 nm distance encountered during the band-to-band transition with no energy change.
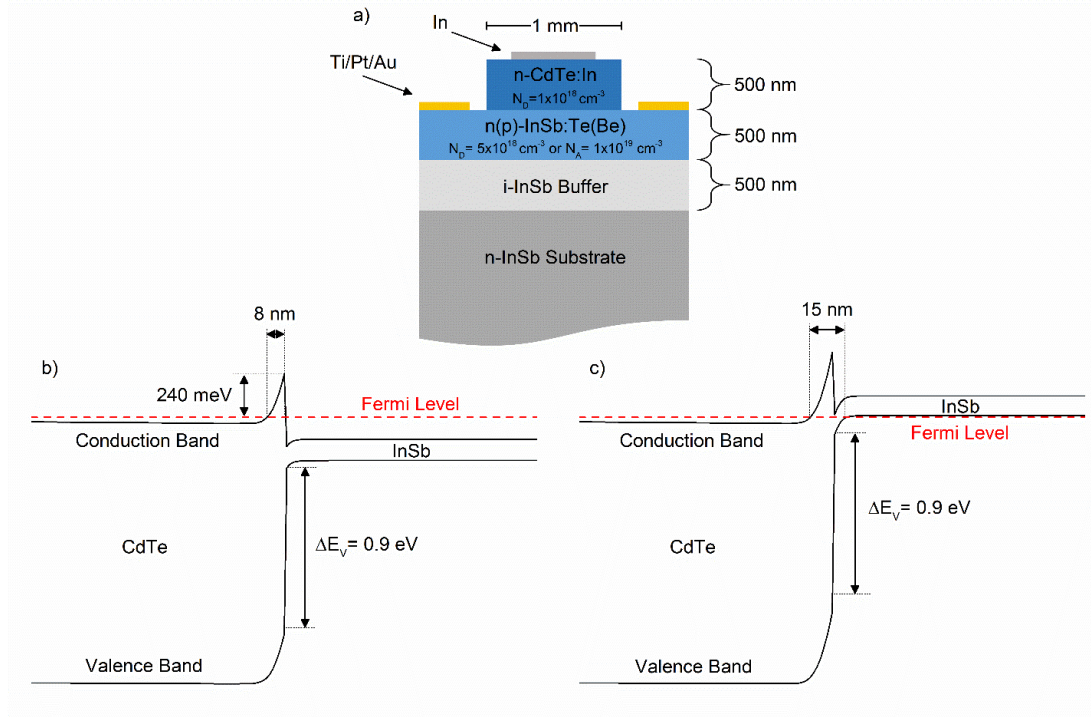
Fig. 42   a) Device layer structure and band edge diagrams for n-type CdTe grown on b) n-type and c) p-type InSb. Diagrams were plotted using PC1D, a one-dimensional transport simulation software.

Standard tunnel-junction formation results from extremely high doping of both layers at the interface. This heterointerface functions particularly well in this regard as the primary n-type dopant used within CdTe is indium—a dopant that will inevitably diffuse in from the InSb layers, thereby increasing the doping concentration at the interface. Secondary ion mass spectroscopy (SIMS) results shown in Fig. 43 indicate that while the targeted doping level within the bulk of the CdTe film of 1×10^{18} cm^{-3} is maintained (verified through C-V measurements), the doping density is over three times higher ($\approx$ 3.6×10^{18} cm^{-3}) at the CdTe/InSb interface. Indium from the lower InSb layers has diffused up to 150 nm from the interface under no additional annealing—that is, outside of the substrate temperature and time of the CdTe layer growth itself. This is not an insignificant change with respect to the barrier formation in the conduction bands. While the barrier

68

widths with a doping level of 3×10^{18} cm^{-3} shown in Fig. 42 b) and c) are 8 nm and 15 nm, they would increase in width 2- to 3-times with only a small reduction in doping to levels at 10^{18} cm^{-3} or below. This diffusion has a much larger, relative effect when occurring in the solar cell structures in which case the absorbers are doped several orders of magnitude lower and the cells are exposed to higher temperatures for a greater period of time during growth and processing; this was seen and discussed in Chapter 3.
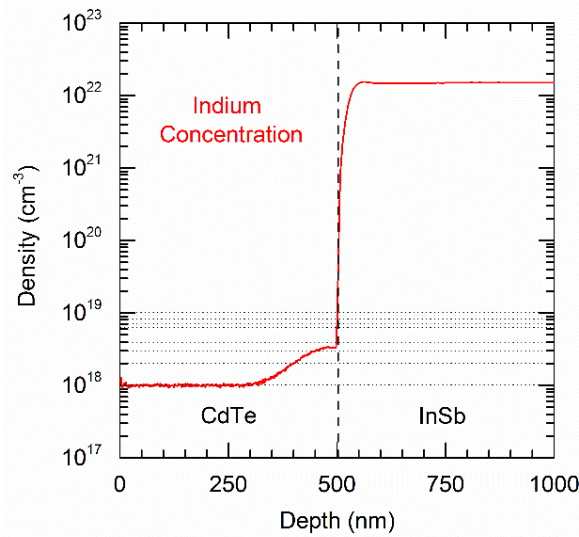
Fig. 43   Secondary ion mass spectroscopy results for an indium doped CdTe layer on a tellurium doped InSb layer. The indium doping density in the CdTe layer was calibrated using CV measurements while the indium concentration in the InSb layer is based on the calculated density.

J-V measurements were performed to test the vertical transport across the two different interfaces. The results shown in Fig. 44 a) reveal the ohmic behavior of the n-CdTe/n-InSb interface at both room- and low-temperatures with no discernable change in the resistance. The tunnel junction on the other hand, while nearly-ohmic at room temperature, is rectifying at lower temperatures. TABLE 9 reports all the resistances measured. The contact resistances are treated as having a negligible impact on the measurements as they are measured at several orders of magnitude lower than the resistance of the stack; this is after

a 200 °C anneal for 2 minutes. In addition, the semiconductor resistances of the vertical transport through the CdTe and the lateral transport through the InSb are ignored due to the thin 500 nm CdTe layer and the extremely high conductivity of the InSb. With these resistivity levels, for normal solar cell device operation at currents under 30 mA/cm^2, the voltage drop at the interface will be significantly less than 1 mV.
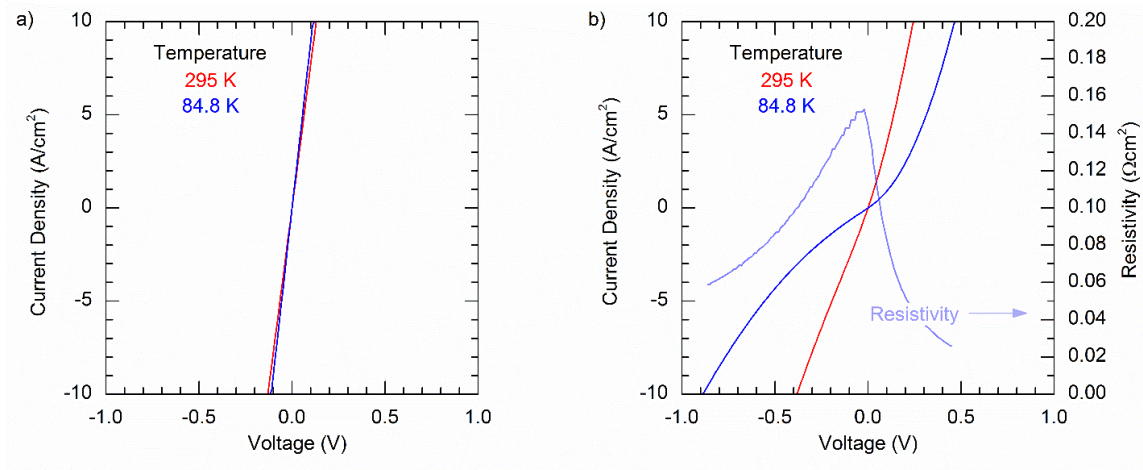
Fig. 44   I-V measurements at room- (295 K) and low-temperature (84.8 K) for both the a) n-CdTe/n-InSb and b) n-CdTe/p-InSb structures. All measurements were taken under vacuum using a two-point probe and Keithley multimeter, with low temperature measurements completed using liquid nitrogen cooling.

TABLE 9
MEASURED RESISTANCES OF ALL RELEVANT CONTACTS AND HETEROINTERFACES

	ρ_c ($\Omega \cdot cm^2$)	295 K ρ_s ($\Omega \cdot cm^2$)	84.8 K ρ_s ($\Omega \cdot cm^2$)
In on n-CdTe	1.2×10^{-4}	--	--
Ti/Pt/Au on n-InSb	1.1×10^{-6}	--	--
Ti/Pt/Au on p-InSb	6.9×10^{-5}	--	--
n-CdTe on n-InSb	--	0.013	0.011
n-CdTe on p-InSb	--	0.033	*See Fig. 3 b)

The convex shape of the J–V curve between -1 V and MPP seen in the fitting of the J-V curves is characteristic of a collection issue and not (Ohmic nor non-Ohmic) shunting. The transport-related origin of this FF loss is also confirmed by the variable-illumination V_{oc} (commonly called Suns-V_{oc} of J_{sc}-V_{oc} if the J_{sc} is measured directly) measurements which were carried out on devices of the same design, showing a large discrepency between the one-sun FF and the calculated pseudo-FF (a value greater than 80%).

The J_{sc}-V_{oc} curve for this device was attained by measuring the full J-V curve of the solar cell for several different light intensities and extracting the J_{sc} and V_{oc} values. Looking at the standard single-diode model with series resistance shown in equation (8), we can see that at both J_{sc} (V=0) and V_{oc} (J=0), the series resistance has no effect. Understanding this, plotting the extracted J_{sc} and V_{oc} values, inverting the curve, and translating them into the first quadrant, we can visualize a J-V curve minus the effect of series resistance. A comparison of this shifted J_{sc}-V_{oc} curve with the one-sun J-V curve as proposed by Aberle *et. al.,* allows for the calculation of R_S at the maximum power point through the relation shown in equation (9) [59], [60]. From these curves we can establish a psuedo-FF and psuedo-η for these devices indicating the limitations of the design.

$$J = J_L - J_0 e^{\left[\frac{q(V+IR_S)}{nkT}\right]} \tag{8}$$

$$R_{S,Suns-V_{oc}} = \frac{\Delta V}{J_{mpp}} \tag{9}$$

This comparison is shown in Fig. 45. The large series resistance found at the maximum power point produces an even larger absolute FF loss than is predicted by the fitting, with the pseudo-FF calculated to be 86%. This same behavior is exhibited with the MgCdTe devices to an even greater extent. Once again, the pseudo-FF is over 85% with a

considerable amount of loss due to poor transport and a much larger series resistance of 26 $\Omega \cdot cm^2$. One small caveat to consider in this analysis is that R_S is current (illumination) and voltage dependent. While this is typically accounted for with a J_{sc}-V_{oc} comparison and an $R_S(J)$ term can be determined, there are certain assumptions made in this analysis that done necessarily always hold true. Primarily, the saturation or dark current (J_0) is assumed constant over all excitation intensities but this is not the case as recombination terms will change with injection level and voltage. However, for illumination levels resulting in voltages between V_{oc} and V_{mpp}, prior work by Fong *et. al.* has indicated that there is very little error in the calculated $R_S(J)$ and constructing a pseudo-FF in this range is very accurate [61].
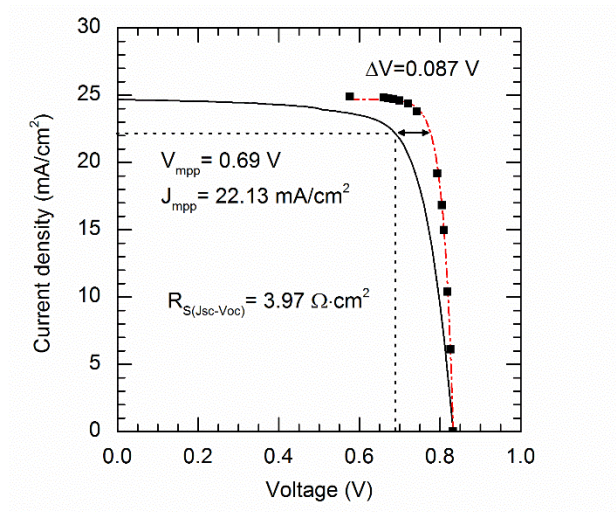
Fig. 45 J_{sc}-V_{oc} data and fitting compared with the 1-sun J-V curve for a 1.5 eV CdTe device to extrapolate the series resistance at the operating point.
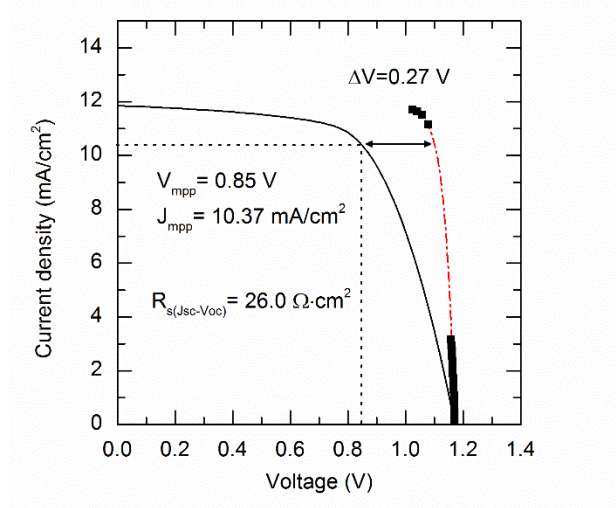
Fig. 46 J_{sc}-V_{oc} data and fitting compared with the 1-sun J-V curve for a 1.7 eV MgCdTe device to extrapolate the series resistance at the operating point.

Further exploration of FF losses can be accomplished through temperature dependent measurements. There are many intrinsic material properties, as well as device properties, that exhibit some level of temperature dependence that will have an effect on the J-V parameters of a solar cell [62]. Perhaps most recognized is the effect temperature has on bandgap as well as the intrinsic carrier concentration. The reverse saturation current density (J_0) is a measure of leakage current in the device and exhibits a strong dependence on n_i^2. With J_0 being a carrier recombination term, it has a strong effect on the V_{oc} of the device as seen in equation (10) derived from the single-diode model:

$$V_{oc} = \frac{kT}{q} \ln \left(\frac{J_{sc}}{J_0} + 1 \right)$$

(10)

It is clear from this relationship that the V_{oc} will drop as the temperature—and thus J_0—increases. This trend can clearly be seen in the temperature dependent J-V parameters for a $Mg_{0.13}Cd_{0.87}Te$ solar cell shown in Fig. 47. The J_{sc} is also seen to be increasing as the bandgap of the absorber decreases and additional portions of the solar spectrum can be

absorbed. Where this device performance deviates from the typical trends observed in other more common device structures is with the FF. While typical devices will show a degradation in FF as the temperature increases and the V_{oc} decreases [62], these devices exhibit the exact opposite behavior. As previously discussed, the barriers in the conduction band at the electron contact and in the valance band at the hole contact are believed to be responsible for restricting majority carrier transport into their respective contacts. This is believed to be the leading cause of the internal lumped resistance. If this is true, an *increase* in FF as opposed to a decrease should be expected as thermal energy is added to the system, thereby increasing the ability for carriers to transport into their respective contacts. Indeed, this trend is observed as the FF increases to 74% with an increase in temperature of 60 °C.
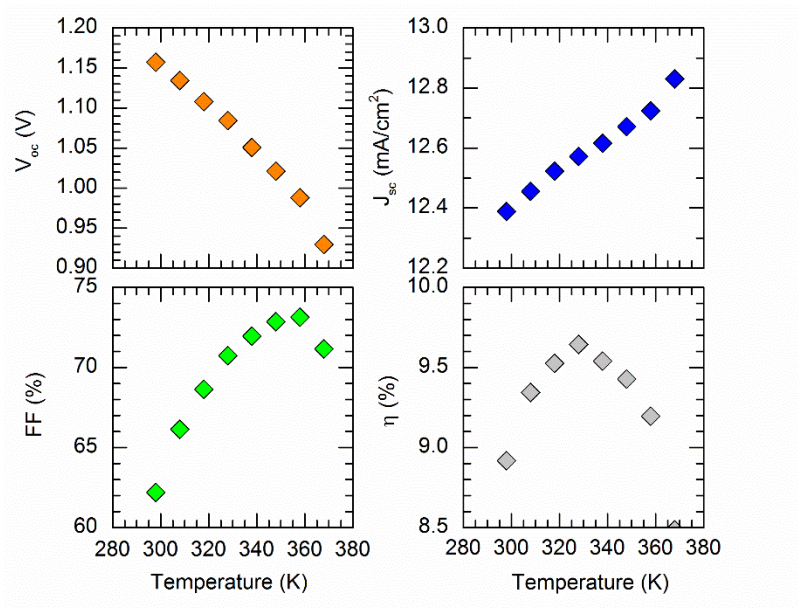
Fig. 47 Extracted device parameters for a $Mg_{0.13}Cd_{0.87}Te$ double-heterostructure solar cell versus device temperature. Temperature is controlled using a hotplate and measured using an attached thermocouple.

This behavior is also present within the CdTe absorber devices as seen in Fig. 48. However, with a significantly smaller barrier to carrier transport, the FF of these devices is already considerably higher at room temperature and very little additional thermal energy is required to negate the resistance due to this barrier. The concern of low conductivity due to an intrinsic absorber is also not an issue with the CdTe devices and thus is not considered a contributor to any series resistance within the device. This can be observed in the halt of the increasing FF at temperatures beyond 320 K and eventually revert to the downwards trend commonly seen in solar cell devices. The V_{oc} and J_{sc} continue to change with temperature as expected and the efficiency will therefore roll over and degrade at an increased rate after the FF begins to plateau.
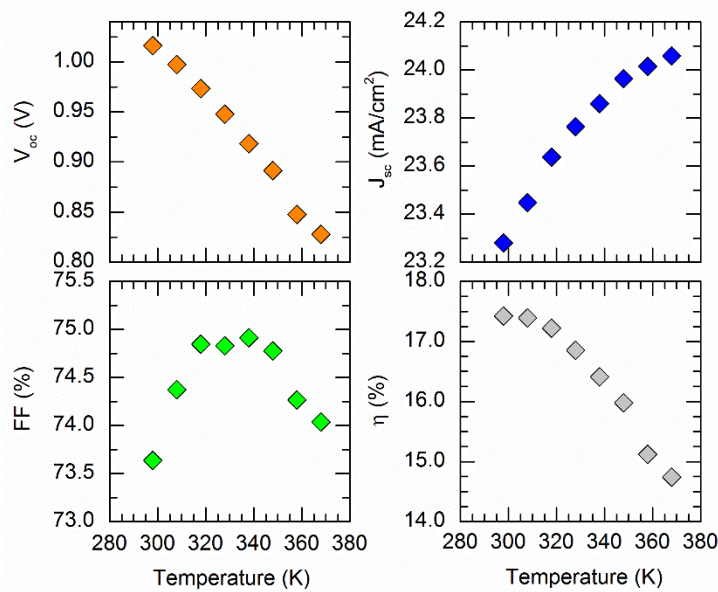
Fig. 48 Extracted device parameters for a CdTe double-heterostructure solar cell versus device temperature. Temperature is controlled using a hotplate and measured using an attached thermocouple.

.

In addition, it's clear from the J-V curves themselves shown in Fig. 49, that for the $Mg_{0.13}Cd_{0.87}Te$ devices, an actual shift in the maximum-power-point voltage is visible at higher temperatures while the maximum power point for the CdTe devices shifts to lower voltages for all temperature increases. Nevertheless, a change in the slope of the J-V curve at open-circuit is still visible for CdTe devices indicating a reduction in the series resistance. The slope of the curves begins to stabilize as the temperature increases even further and the series resistance becomes constant with temperature. The existence of wider and higher barriers in the $Mg_{0.13}Cd_{0.87}Te$ samples along with the undoped absorber would of course lead to a larger benefit to FF with increasing temperature as compared to the CdTe devices. The FF of both devices approach the same 75% value but the $Mg_{0.13}Cd_{0.87}Te$ samples require additional thermal energy to reach this point.
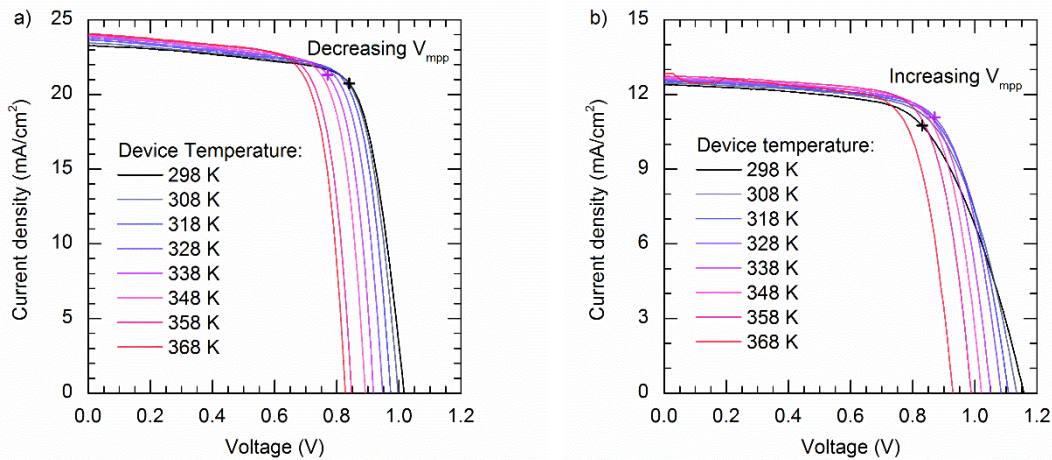
Fig. 49 Light J-V curves for a a) CdTe solar cell and a b) $Mg_{0.13}Cd_{0.87}Te$ solar cell versus device temperature. The maximum power point has been marked to indicate how this point shifts with a change in temperature.

The change in series resistance is even more evident in the J-V characteristic without illumination. At large forward bias, the effect of series resistance dominates and differences can easily be distinguished—with higher resistance values reducing the current density and causing roll over in the curve. Fig. 50 shows the dark J-V characteristics for both a CdTe solar cell (a) and a MgCdTe solar cell (b) measured at varying device temperatures. The roll over and consequent reduction in current density is improved greatly with the increase in temperature for a MgCdTe based device. While some improvement is seen with CdTe based devices, the change in series resistance is not nearly as dramatic. In both cases, the dark-current density J_0 will increase with temperature as expected, visualized by a shift left and shown in TABLE 10. The J_0 values reported are extracted from fitting the linear portion of the natural log of the dark J-V curve within the narrow voltage range as indicated in Fig. 51. Despite the changes, the dark current for the MgCdTe devices is several orders of magnitude larger than that of the CdTe device although they do begin to converge at higher temperatures. The dark I-V characteristic of the highest efficiency MgCdTe cell is shown in Fig. 51.
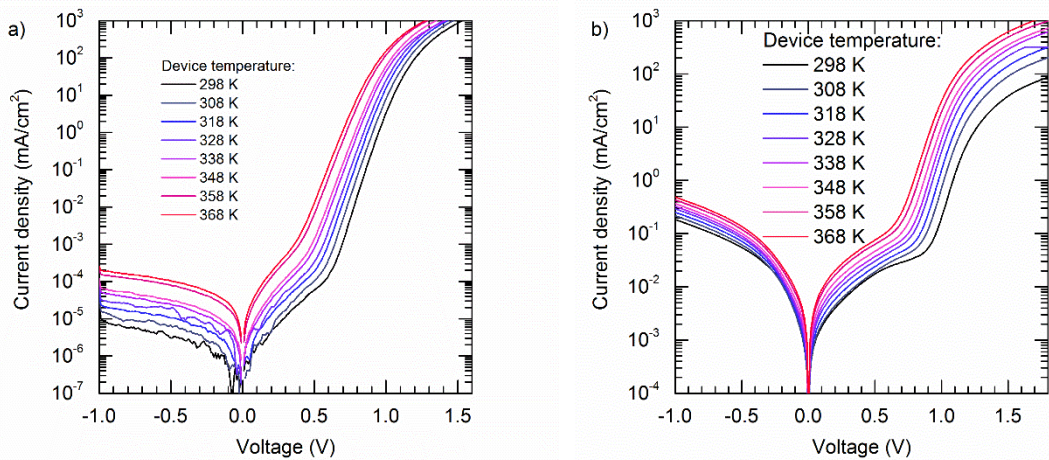
Fig. 50 Dark J-V characteristic measured at varying device temperature for a a) CdTe solar cell device and a b) $Mg_{0.13}Cd_{0.87}Te$ solar cell device.

TABLE 10
DARK CURRENT DENSITIES FOR CDTE AND MGCDTE SOLAR CELLS
FOR VARYING DEVICE TEMPERATURE

Device temperature (K)	J_0 (mA/cm^2)	
	CdTe	$Mg_{0.13}Cd_{0.87}Te$
298	4.9×10^{-12}	1.9×10^{-9}
308	6.4×10^{-11}	7.9×10^{-9}
318	2.4×10^{-10}	1.8×10^{-8}
328	6.6×10^{-10}	3.2×10^{-8}
338	3.2×10^{-9}	5.8×10^{-8}
348	7.3×10^{-9}	1.7×10^{-7}
358	5.9×10^{-8}	4.4×10^{-7}
368	1.4×10^{-7}	1.3×10^{-6}
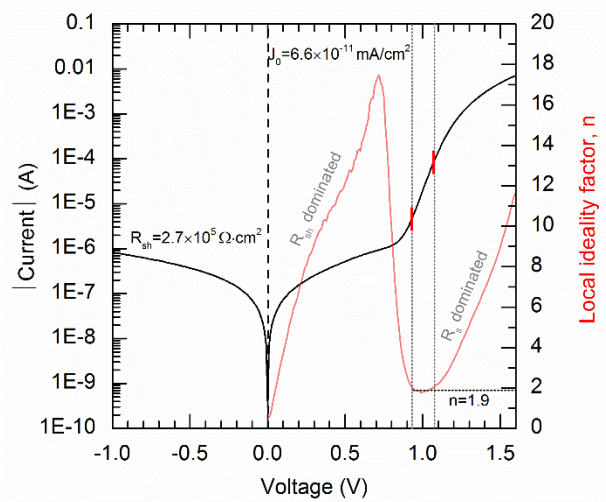
Fig. 51 Dark I-V curve (black) and ideality factor (red) for the $Mg_{0.13}Cd_{0.87}Te$ solar cell with the highest efficiency. Due to the large effects of the shunt and series resistances, the extraction of the dark-current density and ideality factor is limited to the small voltage range indicated.

This is indicative of an area for further improvement with respect to absorber passivation. Eliminating these barriers to current flow would result in a dramatic increase in FF and a return to the negative trend in FF with increasing temperature. However, this temperature dependence does provide some level of benefit at this stage as standard

operating temperatures of a device in the field typically range much hotter than the standard conditions used for measuring devices in the lab under AM1.5G. This means that although a maximum room temperature efficiency of 11.2% for $Mg_{0.13}Cd_{0.87}Te$ is reported, the efficiency at operating conditions may be higher; this is in stark contrast to other PV technologies in which the exact opposite holds true. If we apply the same level of FF and J_{sc} improvement, and V_{oc} reduction at higher temperatures to the hero device, it is reasonable to assume the efficiency can be 11.7% without any changes to the actual design.

5.1.2   Loss mechanisms contributing to lower J_{sc}

To analyze the photocurrent loss mechanisms, the reflectance and absorptance spectrum of each layer is calculated using wave-optics, as presented in Fig. 52. Several of the experimentally observed losses such as the large parasitic absorption in the a-Si:H contact layer and the ITO are clearly visible, along with smaller losses such as transmission loss. One deviation from prior discussion that becomes apparent when viewing the simulated response is the influence of parasitic absorption within the i-MgCdTe barrier layer. MgCdTe still has a high absorption coefficient and will absorb higher energy photons even within the relatively thin 15 nm barrier layer. Within the calculations, these photo-generated carriers are assumed to be lost to non-radiative recombination which can be visualized in the steep and immediate drop in EQE at the MgCdTe band edge (≈550 nm). However, this same dramatic drop is not present in the measured EQE curves for any of the CdTe solar cells; the EQE of the record device shown in Fig. 32 b) in Chapter 4 can be used as reference. This lack of distinct drop at the MgCdTe band edge and higher than expected EQE response at shorter wavelengths could indicate that not all carriers generated in this barrier layer are lost but may be collected. A very strong electric field exists within

79

the barrier layer and can generally sweep these carriers to their respective contacts very quickly. The voltage dependent measurements discussed below help substantiate this claim.
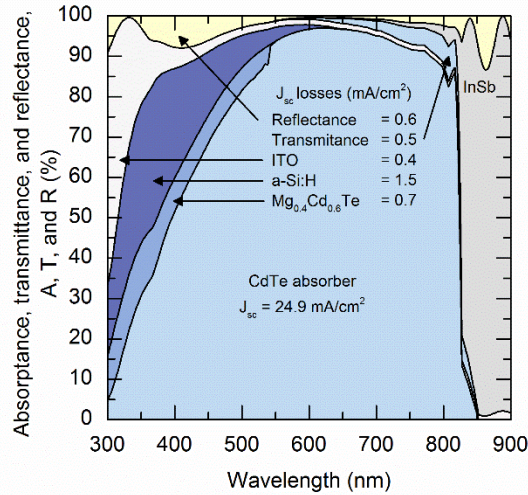
Fig. 52 Simulated absorptance, transmittance and reflectance spectra of CdTe/MgCdTe double-heterostructure solar cell.

The wavelength dependence of the ratio of EQE measurements at different voltage biases can be a helpful method in determining the location and mechanisms responsible for incomplete collection [63]. As can be seen in Fig. 53, there is a strong bias dependence at shorter wavelengths for the CdTe double-heterostructure solar cells. In the case of reverse bias, response at short wavelengths will increase while the opposite holds true for EQE measurements at forward bias. This is indicative of a stronger field dependence for carriers absorbed nearer to the upper surface of the absorber or even within the barrier layer itself. The relative wavelength independence of the EQE ratio for wavelengths greater than 500 nm would suggest that voltage dependent loss mechanisms are effecting all carriers equally. Several electrical loss mechanisms can contribute to this loss including interface recombination and barriers caused by the band offsets between the CdTe absorber and the

MgCdTe barrier/passivation layers. It is unlikely that the former is responsible as the IRV for these structures is remarkably low [6], [9], but rather, the energy barrier for holes at the upper barrier is responsible. The voltage dependence of the EQE ratio is also shown in Fig. 54 for three select wavelengths. There is a strong voltage dependence at all bias points for short wavelengths, whereas wavelengths above 500 nm show no relative decay until the device nears flat band.
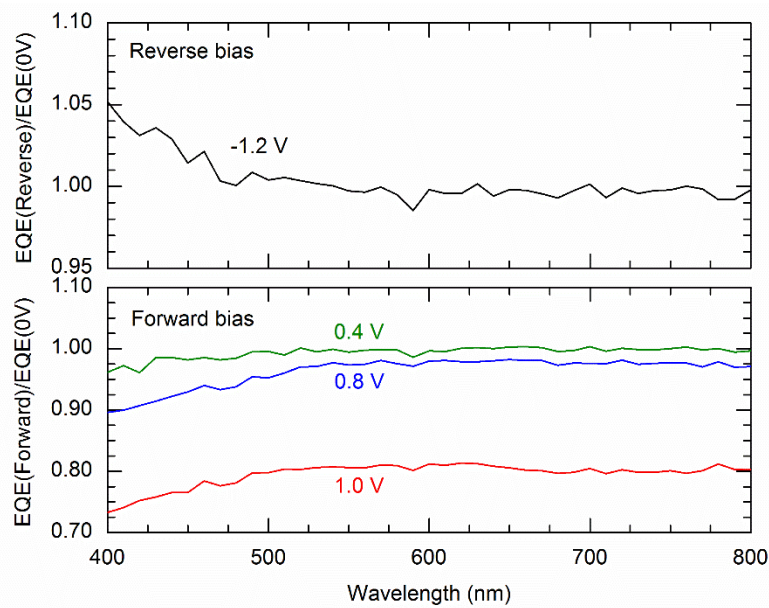
Fig. 53 QE ratios for a CdTe solar cell device at reverse (top) and forward (bottom) bias compared at 0 V bias.
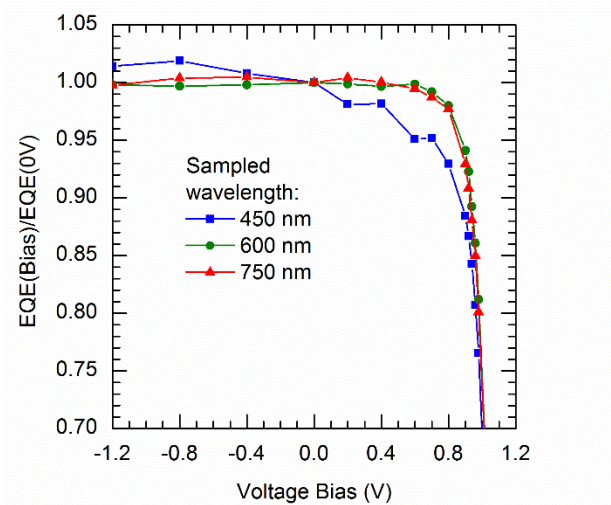
Fig. 54 Ratio of EQE at bias to EQE measured at 0 V for three different wavelengths: 450 nm, 600 nm, and 750 nm.

The test conditions under which these measurements are taken must be considered as the illumination intensity will differ greatly between standard EQE conditions and standard J-V test conditions. For standard J-V curve measurements, devices are illuminated with a white light of ~100 mW/cm^2 while the EQE setup utilized here has a much lower beam intensity. For this reason, it is sometimes recommended to use a constant wattage white bias light in addition to the low frequency monochromatic probing light to ensure the carrier density within the device remains the same between measurements—especially when making voltage dependent comparisons. This was not done so in the majority of the EQE measurements discussed here primarily because no discernable difference was found between the EQE of the device measured with and without additional light bias. The EQE of the hero device was measured at NREL utilizing a white light bias equivalent to approximately 9 mA/cm^2, while the same device was measured at ASU with no light bias and presented the same output. In many devices the additional bias light is necessary to quench or saturate recombination centers, thereby increasing the spectral response over a

standard monochromatic condition with no background source [64]. For the very high quality CdTe absorbers with good quality interfaces and low IRV, this is not considered to be an issue and is also confirmed with TRPL measurements that exhibit no intensity dependence as seen in Fig. 55 a). This same reasoning however, may not apply to the MgCdTe absorber based devices as there is a significant excitation dependence seen in the TRPL results—viewed in Fig. 55 b). Further intensity and voltage dependent EQE measurements need to be examined to fully understand the spectral response of such devices.
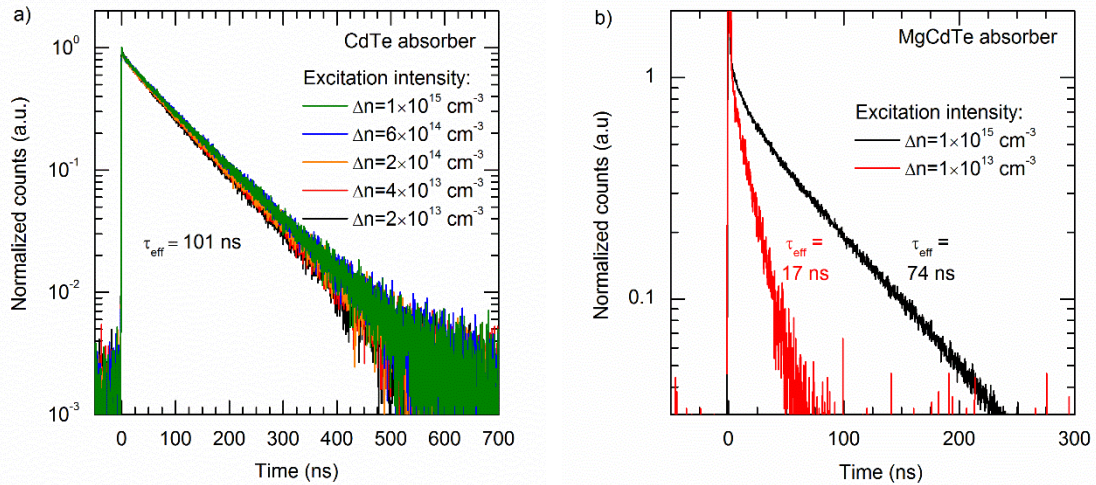
Fig. 55 Excitation dependent TRPL results for a) a CdTe/Mg$_{0.5}$Cd$_{0.5}$Te double heterostructure and b) a Mg$_{0.13}$Cd$_{0.87}$Te/Mg$_{0.5}$Cd$_{0.5}$Te double heterostructure. Unpublished TRPL measurements and fitting carried out by Dr. Xin-hao Zhao.

The photocurrent loss mechanisms for a MgCdTe absorber based device are also explored with the reflectance and absorptance spectrum of each layer calculated using wave-optics presented in Fig. 56. The absorptance of the Mg$_{0.13}$Cd$_{0.87}$Te absorber layer resembles the measured EQE closely, indicating that the carrier collection efficiency in the solar cell is close to unity just as is the case with the CdTe devices. This outcome is

expected as the minority carrier lifetime (and thus diffusion length) in $Mg_{0.13}Cd_{0.87}Te/Mg_{0.5}Cd_{0.5}Te$ DHs is measured to be very long. Integrating the absorptance of the CdTe absorber with the AM1.5G spectrum gives a J_{sc} of 15.3 mA/cm^2. The losses of photocurrent due to reflectance and parasitic absorption are also shown in Fig. 56. The J_{sc} can be further improved by employing double-layer antireflection coatings, wider-bandgap hole contact layers and a thicker $Mg_{0.13}Cd_{0.87}Te$ absorber; the large reduction in quantum efficiency near the band edge cannot be explained by a change in reflectance alone, but also incomplete absorption due to the only 500 nm absorber.
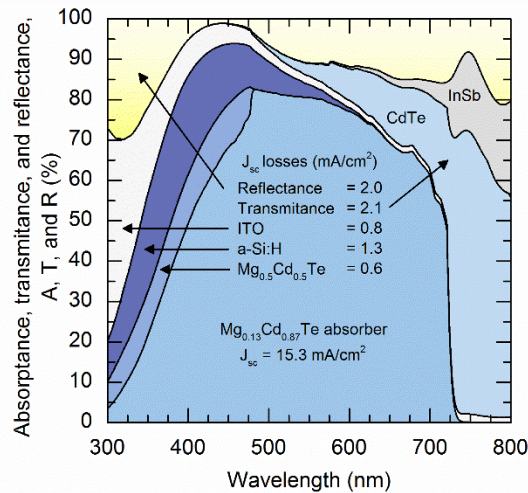
Fig. 56 Simulated absorptance, transmittance and reflectance spectra of $Mg_{0.13}Cd_{0.87}Te/Mg_{0.5}Cd_{0.5}Te$ double-heterostructure solar cell.

Up until this point, the hole contact has always been a material that can readily achieve relatively high hole densities and has a similar electron affinity to that of CdTe. However, n-type materials can provide the same functional band bending in the absorber when the electron affinity is on the order of 5.5 eV. Transition metal oxides (TMO) provide a group of materials that, while essentially n-type, have appropriately placed work functions which can support a large V_{bi}. The MoO_x system supports a wide range in both band gap and work

function as the oxygen content changes [65]. Silicon devices have employed this same design methodology using hole selective MoO_x contacts to great effect [66]. As with the silicon solar cells, CdTe absorber based devices share the same motivation for utilizing MoO_x as the hole-selective contact through band-to-band tunneling—the larger bandgap is beneficial in minimizing the parasitic absorption that has such a large effect on the current density of a-Si:H based contacts and perhaps may play role in the future in increasing the J_{sc} in these devices.

5.2 Envisioned design changes

5.2.1   Jsc improvement through bandgap narrowing

Fig. 57 shows a comparison of the EQE of the monocrystalline CdTe solar cell from Fig. 32 with the EQE of First Solar's record-efficiency polycrystalline cell. The majority of the difference in performance at wavelengths below 700 nm can be attributed to parasitic absorption—visible in Fig. 57 as the shaded region above the EQE—which, as previously discussed, is primarily in the hole contact layer. In addition, higher reflectance at the bounds of the visible spectrum contributes to the lower J_{sc} to some extent, due to the nature of the anti-reflection coating design technique in which optimizing the location of the minimum was the primary goal. However, a significant contributor to the higher J_{sc}, and thus the higher efficiency, of First Solar's polycrystalline cells is their lower bandgap. The approximately 1.41 eV bandgap found in polycrystalline devices is due to the incorporation of selenium. Because CdSeTe ternary alloys have a strong bowing parameter, the bandgap is reduced as selenium is introduced into the CdTe absorber [67]. This difference in bandgap alone is responsible for over 3 mA/cm^2 of potential photocurrent generation, amounting to a nearly 13% increase over the present monocrystalline J_{sc}.
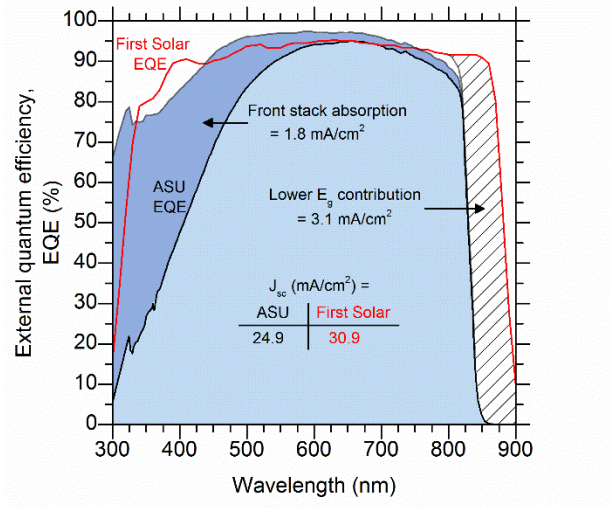
Fig. 57 EQE comparison between the monocrystalline CdTe solar cell from Fig. 32 and the record-efficiency polycrystalline solar cell developed by First Solar in 2015 (data for the new record cell is not yet available) [68].

For polycrystalline devices, lowering the bandgap in this manner may be possible while maintaining a relatively constant W_{oc}, but adding selenium to monocrystalline devices is expected to have an outsized detriment on V_{oc} because the change in lattice constant may result in a considerable reduction in epitaxial material quality. Moving towards 30 mA/cm^2 actually extracted from the device will necessarily require that the maximum attainable current be larger than this value depending upon the average collection efficiency of the device. Fig. 58 shows the maximum attainable J_{sc} versus the bandgap energy of the absorber as determined by the integration of the AM1.5G solar spectrum below each energy. As the average collection efficiency decreases—whether through losses due to reflectance, parasitic absorption, recombination, etc.—the bandgap must be lowered even further to extract the desired 30 mA/cm^2.
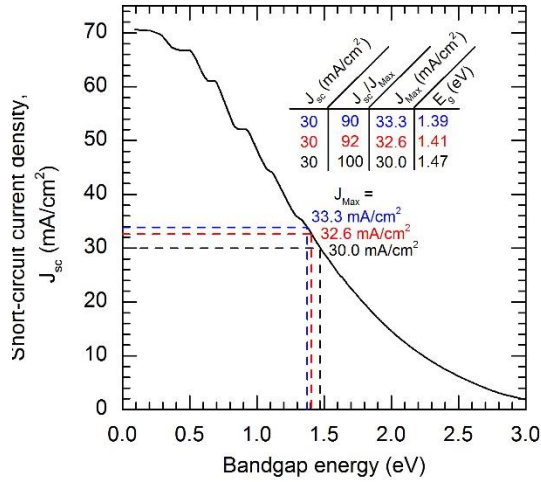
Fig. 58 Maximum attainable short-circuit current density for a given absorber bandgap energy. The displayed relationships were chosen to display the absorber bandgap necessary to achieve a J_{sc} of 30 mA/cm2 given different collection efficiencies.

Several options exist for determining the relationship between the tellurium/selenium composition within the CdSe$_{1-x}$Te$_x$ ternary and the bandgap energy and lattice constant. The data presented in Fig. 59 a) and b) utilizes the simple Vegard's law presented below:

$$E_g(CdSe_{1-x}Te_x) = x * E_g(CdTe) + (1-x) * E_g(CdSe) - b * x * (1-x) \quad (11)$$

where E_g(CdTe) is 1.51 eV, E_g(CdSe) is 1.66 eV, and b is 0.83 eV [69]. This bowing parameter represents the average of several experimentally determined values, but additional quadratic and linear fits to experimental data result in even larger bowing parameters of up to 0.996 eV [67]. Because this range is so large, predicting the selenium content necessary to reach the desired bandgap is difficult to accomplish. The calculations that follow dictate the upper bound in terms of selenium incorporation based on the lower bowing parameter of 0.83 eV.
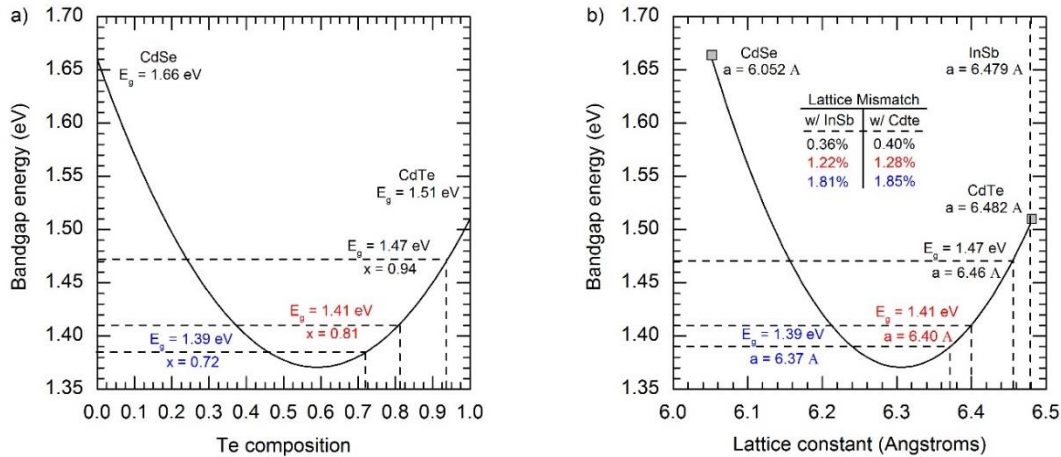
Fig. 59 CdSe$_{1-x}$Te$_x$ bandgap energy versus a) tellurium composition and b) ternary lattice constant. The tellurium compositions necessary to achieve the bandgap energies shown in Fig. 58 are indicated in a) while the lattice constants of the ternaries with those compositions are indicated in b).

To reach the same approximate bandgap as is presumed to be used with the record holding devices developed by First Solar (1.41 eV), it is necessary to incorporate roughly 19% selenium as seen in Fig. 59 a). Unfortunately, moving this far from pure CdTe pushes the lattice constant down to 6.40 Å, resulting in a large mismatch with the InSb substrate as seen in Fig. 59 b). While the addition of selenium clearly will result in a reduction in V$_{oc}$ as the bandgap decreases, the corresponding reduction in material quality due to the large lattice mismatch may also dramatically increase the W$_{oc}$. If this is the case, any potential benefits in current generation would be negated as there will be an outsized detriment on the V$_{oc}$.

Grading of the absorber bandgap is a potential solution to this problem in that it can reduce strain on the overall structure. Bandgap engineering has been considered within the thin-film field with limited success, specifically with CIGS devices [70]. However, the reasons for grading the bandgap in these devices differ greatly. Developing built-in electric

fields through increasing the bandgap is done to keep minority carriers away from potential recombination centers at the interfaces between the absorber and the contacts. In addition, larger bandgaps are desired within the quasi-neutral region to lower the recombination probability. Neither of these issues are present within the monocrystalline double-heterostructures discussed in this thesis. Nevertheless, grading may still prove beneficial for controlling material quality throughout the growth. There are two drawbacks however: 1) the smaller bandgap CdSeTe will only make up a portion of the absorber and therefore absorption of photons below 1.51 eV will be comparatively low; and 2) without fully understanding the valence and conduction band offsets between $CdSe_{1-x}Te_x$ and CdTe, it's possible that there will be a built-in field for both electrons and hole at the back contact. A complete understanding of all of these trade-offs within a monocrystalline system is not yet know.

5.2.2 Inverted device design

Improving current generation for these devices can also be achieved without necessarily changing the contact materials used, or resorting to bandgap tuning in the absorber. The process flow shown in Fig. 60 describes a method in which the solar cell structures currently under development can be utilized in an inverted design. By flipping the structure in this manner, the a-Si:H hole-contact layer—which is responsible for the majority of the parasitic absorption loss—is placed at the backend of the device. In such a design, nearly all of the higher energy photons incident on the device will be absorbed within the monocrystalline layers prior to reaching the backside of the device. However, an electron contact outside of the double heterostructure may still be necessary; in which case photons absorbed in this layer will also be lost to non-radiative recombination.

89

Notwithstanding, this solution remains a feasible option as the CdTe contact can be made thinner than the opposing hole contact without resulting in a depletion of majority carriers. As discussed in Chapter 3, the a-Si:H contact layer will deplete when paired with ITO and the thickness decreases below 8 nm. This won't be a problem with an electron contact and thus the CdTe contact layer can be made even thinner so as to reduce parasitic absorption.

In addition to the changes in layer location, the inversion and subsequent substrate removal allows for the use of a mirror at the backside of the device—effectively doubling the optical path length of the device. The thickness of the absorber can thus be slightly reduced without experiencing any transmission loss; either through transmission to a substrate, or through emission back out the front surface of the device. Consequently, not only should this design lead to an increase in J_{sc}, but the potential exists for an increase in V_{oc} as well. For radiative recombination dominated devices, the internal optics of the structure play a major role in determining the carrier lifetime within the absorber due to the effects of photon recycling [39], [71]. The CdTe/MgCdTe double heterostructures have been found to be radiatively limited and thus minority carrier lifetimes would benefit greatly from the presence of a mirror at the backside as opposed to an absorbing substrate; this may not always be the case as doping levels in the absorber are increased.

The early stages of the process itself are very similar to those described for all prior solar cell devices discussed in this thesis. The double heterostructure is grown by MBE up to the nominally intrinsic MgCdTe passivation layer shown in Fig. 60 a) at which point the hole-contact stack (a-Si:H/ITO/Ag) is deposited. Contrasted with the substrate based design, ITO mesas are not defined at this point but rather, all three layers are deposited across the entire surface forming the backside mirror shown in b). The device is then

flipped and bonded to a gold coated silicon carrier wafer, providing both support and backside contact. The substrate is then removed either through: 1) a combination of chemical mechanical polishing (CMP) and wet etching, or 2) a liftoff process using a sacrificial etching layer; MgTe has been shown to be a highly selective etching layer with submersion in water alone. TCO and metal pads can once again be used to provide current spreading and contacts.
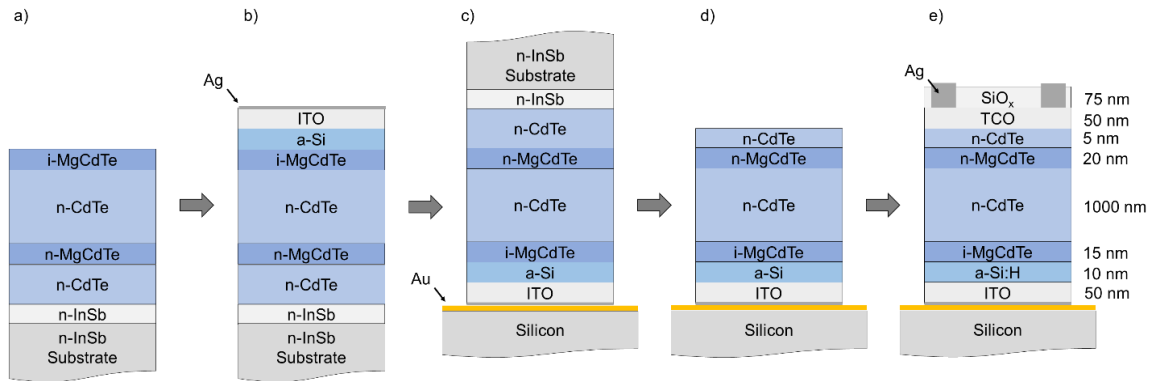
Fig. 60 Process flow describing potential development of an inverted solar cell device based on a CdTe double heterostructure.

The wave-optics simulation of this type of structure shown in Fig. 61 demonstrates the benefits of this design with respect to the readily achievable J_{sc}. The most clearly visible change is the lack of transmission loss mechanisms. At wavelengths between 650- and 850-nm, outside of reflectance losses, nearly all incident light is absorbed and collected. Of similar import, and the driving reason behind this design choice, is the movement of the hole contact to the back end of the device and the associated change in parasitic absorption. Even with a 5 nm CdTe electron contact still utilized at the top-side of the device, absorption within the layers outside of the double heterostructure has been reduced to nearly only 1 mA/cm^2. This brings the total weighted absorption within the CdTe absorber to a current density equivalent of 25.1 mA/cm^2 and when the MgCdTe passivation layer is

91

included—which has been shown to also have a high collection probability as well—this value increases to 27 mA/cm^2.
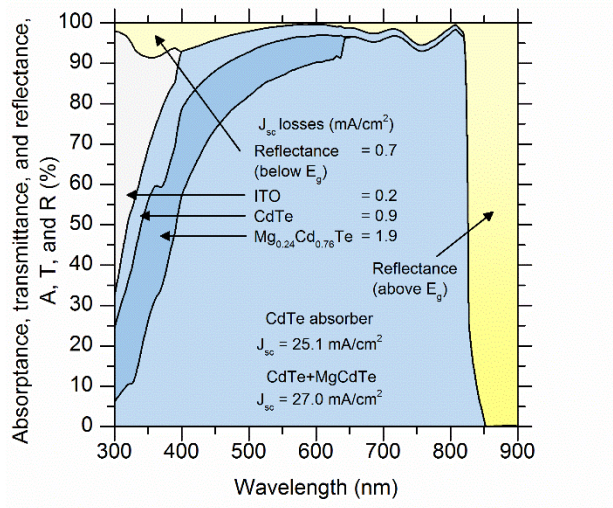
Fig. 61 Calculated absorptance, transmittance and reflectance spectra of the proposed solar cell structure shown in Fig. 60.

The thickness of the electron contact can be tuned to reduce the level of absorptance within this layer without resulting in the depletion of the contact and a reduction in the V_{bi} of the device. At 8 nm thick, as is the case with a-Si:H contact used in the hero device, approximately 1.8 mA/cm^2 in potential current is absorbed and lost within the CdTe contact. As the thickness of the contact is further reduced, the total current loss can even be negated as is the case if you eliminate the need for the layer altogether; the spectral absorptance for a series of thicknesses and their corresponding current losses are shown in Fig. 62.
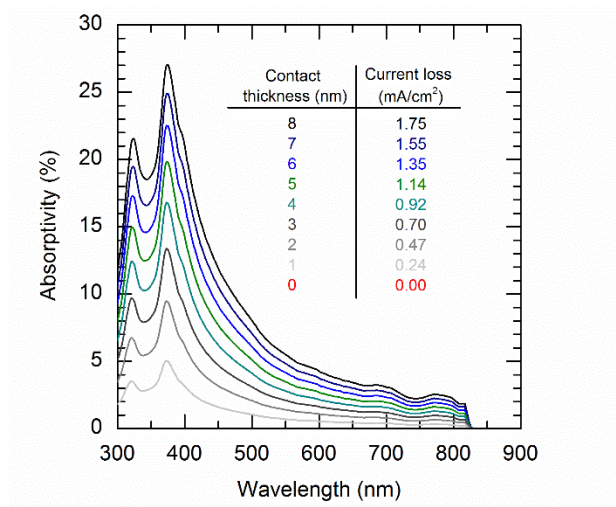
Fig. 62 Spectral absorptance within the CdTe contact layer for a series of thicknesses ranging from 0- to 8-nm. The associated current losses (mA/cm^2) within these layers are reported in the inset table.

CHAPTER 6

CONCLUSION

Monocrystalline CdTe double-heterostructure solar cells have shown great promise with respect to addressing the problems of low V_{oc} previously exhibited in CdTe solar cells. With the passing of the 1 V benchmark, rapid progress has been made in driving the efficiency in monocrystalline CdTe devices ever closer to the record set by polycrystalline thin-films. CdTe solar cell devices utilizing an a-Si:H hole contact provide the highest performance, with a total-area efficiency of 18.52% and an unshaded area efficiency of 20.3% measured at ASU and an NREL certified total-area efficiency 17.1%. The large discrepancy between the total-area efficiency and the unshaded area efficiency leaves plenty of room for further improvement within the realm of a-Si:H contacts and the potential for surpassing 22% is still possible through a further reduction in the series resistance and thus an improvement in FF. Wider bandgap $Mg_{0.13}Cd_{0.87}Te$ absorbers using the same a-Si:H contacts have demonstrated active-area efficiencies of up to 11.2% and a V_{oc} of 1.176 V. Fitting of the J-V curves along with extraction of a pseudo-FF from J_{sc}-V_{oc} measurements indicate that elimination of the series resistance within the devices can push the FF upwards of 80%. However, moving to wider bandgap solutions for the hole contact sets the maximum achievable efficiency even higher. This very approach was taken with ZnTe.

The V_{oc} of the solar cell devices with a ZnTe:Cu and ZnTe:As hole contact are 819 mV and 867 mV, respectively. Yet, the use of ZnTe as the top, hole-contact layer improves the EQE at wavelengths below 600 nm, thereby dramatically increasing the J_{sc} of such devices compared to devices using an a-Si:H hole contact. The resulting maximum efficiency of

14.1% was demonstrated with an arsenic-doped ZnTe hole contact grown by MOCVD. For this material to be a viable option, finding a ZnTe material that results in a V_{oc} beyond 1 V is imperative. With copper doping proving to be difficult to achieve without dramatic impact on the absorber quality, utilizing other dopant sources such as nitrogen or selenium may provide the necessary built-in voltage within the CdTe absorber while still allowing high voltages to be extracted at the electrodes.

While ZnTe and a-Si:H have shown to be sufficient contacts, other potential options exist that may provide for cheaper deposition techniques or lower levels of parasitic absorption. CuZnS is a transparent, heavily p-type material that can be deposited in a number of ways including inexpensive chemical bath deposition. Preliminary measurements on CdTe solar cells using CuZnS as a hole-contact layer have been measured with a V_{oc} of up to 980 mV—indicating that the copper within the contact may be immobile and does not necessarily degrade the quality of the CdTe absorber.

The double-heterostructure design grown on InSb substrates presents an excellent platform for high efficiency solar cells. Continued characterization and modification can lead to even further revelations about how to optimize CdTe based solar cell—monocrystalline or otherwise. Developing these designs and methods and transferring the technology to polycrystalline processes may help to improve the already impressive performance. This includes both the binary CdTe system as well as the potential development of the wider bandgap ternary system $Mg_xCd_{1-x}Te$ for use within tandem technologies.

REFERENCES

[1] M. Woodhouse, R. Jones-Albertus, D. Feldman, R. Fu, K. Horowitz, D. Chung, D. Jordan, and S. Kurtz, "On the Path to SunShot : The Role of Advancements in Solar Photovoltaic Efficiency , Reliability , and Costs," no. 2016, p. 44, 2016.

[2] W. Shockley and H. J. Queisser, "Detailed Balance Limit of Efficiency of p-n Junction Solar Cells," *J. Appl. Phys.*, vol. 32, no. 3, p. 510, 1961.

[3] M. A. Green, K. Emery, Y. Hishikawa, W. Warta, and E. D. Dunlop, "Solar cell efficiency tables (version 48)," *Prog. Photovolt Res. Appl.*, vol. 24, pp. 905–913, 2016.

[4] S. Adachi, *Optical Constants of Crystalline and Amorphous Semiconductors: Numerical Data and Graphical Information*. New York: Springer US, 1999.

[5] T. Nakazawa, K. Takamizawa, and K. Ito, "High efficiency indium oxide/cadmium telluride solar cells," *Appl. Phys. Lett.*, vol. 50, no. 5, p. 279, 1987.

[6] Y. Zhao, M. Boccard, S. Liu, J. Becker, X.-H. Zhao, C. M. Campbell, E. Suarez, M. B. Lassise, Z. Holman, and Y.-H. Zhang, "Monocrystalline CdTe solar cells with open-circuit voltage over 1 V and efficiency of 17%," *Nat. Energy*, vol. 1, no. May, p. 16067, 2016.

[7] J. M. Burst, J. N. Duenow, D. S. Albin, E. Colegrove, M. O. Reese, J. A. Aguiar, C.-S. Jiang, M. K. Patel, M. M. Al-Jassim, D. Kuciauskas, S. Swain, T. Ablekim, K. G. Lynn, and W. K. Metzger, "CdTe solar cells with open-circuit voltage greater than 1 V," *Nat. Energy*, vol. 1, p. 16015, 2016.

[8] M. Gloeckler, I. Sankin, and Z. Zhao, "CdTe Solar Cells at the Threshold to 20% Efficiency," *IEEE J. Photovoltaics*, vol. 3, no. 4, pp. 1389–1393, 2013.

[9] X. Zhao, S. Liu, C. M. Campbell, Y. Zhao, M. B. Lassise, and Y. Zhang, "Ultralow Interface Recombination Velocity (~1 cm/s) at CdTe/Mg$_x$Cd$_{1-x}$Te Heterointerface," *IEEE J. Photovoltaics*, vol. 7, 2017.

[10] X.-H. Zhao, S. Liu, Y. Zhao, C. M. Campbell, M. B. Lassise, Y.-S. Kuo, and Y.-H. Zhang, "Electrical and Optical Properties of n-Type Indium-Doped CdTe/Mg$_{0.46}$Cd$_{0.54}$Te Double Heterostructures," *IEEE J. Photovoltaics*, vol. 6, no. 2, pp. 552–556, 2016.

[11] J. J. Becker, M. Boccard, C. M. Campbell, Y. Zhao, M. Lassise, Z. C. Holman, and Y.-H. Zhang, "Loss analysis of monocrystalline CdTe solar cell with 20% active-area efficiency," *IEEE J. Photovoltaics*, 2017.

[12] J. J. Becker, C. M. Campbell, Y. Zhao, M. Boccard, D. Mohanty, M. Lassise, E. Suarez, I. Bhat, Z. C. Holman, and Y. Zhang, "Monocrystalline CdTe/MgCdTe double-heterostructure solar cells with ZnTe hole contacts," *IEEE J. Photovoltaics*, 2016.

[13] M. A. Green, "Commercial progress and challenges for photovoltaics," *Nat. Energy*, vol. 1, no. 15015, 2016.

[14] S. R. Kurtz, P. Faine, and J. M. Olson, "Modeling of two-junction, series-connected tandem solar cells using top-cell thickness as an adjustable parameter," *J. Appl. Phys.*, vol. 68, no. 4, pp. 1890–1895, 1990.

[15] S. Seyedmohammadi, M. J. DiNezza, S. Liu, P. King, E. G. LeBlanc, X. H. Zhao, C. Campbell, T. H. Myers, Y. H. Zhang, and R. J. Malik, "Molecular beam epitaxial re-growth of CdTe, CdTe/CdMgTe and CdTe/CdZnTe double heterostructures on CdTe/InSb(1 0 0) substrates with As cap," *J. Cryst. Growth*, vol. 425, pp. 181–185, 2015.

[16] Z.-Y. He, C. M. Campbell, M. B. Lassise, Z.-Y. Lin, J. J. Becker, Y. Zhao, M. Boccard, Z. Holman, and Y.-H. Zhang, "CdTe nBn photodetectors with ZnTe barrier layer grown on InSb substrates," *Appl. Phys. Lett.*, vol. 109, no. 12, p. 121112, 2016.

[17] K. J. MacKey, P. M. G. Allen, W. G. Herrenden-Harker, R. H. Williams, C. R. Whitehouse, and G. M. Williams, "Chemical and electronic structure of InSb-CdTe interfaces," *Appl. Phys. Lett.*, vol. 49, no. 6, pp. 354–356, 1986.

[18] B. Kuhn-Heinrich, W. Ossau, H. Heinke, F. Fischer, T. Litz, A. Waag, and G. Landwehr, "Optical investigation of confinement and strain effects in CdTe/(CdMg)Te quantum wells," *Appl. Phys. Lett.*, vol. 63, no. 21, pp. 2932–2934, 1993.

[19] Z. I. Alferov, "Nobel lecture: The double heterostructure concept and its applications in physics, electronics, and technology," *Rev. Mod. Phys.*, vol. 73, no. 3, pp. 767–782, 2001.

[20] H. Kroemer, "The Double-Heterostructure Concept: How It Got Started," *Proc IEEE*, vol. 101, no. 10, pp. 1–5, 2013.

[21] J.-H. Yang, W.-J. Yin, J.-S. Park, J. Burst, W. K. Metzger, T. Gessert, T. Barnes, and S.-H. Wei, "Enhanced p-type dopability of P and As in CdTe using non-equilibrium thermal processing," *J. Appl. Phys.*, vol. 118, no. 2, p. 25102, 2015.

[22] S. Abdi-Ben Nasrallah, S. Mnasri, N. Sfina, N. Bouarissa, and M. Said, "Calculation of band offsets in $Cd_{1-x}X_xTe$ alloys, X = Zn, Mg, Hg and Mn and magnetic effects in CdMnTe," *J. Alloys Compd.*, vol. 509, no. 29, pp. 7677–7683, 2011.

[23] C. A. Wolden, A. Abbas, J. Li, D. R. Diercks, D. M. Meysing, T. R. Ohno, J. D. Beach, T. M. Barnes, and J. M. Walls, "The roles of ZnTe buffer layers on CdTe solar cell performance," *Sol. Energy Mater. Sol. Cells*, vol. 147, pp. 203–210, 2016.

[24] T. Wojtowicz, M. Kutrowski, M. Surma, K. Kopalko, G. Karczewski, J. Kossut, M. Godlewski, P. Kossacki, and N. The Khoi, "Parabolic quantum wells of diluted magnetic semiconductor $Cd_{1-x}Mn_xTe$," *Appl. Phys. Lett.*, vol. 68, no. 23, pp. 3326–3328, 1996.

[25] J. Siviniant, F. V Kyrychenko, Y. G. Semenov, D. Coquillat, D. Scalbert, and J. P. Lascaray, "Magneto-optical determination of the valence-band offset in a CdTe/Cd$_{1-x}$Mn$_x$Te heterostructure," *Phys. Rev. B - Condens. Matter Mater. Phys.*, vol. 59, no. 15, pp. 10276–10282, 1999.

[26] B. Kuhn-Heinrich, W. Ossau, T. Litz, a. Waag, and G. Landwehr, "Determination of the band offset in semimagnetic CdTe/Cd$_{1-x}$Mn$_x$Te quantum wells: A comparison of two methods," *J. Appl. Phys.*, vol. 75, no. 12, p. 8046, 1994.

[27] J. W. Matthews and A. E. Blakeslee, "Defects in epitaxial multilayers: I. Misfit dislocations," *J. Cryst. Growth*, vol. 27, pp. 118–125, 1974.

[28] S. Adachi, *Handbook on physical properties of semiconductors*. Boston: Dordrecht: Kluwer Academic, 2004.

[29] E. Janik, E. Dynowska, J. Bąk-Misiuk, M. Leszczyński, W. Szuszkiewicz, T. Wojtowicz, G. Karczewski, A. K. Zakrzewski, and J. Kossut, "Structural properties of cubic MnTe layers grown by MBE," *Thin Solid Films*, vol. 267, no. 1–2, pp. 74–78, 1995.

[30] F. Kany, J. M. Hartmann, H. UlmerTuffigo, and H. Mariette, "Comparison between atomic layer epitaxy grown and molecular beam epitaxy grown CdTe/MnTe superlattices: a structural and optical study," *Superlattices Microstruct.*, vol. 23, no. 6, pp. 1359–1366, 1998.

[31] P. Maheswaranathan, R. J. Sladek, and U. Debska, "Elastic constants and their pressure dependencies in Cd$_{1-x}$Mn$_x$Te with 0<x<0.52 and in Cd$_{0.52}$Zn$_{0.48}$Te," *Phys. Rev. B*, vol. 31, no. 8, pp. 5212–5216, 1985.

[32] C. M. Campbell, Y. Zhao, E. Suarez, M. Boccard, X. Zhao, Z. He, P. T. Webster, M. B. Lassise, S. Johnson, Z. Holman, and Y. Zhang, "1.7 eV MgCdTe double-heterostructure solar cells for tandem device applications," in *the proceedings of the 43rd IEEE PVSC*, 2016, pp. 3–6.

[33] S. Liul, X. Zhao, Y. Zhaol, C. Campbelll, M. Lassisel, and E. Suarezl, "Structural and optical properties of Mg$_x$Cd$_{1-x}$Te alloys grown on InSb (100) substrates using molecular beam epitaxy," in *the proceedings of the 42nd IEEE PVSC*, no. 100, pp. 1–3, 2015.

[34] T. A. Gessert, W. K. Metzger, P. Dippo, S. E. Asher, R. G. Dhere, and M. R. Young, "Dependence of carrier lifetime on Cu-contacting temperature and ZnTe:Cu thickness in CdS/CdTe thin film solar cells," *Thin Solid Films*, vol. 517, no. 7, pp. 2370–2373, 2009.

[35] S. H. Demtsu, D. S. Albin, J. R. Sites, W. K. Metzger, and A. Duda, "Cu-related recombination in CdS/CdTe solar cells," *Thin Solid Films*, vol. 516, no. 8, pp. 2251–2254, 2008.

[36] K. Masuko, M. Shigematsu, T. Hashiguchi, D. Fujishima, M. Kai, N. Yoshimura, T. Yamaguchi, Y. Ichihashi, T. Mishima, N. Matsubara, T. Yamanishi, T. Takahama, M. Taguchi, E. Maruyama, and S. Okamoto, "Achievement of More Than 25% Conversion Efficiency With Crystalline Silicon Heterojunction Solar Cell," *IEEE J. Photovoltaics*, vol. 4, no. 6, pp. 1433–1435, 2014.

[37] O. D. Miller, E. Yablonovitch, and S. R. Kurtz, "Strong Internal and External Luminescence as Solar Cells Approach the Shockley-Queisser Limit," *IEEE J. Photovoltaics*, vol. 2, no. 3, pp. 1–27, 2012.

[38] R. T. Ross, "Some Thermodynamics of Photochemical Systems," *J. Chem. Phys.*, vol. 46, no. 12, pp. 4590–4593, 1967.

[39] M. A. Steiner, J. F. Geisz, I. García, D. J. Friedman, A. Duda, and S. R. Kurtz, "Optical enhancement of the open-circuit voltage in high quality GaAs solar cells," *J. Appl. Phys.*, vol. 113, no. 12, p. 123109, 2013.

[40] F. Fischer, A. Waag, G. Bilger, T. Litz, S. Scholl, M. Schmitt, and G. Landwehr, "Molecular beam epitaxy of iodine-doped CdTe and (CdMg)Te," *J. Cryst. Growth*, vol. 141, no. 1–2, pp. 93–97, 1994.

[41] N. Strevel, L. Trippel, C. Kotarba, and I. Khan, "Improvements in CdTe module reliability and long-term degradation through advances in construction and device innovation," *Photovoltaics Int.*, pp. 1–8, 2013.

[42] Y. Kuo, J. Becker, S. Liu, Y. Zhao, X. Zhao, P. Su, I. Bhat, and Y. Zhang, "Monocrystalline ZnTe/CdTe/MgCdTe Double Heterostructure Solar Cells Grown on InSb Substrates," in *the proceedings of the 42nd IEEE PVSC*, 2015.

[43] Y. Zhao, X.-H. Zhao, and Y.-H. Zhang, "Radiative recombination dominated n-type monocrystalline CdTe/MgCdTe double-heterstructures," in *the proceedings of the 43rd IEEE PVSC*, 2016, no. 1, pp. 0545–0548.

[44] M. Bivour, S. Schröer, and M. Hermle, "Numerical analysis of electrical TCO/a-Si:H(p) contact properties for silicon heterojunction solar cells," *Energy Procedia*, vol. 38, pp. 658–669, 2013.

[45] S. Y. Herasimenka, W. J. Dauksher, M. Boccard, and S. Bowden, "ITO/SiO$_x$:H stacks for silicon heterojunction solar cells," *Sol. Energy Mater. Sol. Cells*, no. 6, 2016.

[46] K. R. McIntosh and S. C. Baker-Finch, "OPAL 2: Rapid optical simulation of silicon solar cells," *Conf. Rec. IEEE Photovolt. Spec. Conf.*, pp. 265–271, 2012.

[47] S. De Wolf and M. Kondo, "Nature of doped a-Si:H/c-Si interface recombination," *J. Appl. Phys.*, vol. 105, no. 10, pp. 0–6, 2009.

[48] D. Zhang, I. A. Digdaya, R. Santbergen, R. A. C. M. M. Van Swaaij, P. Bronsveld, M. Zeman, J. A. M. Van Roosmalen, and A. W. Weeber, "Design and fabrication of a SiO$_x$/ITO double-layer anti-reflective coating for heterojunction silicon solar cells," *Sol. Energy Mater. Sol. Cells*, vol. 117, pp. 132–138, 2013.

[49] X.-H. Zhao, S. Liu, C. M. Campbell, Y. Zhao, M. B. Lassise, and Y.-H. Zhang, "Impact of thermionic emission and tunneling effect on the measurement of low interface recombination velocity (~1 cm/s) in CdTe/$Mg_x Cd_{1-x}$Te double heterostructures," in *the proceedings of the 43nd IEEE PVSC*, pp. 2302–2305, 2016.

[50] S. Liu, X.-H. Zhao, C. M. Campbell, M. Lassise, Y. Zhao, and Y. Zhang, "Carrier lifetimes and interface recombination velocities in CdTe/$Mg_x Cd_{1-x}$Te double heterostructures with different Mg compositions grown by molecular beam epitaxy," *Appl. Phys. Lett.*, vol. 41120, pp. 1–6, 2015.

[51] Y. Zhao, M. Boccard, J. Becker, X. Zhao, C. M. Campbell, M. B. Lassise, Z. Holman, and Y. Zhang, "High built-in potential and V_{oc} of monocrystalline CdTe/MgCdTe double-heterostructure solar cells with p-type a-Si:H hole-contacts," in *the proceedings of the 43rd IEEE PVSC*, vol. 1, pp. 3–5, 2016.

[52] I. Repins, L. Mansfield, A. Kanevce, S. A. Jensen, D. Kuciauskas, S. Glynn, T. Barnes, W. Metzger, J. Burst, C. Jiang, P. Dippo, S. Harvey, C. Perkins, B. Egaas, A. Zakutayev, J. Alsmeier, T. Lußky, R. G. Wilks, M. Bär, Y. Yan, S. Lany, P. Zawadzki, J. Park, S. Wei, N. Renewable, H. Berlin, E. Gmbh, and B. T. U. Cottbus-senftenberg, "Wild Band Edges : The Role of Bandgap Grading and Band-Edge Fluctuations in High-Efficiency Chalcogenide Devices," in *the proceedings of the IEEE PVSC*, pp. 0309–0314, 2016.

[53] C. Battaglia, S. M. De Nicolas, S. De Wolf, X. Yin, M. Zheng, C. Ballif, and A. Javey, "Silicon heterojunction solar cell with passivated hole selective MoO_x contact," *Appl. Phys. Lett.*, vol. 104, no. 11, pp. 2012–2017, 2014.

[54] J. Merten, J. M. Asensi, C. Voz, a. V. Shah, R. Platz, and J. Andreu, "Improved equivalent circuit and analytical model for amorphous\nsilicon solar cells and modules," *IEEE Trans. Electron Devices*, vol. 45, no. 2, pp. 423–429, 1998.

[55] U. Wurfel, A. Cuevas, and P. Wurfel, "Charge carrier separation in solar cells," *IEEE J. Photovoltaics*, vol. 5, no. 1, pp. 461–469, 2015.

[56] M. J. DiNezza, X.-H. Zhao, S. Liu, A. P. Kirk, and Y.-H. Zhang, "Growth, steady-state, and time-resolved photoluminescence study of CdTe/MgCdTe double heterostructures on InSb substrates using molecular beam epitaxy," *Appl. Phys. Lett.*, vol. 103, no. 19, p. 193901, 2013.

[57] X. Wang, C. Campbell, Y.-H. Zhang, and R. Nemanich, "Band alignment of hydrogen-plasma cleaned MBE CdTe on InSb (001)," in *Materials Research Society Spring Meeting*, 2015.

[58] Y. Hinuma, A. Grüneis, G. Kresse, and F. Oba, "Band alignment of semiconductors from density-functional theory and many-body perturbation theory," *Phys. Rev. B*, vol. 90, no. 15, p. 155405, 2014.

[59] A. G. Aberle, S. . R. Wenham, and M. a. Green, "A new method for accurate measurements of the lumped series resistance of solar cells," in *the proceedings of the 23rd IEEE Photovolt. Spec. Conf.*, pp. 133–139, 1993.

[60] D. Pysch, A. Mette, and S. W. Glunz, "A review and comparison of different methods to determine the series resistance of solar cells," *Sol. Energy Mater. Sol. Cells*, vol. 91, no. 18, pp. 1698–1706, 2007.

[61] K. C. Fong, K. R. McIntosh, and A. W. Blakers, "Accurate series resistance measurement of solar cells," *Prog. Photovolt Res. Appl.*, vol. 21, no. February 2013, pp. 490–499, 2013.

[62] P. Singh and N. M. Ravindra, "Temperature dependence of solar cell performance—an analysis," *Sol. Energy Mater. Sol. Cells*, vol. 101, pp. 36–45, 2012.

[63] S. S. Hegedus and W. N. Shafarman, "Thin-film solar cells: device measurements and analysis," *Prog. Photovoltaics Res. Appl.*, vol. 12, no. 23, pp. 155–176, 2004.

[64] V. L. Dalal and A. Rothwarf, "Comment on a simple measurement of absolute solar cell efficiency,'" *J. Appl. Phys.*, vol. 50, no. 4, pp. 2980–2981, 1979.

[65] I. Irfan, A. James Turinske, Z. Bao, and Y. Gao, "Work function recovery of air exposed molybdenum oxide thin films," *Appl. Phys. Lett.*, vol. 101, no. 9, 2012.

[66] J. Bullock, A. Cuevas, T. Allen, and C. Battaglia, "Molybdenum oxide MoO_x: A versatile hole contact for silicon solar cells," *Appl. Phys. Lett.*, vol. 105, no. 23, 2014.

[67] G. Brill, Y. Chen, P. M. Amirtharaj, W. Sarney, D. Chandler-Horowitz, and N. K. Dhar, "Molecular beam epitaxial growth and characterization of Cd-based II–VI wide-bandgap compounds on Si substrates," *J. Electron. Mater.*, vol. 34, no. 5, pp. 655–661, 2005.

[68] E. D. Green, Martin A.; Emery, Keith; Hishikawa, Yoshihiro; Warta, Wilhelm; Dunlop, "Solar Cell Efficiency Tables (Version 46)," *Prog. Photovoltaics Res. Appl.*, vol. 23, no. 1, pp. 805–812, 2015.

[69] I. Hernandez-Calderon, "Optical Properties and Electronic Structure of Wide Band Gap II-VI Semiconductors," in *II-VI Semiconductor Materials and their Applications*, M. C. Tamargo, Ed. New York: Taylor & Francis Inc., 2002, p. 145.

[70] O. Lundberg, M. Edoff, and L. Stolt, "The effect of Ga-grading in CIGS thin film solar cells," *Thin Solid Films*, vol. 480–481, pp. 520–525, 2005.

[71] M. A. Steiner, J. F. Geisz, I. Garcia, D. J. Friedman, A. Duda, W. J. Olavarria, M. Young, D. Kuciauskas, and S. R. Kurtz, "Effects of Internal Luminescence and Internal Optics on V_{oc} and J_{sc} of III--V Solar Cells," *IEEE J. Photovoltaics*, vol. 3, no. 4, pp. 1437–1442, 2013.

APPENDIX A

COMPLETE LIST OF MATERIAL PARAMETERS

TABLE 11
BINARY MATERIAL PARAMETERS

	InSb	CdTe	MgTe	ZnTe	MnTe
a (nm)	0.648	0.6481 [28]	0.6420 [28]	0.6104 [28]	0.6337 [29]
Epsilon	17.7	10.4 [28]	7.0 [28]	9.4 [28]	
E_g (eV)	0.174	1.51 [28]	3.46 [28]	2.27 [28]	3.2 [30]
X (eV)	4.59	4.28 [28]		3.5 [28]	3.266
N_c (cm^{-3})	3.94×10^{16}	8.6×10^{17}		1.12×10^{18}	
N_v (cm^{-3})	7.12×10^{18}	6.0×10^{18}		1.55×10^{19}	
n_i (cm^{-3})	1.84×10^{16}	4.97×10^{5}		1.5×10^{-1}	
c_{11} (10^{11} dyn/cm^2)	-	5.35 [28]	5.28 [28]	7.15 [28]	5.86 [17,18]
c_{12} (10^{11} dyn/cm^2)	-	3.69 [28]	3.66 [28]	4.08 [28]	3.28 [30]
v	-	0.408	0.409	0.363	0.359 [17,18]
τ_n (ns)		100	1	1	
τ_p (ns)		100	1	1	
μ_n (cm^2/Vs)		1050 [28]		7	
μ_p (cm^2/Vs)		104 [28]		1.5	

TABLE 12
COMMON TERNARY PARAMETERS

	Mg$_{0.24}$Cd$_{0.76}$Te	Mg$_{0.40}$Cd$_{0.60}$Te	Zn$_{0.77}$Cd$_{0.23}$Te	Mn$_{0.54}$Cd$_{0.46}$Te
a (nm)	0.6466	0.6455	0.6191	0.6407
f_m (%)	0.23	0.42	4.46	1.13
E_g (eV)	1.97	2.284	2.039	2.36
X (eV)	3.951	3.731	3.731	3.731
N_c (cm^{-3})*	7.18×10^{19}	3×10^{22}	-	-
N_v (cm^{-3})*	5×10^{20}	2×10^{23}	-	-

*Calculated using the intrinsic carrier concentration, N_c/N_v ratio, and bandgap of the ternary using the following equation

APPENDIX B

QUANTUM EFFICIENCY MEASUREMENT CONSIDERATIONS

External quantum efficiency (EQE) is a ratio of the carriers collected from a solar cell to the photons of a given energy incident on the surface; internal quantum efficiency (IQE) would be the ratio to the number of photons actually absorbed. Of course, this means that it can be plotted against either energy or wavelength. In most cases in which data is converted, a simple change of x-axis is of course not sufficient and we can see why when examining the blackbody radiation spectrum when calculated per unit wavelength or per unit energy. Throughout this appendix, we will see though that this is not the case with EQE.

Spectral Irradiance versus energy:

$$I_E = \frac{2E^3}{h^3 c^2 \left[e^{\left(\frac{E}{k_B T} \right)} - 1 \right]} \tag{1}$$

$$I_E \sim \frac{J}{m^2 \cdot s \cdot eV} \tag{2}$$

However, this gives the irradiance of the blackbody per unit solid angle, so we must determine what proportion of the radiation from the sun hits the surface of the earth. In addition, the intensity will scale with the area of the radiating body (dA) as is observed from the surface of the earth.

$$d\Omega dA = \frac{\pi R_s^2}{d^2} = \pi \sin(\Theta_{sun})^2 \approx 6.8 \times 10^{-5} \tag{3}$$

where d is the distance between the Earth and the Sun and R_s is the radius of the sun; alternatively, the angle between the center of the earth and the edge of the sun, Θ_{sun}, can be used. The 4π term associated with the surface area of a unit sphere has already been taken into account in equation (1) and has therefore been left out of equation (3).

Constant	Value	Units
Planck Constant (h)	4.135×10^{-15}	eV·s
Boltzmann Constant (k_B)	8.62×10^{-5}	eV/K
Speed of Light (c)	3.0×10^{8}	m/s

Spectral Irradiance versus wavelength:

The same process can be carried out to determine the irradiance with respect to wavelength instead of energy. Converting between energy and wavelength results in the following equation:

$$I_\lambda = \frac{2hc^2}{\lambda^5 \left[e^{\left(\frac{hc}{\lambda k_B T} \right)} - 1 \right]} \tag{4}$$

$$I_\lambda \sim \frac{J}{m^2 \cdot s \cdot nm} \tag{5}$$

$$d\Omega dA = \frac{\pi R_s^2}{d^2} = \pi \sin(\Theta_{sun})^2 \approx 6.8 \times 10^{-5} \tag{6}$$

Constant	Value	Units
Planck Constant (h)	6.624×10^{-34}	J·s
Boltzmann Constant (k_B)	1.38×10^{-23}	J/K
Speed of Light (c)	3.0×10^{8}	m/s

Final equations:

$$I_\lambda = \frac{(1.37 \times 10^{-4}) hc^2}{\lambda^5 \left[e^{\left(\frac{hc}{\lambda k_B T} \right)} - 1 \right]} d\lambda \tag{7}$$

$$I_E = \frac{(1.37 \times 10^{-4}) E^3}{h^3 c^2 \left[e^{\left(\frac{E}{k_B T} \right)} - 1 \right]} dE \tag{8}$$

Blackbody radiation vs. measured irradiance:

The blackbody spectrum at 6000K plotted with the measured spectral irradiance AM0, which is the intensity of light without atmospheric absorption, is shown in Fig. B-1; data provided by NREL. This temperature will be used for all future comparisons.
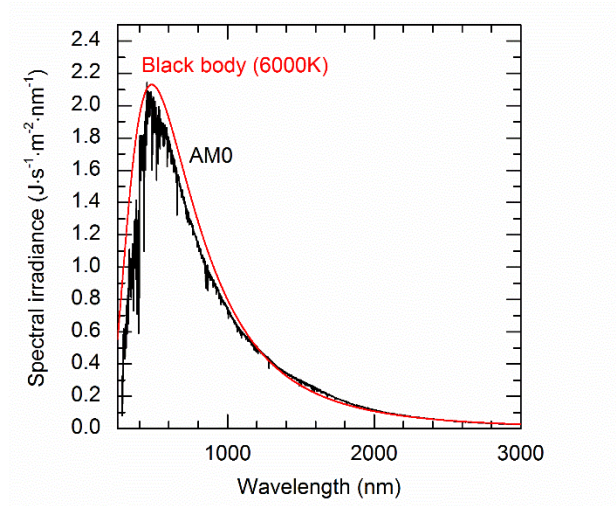

Fig. B-1 Calculated spectral irradiance of a black body source at 6000K (red) compared to the measured AM0 solar spectrum.

Spectral irradiance and photon flux:

The following two plots in Fig. B-2 show both the spectral irradiance and photon flux demonstrating the shift in peak wavelength/energy depending on whether the spectrum is calculated *per unit wavelength* or *per unit energy*.

Spectral irradiance
with respect to wavelength (nm)

Spectral irradiance
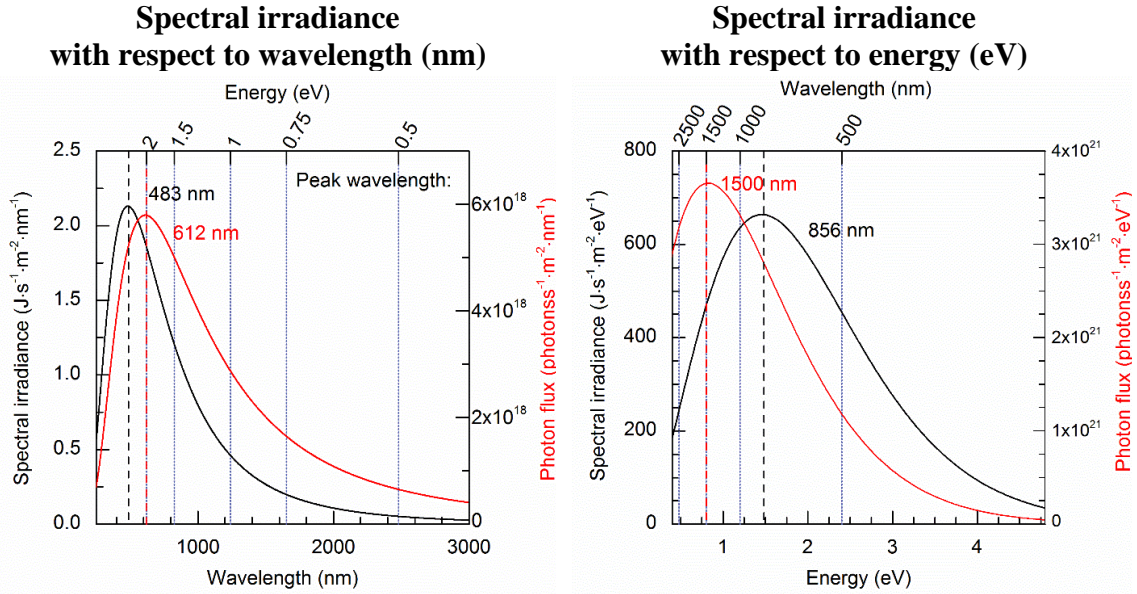**with respect to energy (eV)**

Fig. B-2 Calculated spectral irradiance and photon flux of a black body source at 6000K plotted per unit wavelength (left) and per unit energy (right).

Considering that we are interested in carrier collection for current generation, the photon density peak is much more relevant than the energy peak—one photon to one carrier. Because of the dramatic difference in peak position between the two spectra shown above, it may prove beneficial to plot measured solar cell data both ways.

Let's take for example, an ideal case in which we have a signal of unity representing a photo-response with a band edge cutoff of 850 nm; for the sake of simplifying the example, we will assume a lower bound of 350 nm. The first figure is presented as a signal *per unit wavelength* with evenly spaced intervals of dλ. Because of the inverse relationship between wavelength and energy, these same intervals are no longer evenly spaced when plotted per unit energy. However, the area for these two cases (total absorbed carrier density) must be the same, so the signal (y-axis) must deviate from unity. Combining the standard energy to wavelength conversion shown in equation (9) along with the relationship between the two

signals shown in equation (10), we get the conversion factor for the signal itself shown in equation (11).

$$E = \frac{hc}{\lambda} \tag{9}$$

$$f(\lambda)d\lambda = f\left(\frac{hc}{E}\right)|J|dE = F(E)dE \tag{10}$$

$$F(E) = f(\frac{hc}{E})\frac{hc}{E^2} \tag{11}$$

This is known as the Jacobian transformation. A comparison between these two plots is shown below in Fig. B-3 and demonstrates how the shape of the signal density (signal strength=signal density*Δx(λ,eV)) will change when converting to a signal density *per unit energy*. Despite the dramatic change in shape and intensity when moving to energy, the area of this curve is exactly the same as the first case.
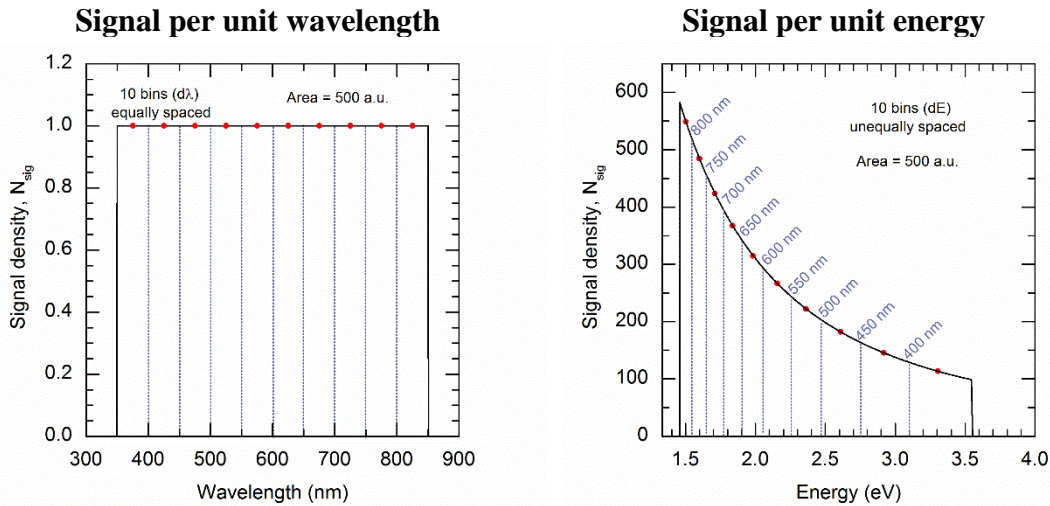

Fig. B-3 Unity signal with evenly spaced data points per unit wavelength (left) and the same unity signal when plotted per unit energy (right).

However, this is only the case with sufficiently small intervals or with perfectly continuous curves in which the area can be determined exactly. As we can see in Fig. B-3, while the interval is evenly spaced around the measured data point when plotted per unit

wavelength (±dλ/2), when plotted per unit energy, not only are these intervals of different sizes, they are no longer centered around the measured data points—data points shown in red. This means that even if the interval is sufficiently small enough to capture features in the left figure, when converting to units of energy, valuable information can be lost as the intervals are narrowed or spread out and the calculated area will differ slightly. When converting data back and forth between per unit wavelength, and per unit energy, the data points will always align and the intervals will change as a result. However, if two measurements of the same signal were to be taken—one with uniform intervals in wavelength and one with uniform intervals in energy—the data points will no longer align and we may find that one is more useful than the other in determining the shape of the curve in certain energy ranges.

Solar Cell EQE measurements:

Ultimately, this leads to the question, will this affect the devices EQE measurements and should we consider plotting them with respect to energy? While EQE measurements are typically carried out using a xenon-arc lamp with a series of filters and gratings within the monochromator, for the purposes of this example, we will assume the incident light is the AM1.5G solar spectrum. For the two cases considered, incident flux per unit wavelength and incident flux per unit energy, the densities are shown below. The data on the left is provided by NREL while the data on the right was calculated using the conversion factor in equation (11).
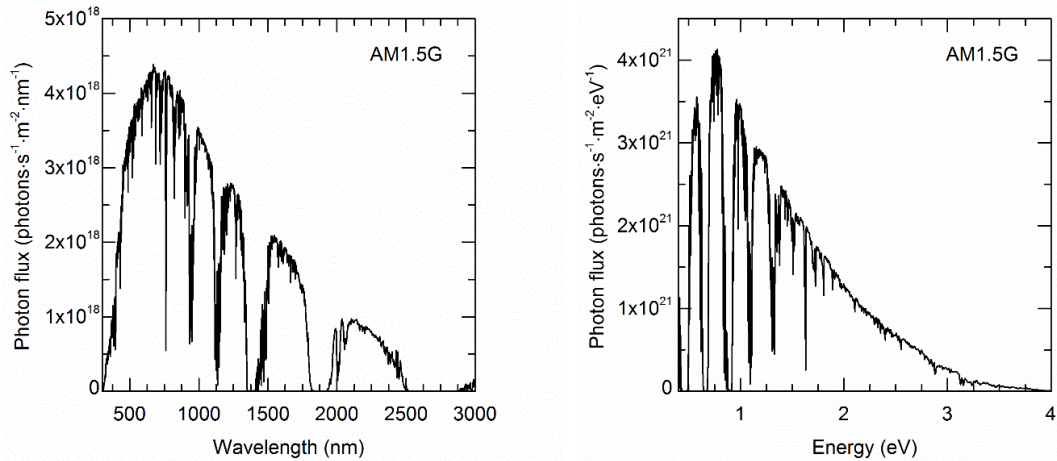
Fig. B-4 Photon density for the AM1.5G solar spectrum plotted per unit wavelength (left) and per unit energy (right).

Using the measured EQE shown below in Fig. B-5, we know that the collected carrier density will be the AM1.5G spectrum weighted against this EQE—shown in red in the right figure. The ratio between these two curves is thus the EQE.
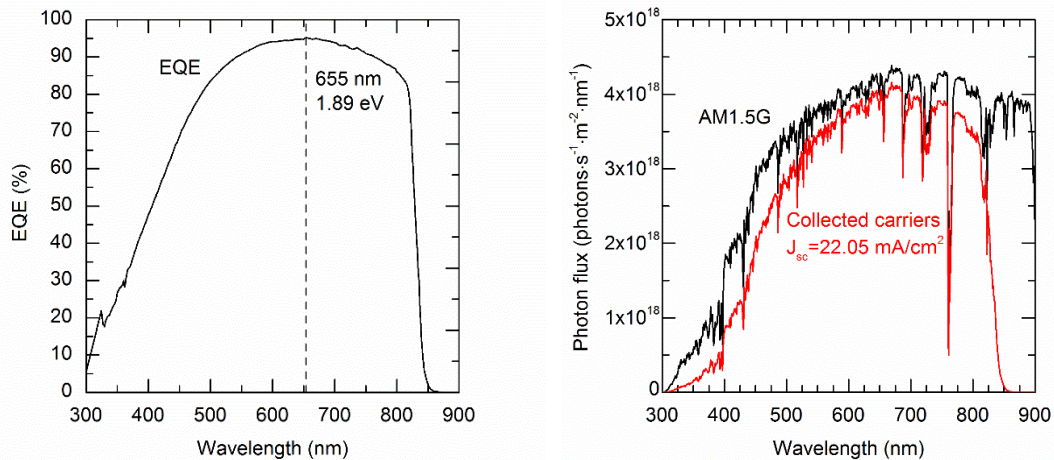

Fig. B-5 Measured EQE of CdTe/MgCdTe double-heterostructure solar cell (left) and the AM1.5G solar spectrum plotted alongside the carrier density collected by the solar cell (right).

This carrier density per unit wavelength can be converted using equation (11) above to give a collected carrier density per unit energy. Both curves are shown below. Integrating

both yields a short-circuit current density (J_{sc}) of 22.05 mA/cm^2, demonstrating that the overall current has remained unchanged regardless of the change in shape.
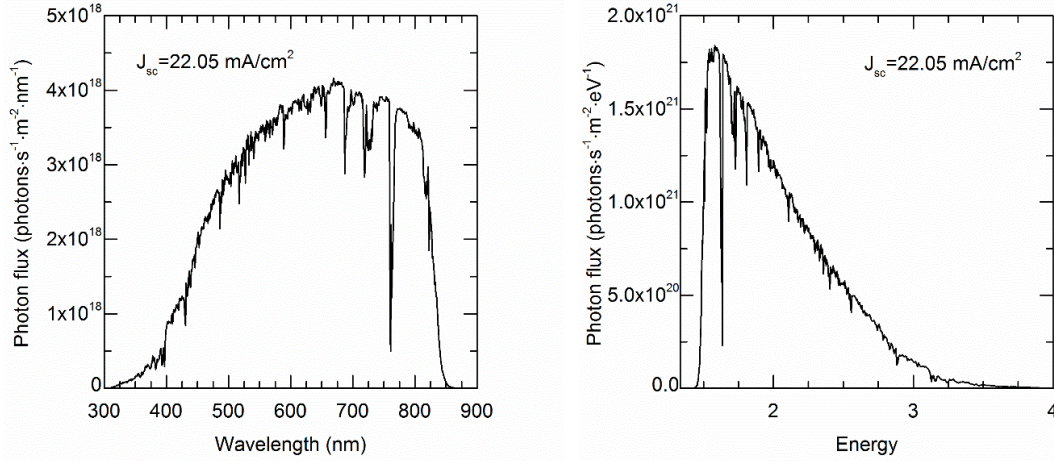

Fig. B-6 Collected carrier density from a CdTe/MgCdTe solar cell plotted per unit wavelength (left) and per unit energy (right).

Working backwards once more, and dividing the collected carrier density per unit energy by the AM1.5G solar spectrum per unit energy yields the ratio of collected carriers to incident carriers, the EQE.
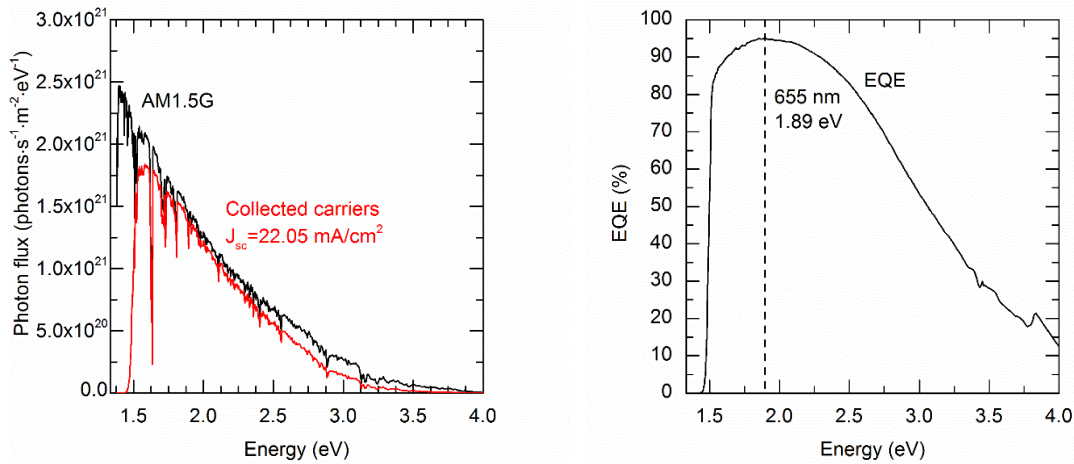

Fig. B-7 AM1.5G photon density and collected carrier density plotted per unit energy (left) and the EQE calculated as the ratio of these two curves (right).

In both cases, we have an incident spectrum either per unit wavelength or per unit energy, as well as a collected carrier density in either per unit wavelength or per unit energy. Because the current density in these two cases must be equivalent and the solar spectrum must also be equivalent, the ratio will also be equivalent at all points. This means that the EQE curve's feature positions will be independent of the underlying measurements dependence on either wavelength or energy. Even though the visual appearance will change as the x-axis is inverted and stretched when moving to energy, the peak position will not change; 655 nm in this case. This same conclusion can be reached when examining equation (12).

$$EQE = \frac{N_{col}(\lambda)}{N_{sun}(\lambda)} = \frac{N_{col}\left(\frac{hc}{\lambda}\right) \cdot \left(\frac{hc}{E^2}\right)}{N_{sun}\left(\frac{hc}{\lambda}\right) \cdot \left(\frac{hc}{E^2}\right)} = \frac{N_{col}(E)}{N_{sun}(E)} \tag{12}$$

where N_{col} is the carrier density collected by the solar cell under investigation and N_{sun} is the photon density incident on the surface. The right-hand side of the equation converts wavelength to energy and uses the Jacobian transformation on both densities. Because the EQE is a ratio of these two densities, regardless of whether we plot it as a function of wavelength or energy, the Jacobian transformation will cancel and we are left with the same EQE; although the appearance will of course differ as the scale is changed.

However, this all hinges on the ability to maintain relatively narrow data intervals when transitioning between plots per unit wavelength and per unit energy. Because of the uneven distribution of data points after the conversion, energy/wavelength dependent error is introduced as the intervals are elongated in the energy space. For broad flat spectra like are commonly seen with EQE measurements, this error is not necessarily detrimental; especially considering that the range is typically confined to the visible portion of the

spectrum. For peaks with a narrow linewidth this effect may become an issue, but for these

CdTe devices it is not considered to be a problem.